Nonlinear transient burning of solid rocket propellants

Louwers, J.

Award date:
1995

Nonlinear Transient Burning of Solid Rocket Propellants.

Jeroen Louwers[1]

August 1995

[1]Prins Maurits Laboratory TNO, P.O. Box 45, 2280 AA Rijswijk, The Netherlands

Summary.

In this thesis the nonstable combustion of solid rocket propellants is discussed within the QSHOD - flame modeling - approach. All calculations are performed for a reference AP-HTPB composite propellant.

A survey of the model and its assumptions are given. For small disturbance amplitudes linear perturbation techniques can be applied to calculate the response of the propellant, yielding the linear frequency response functions. For larger disturbances, chemical reactions, and other strong nonlinearities, these linearized calculations are not applicable anymore. For this, the systems of equations is solved numerically.

The common inert condensed phase with constant thermal properties is replaced by a chemical reacting condensed phase with temperature dependent thermal properties and phase changes of AP. This condensed phase can still be seen as a simplification, but is in better agreement with the reality. It is shown that the introduction of this more realistic condensed phase has a large effect on the response function of a solid rocket propellant.

The introduction of subsurface reactions and phase transitions of AP results in a propellant which has a higher intrinsic combustion stability. It is also shown that the temperature dependent properties have a large effect on the intrinsic combustion instability.

For high values of the surface heat release, self-sustained oscillatory combustion occurs. During self-sustained combustion the propellant burns with characteristic spikes, without an external driving force.

An existing analytical nonlinear combustion stability analysis is discussed, which is compared to a linear numerical stability approach. Both methods are applied to find the value of the heat release where self-sustained oscillations emerge.

Finally the stability for an HNF/GAP propellant combination is discussed. Due to the high heat release in the solid phase of the propellants, compared with composites, these propellants exhibit a large intrinsic combustion instability.

Contents

1 Solid rocket propulsion. **1**
1.1 Introduction. 1
1.2 Burning of solid propellants. 2

2 Transient burning of solid propellants. **5**
2.1 Introduction. 5
2.1.1 History. 5
2.1.2 Classification of instabilities. 5
2.2 Response functions. 6
2.3 Radiation-driven transient burning. 8
2.3.1 Background. 8
2.3.2 Experimental technique. 8
2.3.3 Optical characteristics of solid propellants. 10

3 Flame modeling. **11**
3.1 Introduction. 11
3.2 The condensed phase. 13
3.3 The burning surface. 14
3.4 The gas phase. 15
3.4.1 KTSS Flame Model. 18
3.4.2 The $\alpha\beta\gamma$-flame model. 19

4 Linear frequency response functions. **23**
4.1 Condensed phase. 23
4.2 Surface connection relations. 25
4.3 Gas phase. 26
4.4 Pressure-driven frequency response function. 26
4.5 Radiation-driven frequency response function. 27
4.6 Transfer function. 28
4.7 Summary of the assumptions. 29

5 Model for the transient burning of AP-composites. 31
5.1 Model for a reacting condensed phase. 31
5.2 Summary of the equations. 33

6 Numerical calculations of non-steady burning. 34
6.1 Transformation of the problem. 34
6.2 Finite difference approximation. 36
6.3 Implementation in software. 38
6.4 Steady-state burning. 39
6.5 Time-dependent burning. 45
6.5.1 Introduction. 45
6.5.2 Combustion transients. 46
6.5.3 Pressure driven frequency response functions. 52
6.5.4 Radiation driven frequency response functions. 58
6.5.5 Condensed phase reactions. 61
6.5.6 Response functions of AP-composites. 66
6.5.7 Effect of gaseous heat release distribution. 68

7 Intrinsic combustion instability. 70
7.1 Nonlinear combustion instability. 70
7.1.1 Static restoring function. 72
7.1.2 Bifurcation diagrams. 73
7.2 Stability of an equilibrium of a linearized system 78

8 Conclusions and suggestions for future work. 82

A Derivations. 91
A.1 Derivation of the steady state thermal profile. 91
A.2 Derivation of the transient thermal profile. 92
A.3 Derivation of the linearized pyrolysis laws. 94
A.4 Derivation of the static restoring function. 95

B Numerical methods. 99
B.1 Finite-differences approximation of the condensed phase energy equation. . 99
B.2 Thomas algorithm. 99

C The Zeldovich-Novozhilov approach. 101

D Thermophysical properties of AP-composites. 103
D.1 Thermophysical properties of AP. 103
D.2 Thermophysical properties of HTPB. 104
D.3 Thermophysical properties of an AP/HTPB propellant. 104

E HNF-GAP propellants. **108**
E.1 Properties of HNF-GAP propellants. 108
E.1.1 Properties of HNF. 108
E.1.2 Properties of GAP. 108
E.1.3 Properties of HNF-GAP propellants. 109
E.2 Burning of HNF-GAP propellants. 111
E.2.1 Steady state burning. 111
E.2.2 Response functions. 111

F TW95 Workshop. **114**

List of Figures

1.1 Schematic of a homogenous double-base propellant, and a heterogenous composite propellant. 2
1.2 The zones in the combustion of a double-base propellant. 3
1.3 BDP-Multiple flame model of composite propellant combustion. 4

2.1 Linear and nonlinear combustion instabilities. 6
2.2 Typical setup for radiation-driven transient burning experiments. 9

3.1 Schematic view of the overall physical problem. 11
3.2 Schematic of heat release distribution by the KTSS-model. 18
3.3 Schematic of heat release distribution by a Dirac delta function. 19
3.4 Schematic of heat release distribution by the $\alpha\beta\gamma$-model. 20

4.1 Surface of solid propellant during burning transients. The condensed phase moves with velocity $\bar{r}_b$ to the right. Due to the transients the surface can be seen to fluctuate between $x = s^-$ and $x = s^+$. 24
4.2 Response function for $A = 14$, $B = 0.8$, $n = 0.5$, $n_s = 0$ and $n_s = 1$. 28

5.1 Schematic of the temperature distribution in an AP-propellant. 32

6.1 Illustration of the transformation. 35
6.2 Schematic of the computational molecule. 36
6.3 Flow chart of the program. 39
6.4 Flow chart of the calculation of the thermal profile in the condensed phase. 40
6.5 Comparison of the steady-state equation $r_b = ap^n$ and the Arrhenius pyrolysis law. 41
6.6 Steady-state thermal profiles in the condensed phase. Profile 1 is obtained by calculations with variable thermal properties, and profile 2 is the analytical solution of the energy equation. 42
6.7 Removal of the discontinuties of the thermal conductivity. 43
6.8 Effect of the latent heat of crystal transition and melting of AP on the steady-state thermal profiles in the condensed phase. 43
6.9 Comparison of calculated and measured thermal profile at 1.5 MPa. In the calculation the latent heat of crystallographic transition, and melting have been set to zero. 44

6.10 Combustion transient during a sinusoidal pressure disturbance. 45
6.11 Temperature profiles in the condensed phase during transient burning. . . . 46
6.12 Combustion transient during a pressurization from 1 to 2 MPa. It can be seen that the effect of the surface and condensed phase heat release, Q_s and Q_c is identical. 47
6.13 Effect of increase of external radiant flux on the surface temperature, for two extreme values of condensed phase absorption. 48
6.14 Response of the propellant on a sinusoidal pressure perturbation, with an amplitude of 10% and 50% of its steady state value of 1.0 MPa. 49
6.15 Effect of the disturbance amplitude on the fft-spectrum. 50
6.16 Pulsating perturbation and the response of the propellant. 50
6.17 FFT spectrum of the pulsating perturbation and the response of the propellant. 51
6.18 Fluctuating surface temperature due to a sinusoidal pressure disturbance. After a few initial cycles the surface temperature responds periodically. . . 52
6.19 Nonlinear pressure driven response function versus linear calculated response function (constant thermal properties). 53
6.20 Effect of the value of the steady-state pressure on the pressure coupled response function, for temperature dependent thermophysical properties. . . 55
6.21 Effect of the value of the steady-state pressure on the pressure coupled response function, for temperature dependent thermophysical properties. . . 56
6.22 Effect of the value of the steady-state pressure on the pressure coupled response function, for constant thermophysical properties. 56
6.23 Effect of the value of the steady-state pressure on the pressure coupled response function, for constant thermophysical properties. 57
6.24 Effect of the thermal properties on the pressure coupled response function. 57
6.25 Effect of volumetric absorption coefficient $\bar{\bar{a}}_\lambda$ on the radiation driven response function for the reference propellant, for a heat flux of 50 cal/cm^{2}s. Crystal transitions and condensed phase reactions have been neglected in these calculations. 59
6.26 Effect of volumetric absorption coefficient $\bar{\bar{a}}_\lambda$ on the radiation driven response function for the reference propellant, for a heat flux of 100 cal/cm^{2}s. Crystal transitions and condensed phase reactions have been neglected in these calculations. 60
6.27 Experimentally determined steady-state burning rate as function of the applied external heat flux for three different propellants [24]. 60
6.28 Heat release rates for different values of the parameter n. 62
6.29 Steady state temperature profile for several values of the parameter n. . . . 63
6.30 Transient burning due to a sinusoidal pressure disturbance for several values of the parameter n ($\bar{P}$ = 1.0 MPa, $\Delta P/\bar{P}$ = 10 %). 64
6.31 Effect of heat release distribution on the pressure coupled response function. By decreasing the reaction layer (increase of parameter n) the intrinsic stability increases, and the resonance peak shifts towards higher frequencies. . 64

6.32 Effect of heat release distribution on the pressure coupled response function. Surface reactions (infinitesimally thin reaction layer) have the largest response. By increasing the reaction layer (decrease of activation energy) the intrinsic stability increases. 65
6.33 Effect of latent heats on the normalized pressure driven response function for the reference propellant. 66
6.34 Effect of condensed phase heat release and phase transitions in the solid phase on the normalized pressure coupled response function. 67
6.35 Effect of parameter γ on the pressure coupled response function ($\alpha = 0, \beta = 1$). 68
6.36 Effect of parameter α on the pressure coupled response function ($\gamma = 1$, and $\beta = 0.5$, except for $\alpha = 0$, then by definition $\beta = 1$). 69

7.1 Condensed phase with two temperature profiles. The steady state profile $\bar{\Theta}(X)$, and the perturbed profile $\Theta(X, \tau)$. The perturbation is limited to the disturbance layer thickness $\xi(\tau)$. 71
7.2 Typical plot of a static restoring function with three roots. 72
7.3 Typical plot of a static restoring function with five roots. 73
7.4 Typical plot of a static restoring function when roots B and D have exchanged stability. The only possible stable configuration is the nonreacting situation, represented by root C. 74
7.5 Envelope of the fluctuating surface temperature for a slowly varying surface heat release, Q_s. 75
7.6 Characteristic spikes during self-sustained transient burning. 76
7.7 Bifurcation diagram at 1.0 MPa pressure. Shown are the roots of the static restoring function, (A, B, C, and D), and the envelope of a numerical calculation, by slowly varying Q_s. 76
7.8 Extinction during a pressurization from 0.9 to 1.0 MPa. 77
7.9 Hysteresis in the envelope of the fluctuating surface temperature for an increase in surface heat release, followed by a decrease in surface heat release. 77
7.10 Plot of the normalized modulus of $\vec{x}_{dis}$ as function of the time. For $Q_s \leq 130$ the modulus returns to it's value at $\tau = 0$. For larger values the equilibrium is unstable, diverging from the steady situation because of the perturbation at $\tau = 0.1$. 81

D.1 Specific heat of an AP/HTPB:86/14 propellant as function of the temperature. 105
D.2 Thermal conductivity of an AP/HTPB:86/14 propellant as function of the temperature. 107

E.1 Estimated surface temperature as function of the pressure for a HNF-GAP propellant. 111
E.2 Comparison of the temperature profile in the condensed phase of a typical AP-propellant (1) and a HNF-GAP propellant (2). Both calculations with constant thermal properities. 112

E.3 Comparison of the pressure coupled response function of a HNF/GAP-propellant with that of the AP reference propellant. 113
E.4 Pressure coupled response function of a HNF/GAP-propellant for several values of the surface heat release. 113

Nomenclature.

Roman symbols.

A	Nondimensional constant of two parameter form	-
A_c	Nondimensional prefactor of Arrhenius pyrolysis law	-
$\bar{\bar{a}}_\lambda$	Volumetric absorption coefficient	m^{-1}
B	Nondimensional constant of two parameter form	-
C	Nondimensional specific heat	-
c	Specific heat	J/kgK
c_1	Nondimensional constant	-
c_2	Nondimensional constant	-
c_3	Nondimensional constant	-
D	Mass diffusivity	m^2/s
d	Thickness	cm
E	Nondimensional activation energy	-
$\tilde{E}$	Dimensional activation energy	J/mole
F	Function as defined in text	-
F_0	Nondimensional external radiant flux	-
f	Function as defined in text, weight fraction	-
g	Function as defined in text	-
h	Enthalpy	J/kg
$H_{()}$	Nondimensional heat release	-
I_0	External radiant flux intensity	W/m^2
K	Nondimensional thermal conductivity	-
k	Dimensional thermal conductivity	W/mK
l_r	Ratio of thermal to radiant layer thickness	-
M	Molecular weight	g/mole
$\dot{m}$	Mass burning rate	kg/m^2s
N_t	Fraction of radiant flux absorbed in condensed phase	-
n	Pressure exponent, parameter as defined in text	-,-
n_q	Exponent of burning rate vs radiant heat relation	-
n_s	Pressure exponent in pyrolysis laws	-
P	Nondimensional pressure	-
p	Pressure	Pa
Q	Heat release	J/kg

q	Nondimensional heat flux	-
q_r	Nondimensional radiant flux intensity	-
R	Nondimensional burning rate	-
$\Re$	Universal gas constant	J/molK
R_p	Pressure driven response function	-
R_q	Radiation driven response function	-
r_b	Burning rate	m/s
$\bar{\bar{r}}_\lambda$	Reflectivity of the propellant surface	-
T	Temperature	K
t	Time	s
t^*	Characteristic Time	s
U	Nond. average gas velocity	-
u	Velocity, nond. temperature disturbance profile, nond. temperature disturbance profile	m/s,-, -
W	Normalization prefactor in $\alpha\beta\gamma$-model	-
w_s	Pressure exponent in KTSS pyrolysis law	-
X	Nondimensional space coordinate	-
x	Dimensional space coordinate	m
$\vec{x}$	Nondimensional state vector	-

Greek symbols.

α_c	Thermal diffusivity of the condensed phase	m^2/s
α	Parameter of the $\alpha\beta\gamma$-model	-
β	Parameter of the $\alpha\beta\gamma$-model, transformation variable	-
γ	Parameter of the $\alpha\beta\gamma$-model	-
$\Delta\ldots$	Increase/decrease of ...	-
δ_a	Nondimensional optical layer thickness	-
$\delta_{i,j}$	Kronecker-delta (= 1 if $i = j$, otherwise = 0	-
ϵ	Nondimensional chemical reaction rate	-
$\bar{\bar{\epsilon}}_\lambda$	Optical emissivity	-
λ	Wavelength, characteristic root, eigenvalue	m,-,-
$\vec{\eta}$	Eigenvector of linearized system	-
ϕ	Phase shift	rad
Φ	Temperature gradient, function as defined in text	K/m,-
ρ	Density	kg/m^3
σ	Stefan-Boltzmann constant	W/m^2K
Θ	Nondimensional temperature	-
τ	Nondimensional time	-
$< \tau' >$	Nondimensional characteristic time parameter	-
Υ	Nondimensional temperature	-

ω	Dimensional circular frequency	rad/s
$\bar{\omega}$	Nond. uniform gaseous heat release of KTSS flame	-
Ω	Nondimensional circular frequency	-
ξ	Nondim. thermal layer disturbance thickness	-
ζ	Function as defined in text	-

Subscripts and superscripts.

a	Cold boundary
c	Condensed phase
dec	Decomposition
dis	Disturbed situation
eq	Equilibrium
ext	External
f	Flame
g	Gaseous phase
i	Initial, imaginary part
j	Grid point index
k	Grid point index
m	Melting of AP
p	With respect to the pressure driven response function
q	With respect to the radiation driven response function
r	Real part
ref	At reference conditions
s	Burning surface
tra	Crystallographic transition
T_f	Differentiated with respect to T_f
T_s	Differentiated with respect of T_s
w	Weighted average
$\sum$	Total
$+$	On the positive side of
$-$	On the negative side of
$(\ldots)'$	Fluctuating part of ..., transformed variable
$\bar{\ldots}$	Steady-state value of ...

Definitions of nondimensional quantities.

$C_{()}$	=	$c_{()}/c_{(),ref}$	Nondimensional specific heat
$E_{()}$	=	$\tilde{E}_{()}/(\Re T_{s,ref})$	Nondimensional activation energy
F_0	=	I_0/I_{ref}	Nondimensional thermal flux
$H_{()}$	=	$Q_{()}/Q_{ref}$	Nondimensional heat release
l_r	=	$\bar{\bar{a}}_\lambda \alpha_c/\bar{r}_b$	Ratio of thermal to radiant layer thickness
Ω	=	$\omega \alpha_c/\bar{r}_b^2$	Nondimensional circular frequency
P	=	p/p_{ref}	Nondimensional pressure
q_r	=	I_0/I_{ref}	Nondimensional thermal flux
R	=	$r_b/r_{b,ref}$	Nondimensional burning rate
X	=	x/x_{ref}	Nondimensional space coordinate
δ_a	=	$(1/\bar{\bar{a}}_\lambda)/x_{ref}$	Boundary layer thickness
τ	=	t/t_{ref}	Nondimensional time
Θ	=	$(T - T_{ref})/(T_{s,ref} - T_{ref})$	Nondimensional temperature
Υ	=	$T/T_{s,ref}$	Nondimensional temperature

Reference properties.

I_{ref}	=	$\rho_c\, c_{c,ref}\, r_{b,ref}\, (T_{s,ref} - T_{ref})$	Energy flux
Q_{ref}	=	$c_{c,ref}\, (T_{s,ref} - T_{ref})$	Heat
t_{ref}	=	$\alpha_c/r_{b,ref}^2$	Time
x_{ref}	=	$\alpha_c/r_{b,ref}$	Length

Acronyms.

AP	Ammonium Perchlorate
BDP	Beckstead, Derr, and Price
CMDB	Composite Modified Double-Base
DB	Double Base
DFT	Discrete Fourier Transform
FFT	Fast Fourier Transform
FM	Flame Modeling
GAP	Glycidil Azide Polymer
HNF	Hydrazinium Nitroformate
HTPB	Hydroxyl Terminated PolyButadiene
KTSS	Krier, T'ien, Sirignano and Summerfield
PBAA	PolyButadiene Acrylic Acid
QSHOD	Quasi-Steady Homogeneous One-Dimensional
TF	Transfer Function
ZN	Zeldovich-Novozhilov

Preface.

This thesis is written to obtain a masters degree in Engineering Physics at the Eindhoven University of Technology.

A short introduction to solid rocket motor technology is included in chapter one. Chapter two contains a background of transient burning, experimental techniques and the definition of response functions. Chapter three is a general section that covers flame modeling. In this chapter the equations governing in the condensed phase, burning surface, and gas phase are discussed. Chapter four deals with the common linearized approach, based on the theory of chapter three. In chapter five an extended model for transient burning is presented, which is solved numerically in chapter six. This chapter also discusses several aspects of nonlinearity of the equations, and the results are compared with the linearized analysis of chapter four. In chapter seven combustion stability, by linear, as well as nonlinear, approaches is reviewed, which is then compared with some of the results of chapter seven. The appendices A and B contain several derivations. To be complete, the Zeldovich-Novozhilov approach is discussed briefly in appendix C. In appendix D the properties of a typical AP-composite are presented. This propellant serves as a reference for all the calculations in this thesis. Appendix E deals with the intrinsic stability of a next generation propellant, HNF/GAP, which is currently under development at TNO/PML. Finally, appendix F contains a poster and handout as presented at the TW95 meeting.

Acknowledgements.

I would like to express my thanks to the following: My mentors Guy Gadiot (TNO/PML) and Willem van de Water (TUE), for their advice, encouragement and the many useful suggestions for improving the preliminary version of this thesis. Paul Korting for making it possible to carry out my thesis at TNO/PML. And all members of the Rocket Propulsion Group of TNO/PML for their continuous interest, and the pleasant collaboration.

Chapter 1

Solid rocket propulsion.

1.1 Introduction.

In essence rocket propulsion can be divided in chemical propulsion, nuclear propulsion and electric propulsion [56]. Of these types only chemical propulsion is extensively used. Chemical propulsion can be divided further in liquid propellant rocket engines and solid propellant rocket engines, and combinations thereof.

Although the performance of solid propellants is not as good as their liquid counterparts, they are in most cases preferred, because of their reliability, simplicity and storability. An illustrative example of modern solid rocket engines are the boosters of the Space Shuttle vehicle and the Ariane 5 launcher.

Solid rocket motors contain energetic material which reacts to form species with a low molecular weight at high temperatures. These gaseous products are accelerated through a Laval nozzle to produce the desired thrust. The current solid propellant can be divided into two classes, double-base (DB) propellants and composite propellants.

Double-base propellants were the first production propellants. Essentially they consist of a nitrocellulose, in which nitroglycerin is dissolved. This yields a *homogeneous* propellant. Both ingredients are explosives and function as a combined fuel and oxidizer in one molecule.

Composite propellants form a *heterogeneous* propellant with the oxidizer crystals held together in a matrix of synthetic rubber binder, usually a polybutadiene. The oxidizer decomposes during heating, releasing oxygen. This oxygen burns the rubber. Nowadays ammonium perchlorate (AP) is the most common used oxidizer. Often a metallic fuel such as aluminum is included to enhance performance. Figure 1.1 schematically shows the difference between DB and composite propellants. Also combinations of DB and composite propellants exist, and these have been called composite modified double-base (CMDB) propellants.

It is obvious that this classification is far from complete, see reference [56] for more information.

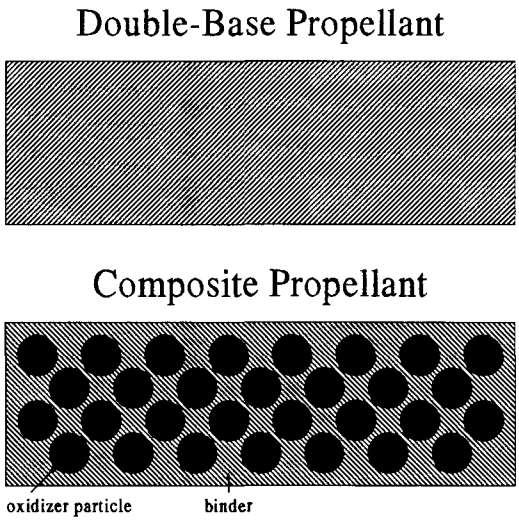

Figure 1.1: Schematic of a homogenous double-base propellant, and a heterogenous composite propellant.

1.2 Burning of solid propellants.

During burning of homogeneous propellants, the components pass unaffected through a preheated zone a few of tens of microns thick (see figure 1.2) and reach a very thin (few microns thick) degradation zone, known as the foam zone. Here there is a rise in temperature, which is sufficient for degradation to take place. At pressures below 10 MPa, a distinction can be made between the primary fizz zone and the secondary luminous flame, which are separated by the dark zone. In this pressure range the secondary flame is too distant to have any effect on the surface, and does not even induce a temperature gradient in the primary zone. As a consequence, the burning rate is influenced only by the fizz zone.

Composite propellants are of heterogeneous structure. They consist of oxidizer crystals embedded in a matrix of a polymerized binder. The heterogeneous-structure burning processes are more complicated than that of homogeneous propellants. Most composite solid propellant burning models are based on the Beckstead-Derr-Price model [2]. This model assumes multiple flames surrounding the ammonium perchlorate (AP) particles, see figure 1.3. Flame thicknesses found in experiments vary from $10\,\mu m$ up to $1000\,\mu m$ depending upon pressure and AP particle size.

The burning rate of solid propellants is dependent on several parameters, e.g. the pressure, the particle size distribution, the initial temperature, the presence of catalysts, and the velocity of the gas flow parallel to the burning surface. The pressure dependence for both DB and composite propellants can be described by an empirical equation

$$r_b = a\,p^n\ , \tag{1.1}$$

where r_b is the burning rate (m/s) and p is the pressure (Pa). The parameter n is known as the burning rate pressure exponent or combustion index. This relation is only valid

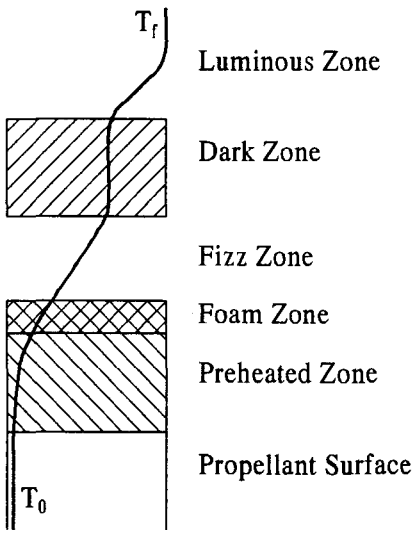

Figure 1.2: The zones in the combustion of a double-base propellant.

during steady-state combustion, and not during transient burning[1], when the burning rate can be a magnitude larger as compared to steady burning.

The solid propellant *itself* is called the grain. By modifying the geometrical shape of the grain, the thrust-time curve can be programmed.

[1]In this thesis the term steady-state is used for processes which do not have a time dependency. Processes which are time dependent are called transient. So the term transient should not be confused with its meaning as starting transition.

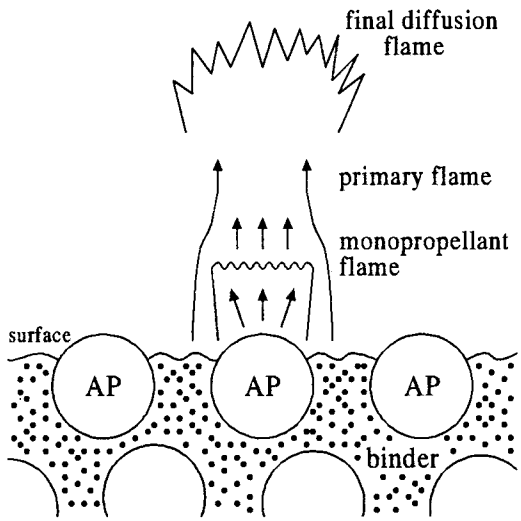

Figure 1.3: BDP-Multiple flame model of composite propellant combustion.

Chapter 2

Transient burning of solid propellants.

2.1 Introduction.

2.1.1 History.

Early in the Second World War irregular thrust-time curves were occasionally observed for solid propellant rockets. In extreme instances the chamber pressure would exceed the structural strength of the motor casing, causing the rocket motor to explode. Irregular chamber pressure traces were often associated with oscillations in the flow. They could not be explained in terms of variations in burning area or erosive burning[1]. The phenomenon, known as irregular burning, was therefore assumed to originate either in the combustion process itself or in the interaction of the combustion process, with acoustical waves in the combustion chamber. This general view has now been well established even though the detailed mechanisms involved are not understood entirely.

2.1.2 Classification of instabilities.

The general phenomenon of irregular burning may be divided into two main categories, acoustic instability and nonacoustic instability.

In early observations the irregular burning was often accompanied by pressure fluctuations of acoustic frequencies. This led to the assumption that irregular burning was caused by amplification of the acoustic waves in the combustion chamber by the combustion processes occurring therein. Irregular burning produced by mechanisms involving sound vibrations in an essential way, is termed *acoustic instability.*

Unstable combustion can also occur without interaction between the combustion processes and sound waves in the chamber. For example, *chuffing* combustion oscillation frequencies below any acoustic frequencies of the chamber have been observed for certain

[1] Enlarged burning rate due to extensive crossflow over the burning surface

propellant formulations. Any occurrence of irregular burning that does not involve interaction between the combustion process and a sound field in an essential way, can be termed nonacoustic instability or *intrinsic instability.*

In rocket motors both instabilities can amplify each other. Acoustic pressure oscillations cause the pressure to be a time dependent quantity. It is described in this thesis that this fluctuating pressure causes a time-dependent burning of the propellant. This produces acoustic disturbances by the unsteady mass, momentum and energy ejection in the combustion chamber. When this process occurs at proper spatial and temporal phases, a feedback loop may be established and substantial pressure oscillations can be sustained.

A further division can be made into linear and nonlinear instabilities. Linear instabilities are those which can be described in terms of small-amplitude perturbations about steady, normal burning. A rocket motor is linearly-unstable when a small disturbance causes the combustion pressure to grow exponentially. Nonlinear instabilities are those involving finite-amplitude perturbations. A nonlinear unstable rocket motor is stable for small pressure fluctuations, but unstable when these fluctuations exceed a critical value. Figure 2.1 summarizes these two possibilities. It has been observed that experimental motors which are linearly stable may be nonlinearly unstable [7].

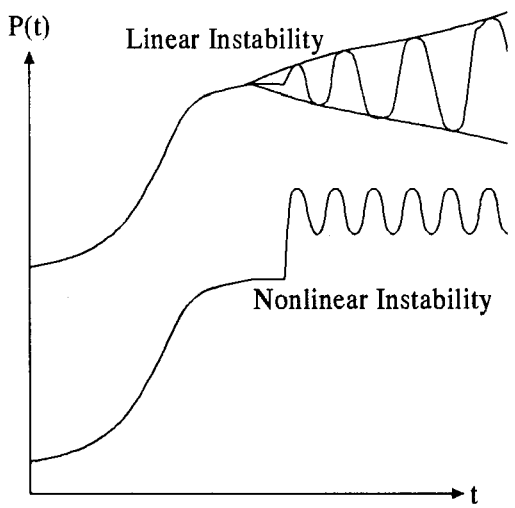

Figure 2.1: Linear and nonlinear combustion instabilities.

2.2 Response functions.

It was discussed in the previous paragraph that pressure oscillations affect the burning rate of a solid propellant. When the possible instability of a rocket motor is verified, it is necessary to know the response of the propellant on an acoustic pressure disturbance in the motor cavity. This response can be expressed by the pressure coupled response function,

defined as,

$$R_p = \frac{m'/\bar{m}}{p'/\bar{p}} = \frac{r_b'/\bar{r}_b}{p'/\bar{p}}, \tag{2.1}$$

where m' the fluctuating value of the mass burning rate, $\bar{m}$ the steady-state value mass burning rate, p' the fluctuating value of the pressure, and $\bar{p}$ the steady-state value of the pressure. The second equality holds because the burning rate, r_b, can be calculated as $r_b = m/\rho_c$, where ρ_c the density of the condensed phase.

For measurements it is often desirable to disturb the steady-state burning with fluctuating radiation (see section 2.3). Analogous to the pressure response function, the response function with respect to radiation fluctuation is defined as

$$R_q = \frac{m'/\bar{m}}{I_0'/\bar{I}_0} = \frac{r_b'/\bar{r}_b}{I_0'/\bar{I}_0}, \tag{2.2}$$

where I_0 the external radiant flux intensity. Response functions are complex functions because in general the mass-rate oscillations are not in phase with the pressure oscillations.

In a linearized analysis of oscillations, the oscillations of pressure in a specific mode have the form

$$\frac{p'}{\bar{p}} = P\, e^{i\omega t} \tag{2.3}$$

where P the complex amplitude of oscillation at some arbitrary time $t = 0$. Assume the mass burning rate oscillates in response to the pressure oscillations,

$$\frac{m'}{\bar{m}} = M\, e^{i\omega t} \tag{2.4}$$

where M the complex amplitude at $t = 0$. The relation of mass-rate oscillation to pressure oscillations is characterized by a ratio of amplitudes

$$R_p(\omega) = \frac{m'/\bar{m}}{p'/\bar{p}} = \frac{M}{P}\,. \tag{2.5}$$

So in general R_p is a complex function because of the phase difference between mass rate and pressure. A positive real part of the frequency response function implies an amplification of the pressure wave. The frequency response function can be seen as an index which measures the tendency of the combustion processes to drive waves and, ultimately, to trigger instability.

Mathematically, the response functions have to respect the corresponding static limit when $\omega \to 0$:

$$\lim_{\omega\to 0} R_p(\omega) = \lim_{\omega\to 0} \frac{m'/\bar{m}}{p'/\bar{p}} = n, \tag{2.6}$$

$$\lim_{\omega\to 0} R_q(\omega) = \lim_{\omega\to 0} \frac{m'/\bar{m}}{I_0'/\bar{I}_0} = n_q, \tag{2.7}$$

being n and n_q exponents defined respectively by the experimental steady-state burning rate laws.

2.3 Radiation-driven transient burning.

There is a growing recognition of the advantages of studying the combustion of solid propellants using unsteady external radiant energy sources such as lasers. This technique is called *radiation-driven transient burning.* A reason that this particular approach has recently received renewed interest is that it is easier to control a radiant flux and to simultaneously measure the instantaneous burning rate than to perform a similar experiment with an unsteady pressure field. This method has some further advantages; it is contactless, the energy can be introduced into various spatial zones in the condensed phase due to the wavelength dependence of propellant transparency, and the radiative heating can be carried out at different pressures and different compositions of a gaseous medium.

2.3.1 Background.

One of the first studies on radiation-driven burning was that of Milfeith et al. [41], who used a force transducer to measure dynamic burning rate of non-metalized AP-composite propellants under the action of an oscillating radiant flux from a xenon mercury lamp. Recoil force was converted to instantaneous mass flux via a momentum balance. Soon hereafter Zarko and co-workers in Russia began an extensive program, using similar experimental methods, which has continued to the present [58] [59]. Recently, Strand et al. [54] and DeLuca [18] used a CO_2 laser as perturbing source.

2.3.2 Experimental technique.

A setup for measurements of characteristics of radiation-driven transient burning of solid propellant includes a radiation source which can be modulated, a radiation power meter, a transducer for measuring the recoil force and a recording unit. Figure 2.2 shows a typical setup for radiation-driven transient burning experiments.

For the irradiation of the sample, several sources can be used. In the first experiments xenon lamps were used as radiation source in the majority of the experiments. The radiation spectrum of the lamp is similar to the solar one, extending from ultraviolet to the far infrared. Variation of the radiation intensity is realized by a slotted disk, rotating in front of the lamp. Nowadays CO_2 (10.6μm) or Nd/YAG (1.06μm) lasers serve as radiation sources.

Because of the attenuation of the laser beam by the plume, and the propellant reflectivity [30], it is necessary to measure the radiant flux reaching the surface. Often a small fiberoptic is placed through the propellant sample [4] [31]. Laser radiation on the surface passes through the fiber producing a signal which can be detected by a photodiode.

A method for the determination of the transient mass flux is to measure the change in force generated normal to the surface when the burning rate of a propellant is modified by an external thermal energy source. By means of a momentum balance, the total recoil

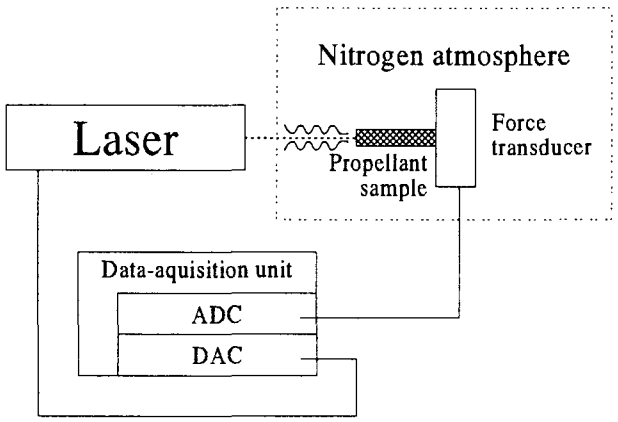

Figure 2.2: Typical setup for radiation-driven transient burning experiments.

force, f, created by the mass efflux from the burning surface can be calculated as

$$f(t) = m(t)\, u_g(t)\,, \tag{2.8}$$

where m the mass efflux, and u_g the velocity of the gasses leaving the surface. This velocity can be calculated from a mass balance across the burning surface, $u_g(t) = m(t)/\rho_g$, where ρ_g the density of the gasses. This density can be calculated from the ideal gas equation. Finally it is found that [41]

$$f(t) = m^2(t)\,\frac{\Re T_f}{PM}\,, \tag{2.9}$$

where $\Re$ the gas constant, T_f the flame temperature, P the pressure and M the molecular weight of combustion products. For small perturbations ($'$) this can be modified to give the result

$$f'(t) = 2\bar{m}m(t)'\,\frac{\Re T_f}{PM}. \tag{2.10}$$

Thus, the measured small force perturbations are proportional to variations in the mass burning rate. The experimental problem is to measure these small fluctuations, which are on the order of 0.001 to 0.003 N/cm^2.

Another method for measuring the combustion response is the microwave Doppler technique [54]. This technique is based on the fact that propellant regression rate is directly proportional to the time rate of change of phase shift (ϕ) between incident microwave signal and reflected microwave signal,

$$m' = \frac{\partial \phi'}{\partial t}. \tag{2.11}$$

2.3.3 Optical characteristics of solid propellants.

As an approximation, radiation transmission as a function of the depth in the condensed phase obeys Beer's law [59]:

$$q_r(x) = q_r e^{-\bar{\bar{a}}_\lambda x}, \tag{2.12}$$

where q_r the radiant flux intensity, and $\bar{\bar{a}}_\lambda$ the volumetric absorption coefficient. The absorption coefficient is dependent on radiation wavelength and propellant nature.

Experiments with thin slides double-base propellants show that $\bar{\bar{a}}_\lambda = 1000$ cm^{-1}, for wavelengths in the range $10 - 14\,\mu$m. In the near infrared however, the transparency is much higher.

The determination of the effective transparency of the *heterogeneous* composite propellants is much more difficult. These propellants consist of a relatively transparent ammonium perchlorate (AP) crystals, and an opaque binder. At a wavelength of $10.6\,\mu$m for example, for the standard Hydroxyl Terminated PolyButadiene (HTPB) binder $\bar{\bar{a}}_\lambda = 500$ cm^{-1} [60], while an effective value of $\bar{\bar{a}}_\lambda = 64$ cm^{-1} was measured for the standard A-13 composite propellant (containing 76% AP). Often powdered metals are added in composite propellants resulting in an even more complex system.

Chapter 3

Flame modeling.

3.1 Introduction.

It was discussed in the previous chapter that the instable combustion of solid rocket propellants can be divided in acoustic and intrinsic instabilities. The intrinsic instability can be described by a thermal model which is presented in this chapter.

Figure 3.1 shows the burning of a solid rocket propellant schematically. For away from the burning surface, the propellant is at its initial temperature T_a. Due to reactions in the condensed phase and the conductive heating from the reactions in the gas phase, the temperature of the solid increases up to the surface temperature, T_s. At the surface gasification of the solid takes place. Above the surface, decomposition products of oxidizer and fuel react, until the gasses reach the flame temperature T_f. When the condensed phase moves with the burning rate $r_b(t)$ to the right, the surface will remain at a fixed position.

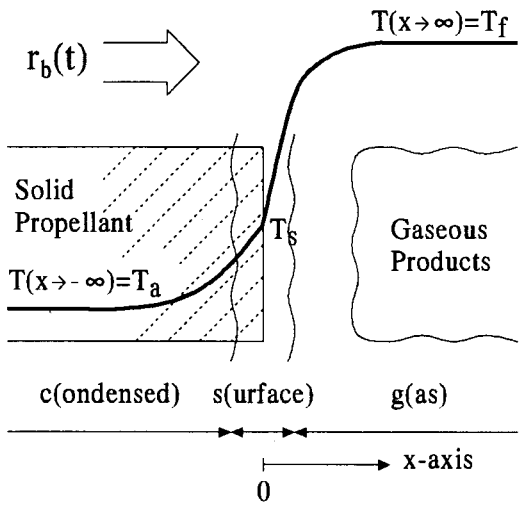

Figure 3.1: Schematic view of the overall physical problem.

For the problem to be tractable, several assumptions have to be made. The first one is that of monodimensionality in space, i.e. only a dependence of the x coordinate is assumed. Then the energy equation of the solid phase of figure 3.1 can be written as

$$\frac{\partial T}{\partial t} + r_b \frac{\partial T}{\partial x} = \alpha_c \frac{\partial^2 T}{\partial x^2} + Q \quad \text{for} \quad -\infty < x < 0 \,, \tag{3.1}$$

where t is the time. It has been assumed that the thermal diffusivity, α_c is temperature independent. The term Q describes the possible heat sources in the solid phase. As seen later this term can e.g. describe possible chemical reactions in the solid. By introducing equation 3.1 it was also assumed that the condensed phase is of homogeneous structure.

During steady state burning the time derivatives of equation 3.1 are canceled, and the solution of this equation for $Q = 0$ is (see appendix A.1)

$$T(x) = T_a + (T_s - T_a) e^{r_b x/\alpha_c} \quad \text{for} \quad -\infty < x \leq 0 \,, \tag{3.2}$$

where the boundary conditions $T(x \to -\infty) = T_a$ and $T(x = 0) = T_s$ have been used. So, in the condensed phase a thermal layer exists. Because of the limited thermal conductivity, and heat capacity of the condensed phase, this thermal layer has a certain inertia. When external time-dependent periodic disturbances perturb this thermal layer, resonant burning may occur, when the characteristic time of the condensed phase is equal to that of the disturbance. This is the basis for intrinsic instability.

In this chapter the governing general equations for the three regions of figure 3.1 are presented. As in most models the approach is based on the QSHOD framework (**Q**uasi-**S**teady gas phase **H**omogeneous **O**ne-**D**imensional). The exact meaning of each term will become clear in this chapter. Within this framework two approaches can be distinguished, the Zeldovich-Novozhilov (ZN) method as described in appendix C and the flame modeling (FM) method. The flame modeling approach calculates the time dependent burning of a propellant by modeling the conductive heat feedback from the gas phase to the solid phase and solving the energy equation of the solid phase. The Zeldovich-Novozhilov method uses experimentally determined burning rates to calculate the time dependent burning.

In this and the following chapters the following general assumptions are made. Consider a solid propellant burning in a vessel at uniform pressure and possibly subjected to a collimated radiant flux that originates exclusively from a continuous external source of thermal nature. Assume monodimensional processes, no photochemistry, and no external forces (e.g. acceleration). It is further assumed that there is no velocity coupling, i.e. the burning rate is independent of the velocity of gasses parallel to the combustion surface. Define a Cartesian x-axis with its origin anchored to the burning surface and positive in the gas phase direction, see figure 3.1.

With the theory of this chapter the linear and nonlinear response functions can be calculated. These calculations will be discussed in chapters 4 and chapter 6 respectively.

3.2 The condensed phase.

Let the condensed phase be a semi-infinite slab of uniform and isotropic composition, possibly suffering heat losses from the burning surface only. Assume that an external radiant flux irradiates the condensed phase.

The energy equation 3.1 can be written in a nondimensional form by nondimensionalising all the quantities involved. This is performed by dividing by those values associated with the steady state thermal layer in the condensed phase at a certain pressure. These reference values will denoted by a subscript ref, and are summarized in table D.1 of appendix D.

The thermal layer thickness in the condensed phase is characterized by the quantity α_c/r_b. So the nondimensional space coordinate, X, is defined as $X = x/(\alpha_{c,ref}/r_{b,ref})$, where x the space coordinate, and $\alpha_{c,ref}$ and $r_{b,ref}$ thermal diffusity and burning rate respectively, both at reference conditions.

Further, the nondimensional temperature is defined as $\Theta = (T - T_{ref})/(T_{s,ref} - T_{ref})$, where T temperature and T_s the surface temperature defined as $T_s = T(x = 0)$. With this definition $\Theta = 1$ at the surface under reference conditions, and $\Theta = 0$ at the cold boundary if T_{ref} is taken equal to T_a, as commonly done.

The nondimensional time, τ, is defined as as $\tau = t/(\alpha_{c,ref}/r_{b,ref}^2)$. This definition is based on the characteristic time parameter of the thermal wave, α_c/r_b^2.

When the previous assumption of constant thermal properties is dropped, the nondimensional energy equation in the condensed phase is given by the following nonlinear partial differential equation [18]

$$C_c(\Theta)\left[\frac{\partial\Theta}{\partial\tau} + R\frac{\partial\Theta}{\partial X}\right] = \frac{\partial}{\partial X}\left[K_c(\Theta)\frac{\partial\Theta}{\partial X}\right] + F_0\, f(X) + \epsilon_c(\Theta)\, H_c \quad \text{for} \quad -\infty < X < 0, \tag{3.3}$$

where C_c the specific heat of the condensed phase, $R = r_b/r_{b,ref}$ the nondimensional burning rate, K_c the thermal conductivity. Note that the source term Q has been divided further into two terms. The first one, $F_0 f(x)$, describes a possible external radiant flux, with nondimensional radiant heat flux amplitude F_0, and spatial dependence $f(X)$, e.g. Beer's law (equation (2.12)). The second term, $H_c\epsilon_c(\Theta)$ describes the heat release in the condensed phase because of subsurface chemical reactions. Again this term is written as a product of amplitude, H_c, and temperature (read spatial) dependence, $\epsilon_c(\Theta)$, describing the chemical reactivity. H_c is the total energy released in the condensed phase.

The initial condition is given by

$$\Theta(X, \tau = 0) = \Theta_i(X) \quad \text{for} \quad X < 0, \tag{3.4}$$

where Θ_i the initial temperature profile. The boundary conditions are

$$\Theta(X \to -\infty, \tau) = \Theta_a, \tag{3.5}$$

$$q_{c,s} = q_{g,s} + R\, H_s - q_{out}, \tag{3.6}$$

where Θ_a the temperature at the cold boundary of the propellant sample. Equation (3.6) is found from an energy balance at the surface. $q_{c,s}$ is the heat flux from the surface into the solid and $q_{g,s}$ is the heat flux from the gaseous phase into the surface. H_s is the heat release at the surface and q_{out} is the heat loss toward the surroundings, typically by radiation from the hot burning surface. The heat fluxes are defined as

$$q_{c,s} \equiv \left(K_c \frac{\partial \Theta}{\partial X} \right)_{c,s} \quad \text{and} \quad q_{g,s} \equiv \left(K_g \frac{\partial \Theta}{\partial X} \right)_{g,s} . \tag{3.7}$$

The heat loss can be modeled by Stefan-Boltzmann's law

$$q_{out} = \frac{\sigma \bar{\bar{\epsilon}}_\lambda (T_s^4 - T_a^4)}{\phi_{ref}}, \tag{3.8}$$

where $\bar{\bar{\epsilon}}_\lambda$ the average optical emissivity of the burning surface. Note that the heat loss is divided by the reference energy flux, ϕ_{ref}, to obtain a nondimensional quantity.

Due to the heating of the condensed phase, pyrolisis reactions take place in the condensed phase. Often these reactions are neglected because of the difficulty in modeling. An example of a model for these reactions in a DB propellant, is a two step process between the surface temperature, Υ_s, and some minimum temperature, Υ_{min}, below which no thermal degradation is assumed to occur. When Υ_{tra} is the transition temperature between the two pyrolysis steps, the group $H_c \epsilon_c$ is computed as [15].

$$H_c\,\epsilon_c = \begin{cases} H_{c,1}\, A_{c,1}\, e^{-E_{c,1}/\Upsilon} & \Upsilon_{tra} \le \Upsilon < \Upsilon_s \\ H_{c,2}\, A_{c,2}\, e^{-E_{c,2}/\Upsilon} & \Upsilon_{min} \le \Upsilon < \Upsilon_{tra} \\ 0 & -\infty < \Upsilon < \Upsilon_{min}, \end{cases} \tag{3.9}$$

where $E_{c,1}$ and $E_{c,2}$ activation energies. The pre-exponential factors $A_{c,1}$ and $A_{c,2}$ can be deduced through normalization conditions. The value of the total heat release in the solid phase ($H_{c,1} + H_{c,2}$ for the above equation) has to be obtained from experiments.

It was found by Zenin [61] e.g., that the measured total condensed phase heat release, H_c, for double base propellants is described by

$$\frac{H_c}{H_\Sigma} = c_1 - c_2 \exp^{-c_3 P/\sqrt{R}} , \tag{3.10}$$

where H_Σ the total heat release of the propellant. In the limit for high pressures $H_c = c_1 H_\Sigma$, i.e. the maximum heat release in the solid phase is a fraction of the total heat release of the propellant. An important conclusion can be drawn from this equation. It explains why more energetic propellants burn faster. Because of the proportionality $H_c \sim H_\Sigma$, and the obvious relation $R \sim H_c$, it is found that $R \sim H_\Sigma$.

3.3 The burning surface.

Assume that the burning occurs within an infinitesimally thin planar surface subjected to one-step irreversible gasification process. Two pyrolysis laws are accepted in the literature

for concentrated surface gasification, the classical exponential law by Arrhenius[1]

$$R(\Upsilon_s, P) = P^{n_s} \cdot \exp\left[-E_s\left(\frac{1}{\Upsilon_s} - 1\right)\right], \tag{3.11}$$

and the alternative power law by Krier et al. [33].

$$R(\Upsilon_s, P) = P^{n_s} \cdot \left(\frac{\Upsilon_s - \Upsilon_0}{1 - \Upsilon_0}\right)^{w_s}. \tag{3.12}$$

No strong experimental evidence exists for pressure effects on the pyrolysis phenomenon under steady operations, hence pressure dependence is usually neglected, i.e. $n_s = 0$.

The temperature dependence of the nondimensional net heat release concentrated at the burning surface is computed as

$$H_s(P, \Theta_s) = \bar{H}_s(P) + \int_{\bar{\Theta}_s(P)}^{\Theta_s} C_c(\Theta) d\Theta - C_g[\Theta_s - \bar{\Theta}_s(P)], \tag{3.13}$$

where C_g the heat capacity of the gaseous products, and the steady state quantity $\bar{H}_s(P)$ is experimentally deduced. It is shown in chapter 6 that H_s has a pronounced effect on the intrinsic instability of a propellant.

3.4 The gas phase.

The gas phase is considered to be semi-infinite and one-dimensional, extending from $X = 0$ to $X \to \infty$. Assume that the gas consists of a mixture of thermally perfect components, the gas is adiabatic everywhere except at the burning surface and does not interact with radiation. The flow is assumed to be one-phase, laminar, nonviscous, and low subsonic.

[1]This form may look strange, but is due to the normalizing by the reference conditions. The familiar (dimensional) form of the Arrhenius law is

$$r_b = A \cdot p^{n_s} \cdot \exp\left[-\frac{\tilde{E}_s}{\Re T_s}\right].$$

When this equation is divided by the Arrhenius law at reference conditions it is found that

$$R = \frac{r_b}{r_{b,ref}} = \left(\frac{p}{p_{ref}}\right)^{n_s} \cdot \exp\left[-\frac{\tilde{E}_s}{\Re T_{s,ref}}\left(\frac{T_{s,ref}}{T_s} - 1\right)\right] = P^{n_s} \cdot \exp\left[-E_s\left(\frac{1}{\Upsilon_s} - 1\right)\right].$$

Further, assume that the gas phase can be described by a thermal model (Lewis number $Le = 1$)[2].

Under these assumptions the nondimensional energy equation in the gas phase ($X > 0$, $\tau \geq 0$) is described by the following nonlinear partial differential equation

$$\frac{\rho_g}{\rho_c} C_g(\Theta) \left[\frac{\partial \Theta}{\partial \tau} + U \frac{\partial \Theta}{\partial X} \right] = \frac{\partial}{\partial X} \left[K_g(\Theta) \frac{\partial \Theta}{\partial X} \right] + \frac{\partial P}{\partial \tau} + \frac{\rho_g}{\rho_c} H_g \epsilon_g, \tag{3.14}$$

where ρ the density, and U the nondimensional gas velocity. The last term, $\rho_g/\rho_c H_g \epsilon_g$, describes the heat release rate in the gaseous phase due to chemical reactions of the reactive gasses. The total heat released in the gaseous phase is H_g, and the chemical reactivity is ϵ_g. The associated boundary conditions are

$$\Theta(X = 0^+, \tau) = \Theta_s, \tag{3.15}$$

$$\frac{\partial \Theta}{\partial X}(X \to \infty, \tau) = 0, \tag{3.16}$$

and initial condition

$$\Theta(X, \tau = 0) = \Theta_i(X) \quad \text{for} \quad X > 0, \tag{3.17}$$

During relaxation transients of solid propellants the gas phase adjusts much faster than the condensed phase, $t_g^* \ll t_c^*$ (t^* characteristic time). The validity of the quasi-steady assumption lies in the small gas-to-solid density ratio which implies that the transient time in the gaseous flame is much shorter than the response time of the heat transfer in the condensed phase [29] [55]. The quasi-steady assumption cannot be justified, neither at high frequencies, nor at high pressure burning, when the gas-to-solid density is not small enough to make the two relaxation times sufficiently different [9]. A typical frequency range for the quasi-steady approximation is from 0 to 1000 Hz. A quasi-steady gasphase approach needs in addition $t_g^* \ll t_{ext}^*$, where t_{ext}^* is the characteristic time of the external driving force. This requirement depends on the externally driven transient and may often be not true. Whenever a quasi-steady approach is used this inequality should be verified. In this approach the time derivatives are canceled in all gas phase equations, and initial conditions are no longer required. An example of a model including nonsteady gas phase effects is given by Clavin and Lazimi [9]. A further simplification of equation (3.14) is that $C_g(\Theta)$ and $K_g(\Theta)$ are taken constant.

It can be shown (see e.g. reference [37]) that the quasi-steady thermal heat flux from

[2]The Lewis number, Le, is defined as

$$Le = \frac{\alpha_g}{D} = \frac{\text{rate of energy transport}}{\text{rate of mass transport}},$$

where D the mass diffusitivity. When $Le = 1$ the two governing differential equations in the gas phase (energy conservation and species continuity) can be replaced by one differential equation and an algebraic equation. In combustible gas mixtures Le is often very nearly unity [36].

the gaseous phase into the solid is given by

$$q_{g,s}(P,R) = K_g \left(\frac{d\Theta}{dX}\right)_{X=0} = \int_0^\infty H_g \epsilon(X) \frac{\rho_g}{\rho_c} \exp\left[-\frac{C_g}{K_g} RX\right] dX. \tag{3.18}$$

The most difficult point is how to describe the chemical contribution $H_g \epsilon_g \rho_g / \rho_c$. Even simple propellant compositions have a very complex gas phase and treating the problem with chemical kinetics is virtually impossible. Because of this, modeling is required. The flame modeling (FM) method is named after this technique. Another approach of modeling is the ZN-approach which is described in appendix C. This method does not consider the flames, but depends on experimental burning rates for different initial temperatures.

Often the gas phase is divided into *two* parts:

1. A flame region, $X_i < X < X_f$. The chemical activity takes place here. In the quasi-steady approximation, and with above assumptions the quasi-steady energy equation (3.14) becomes (note that ∂ is replaced by d):

$$\frac{\rho_g}{\rho_c} C_g U \frac{d\Theta}{dX} = K_g \frac{d^2\Theta}{dX^2} + \frac{\rho_g}{\rho_c} H_g \epsilon_g. \tag{3.19}$$

2. A wake region, $X > X_f$. In this region there is no chemical activity anymore, so $H_g \epsilon_g = 0$. In this case equation (3.19) can be integrated to give a uniform in space, but time-dependent temperature profile,

$$\Theta(X > X_f, \tau) = \Theta_f(\tau). \tag{3.20}$$

Note that the differential equation for the steady state gas phase is time independent, but the solution is time dependent because of the time dependency of the boundary conditions.

In most cases $X_i = 0$, meaning that the flames are anchored to the burning surface. The focus of flame modeling is the modeling of the flame reaction layer. Often the models resort to simple mathematical functions to describe the space distribution of heat release (see sections 3.4.1 and 3.4.2).

Most detailed experimental investigations of the thermal wave structure in solid propellant combustion have been measurements of temperature profiles obtained by imbedding small thermocouples in propellant samples. All experiments show that the heat release under steady state operations is neither uniform, nor sharp in space, but rather features an elongated structure with a heat release rate very intense near the burning surface and gradually weakening in the tail. For the quasi-steady gas phase, the heat release distribution is assumed to be the same for transient and steady burning. A distinction must be made between homogeneous (DB) propellants and composite propellants.

Taking the experimental results into consideration, several flame models will be discussed next. The most simple model for the heat release rate, the KTSS flame, will be discussed first. After this section the more complicated $\alpha\beta\gamma$-model will be treated. This model covers all of the currently available transient flame models of thermal nature.

3.4.1 KTSS Flame Model.

From the previous section it becomes clear that an appropriate flame model has to be chosen, to be able to calculate the quasi-steady thermal heat flux from the gas phase into the solid phase. The KTSS flame is the most simple model.

The KTSS model developed by Krier et al. [33] assumes that the rate of product generation is uniformly distributed over the reaction zone, so that it can be modeled by a pulse function (see figure 3.2)

$$H_g \epsilon_g \frac{\rho_g}{\rho_c} = \bar{\omega}, \quad \text{for} \quad X_i \leq X \leq X_f. \tag{3.21}$$

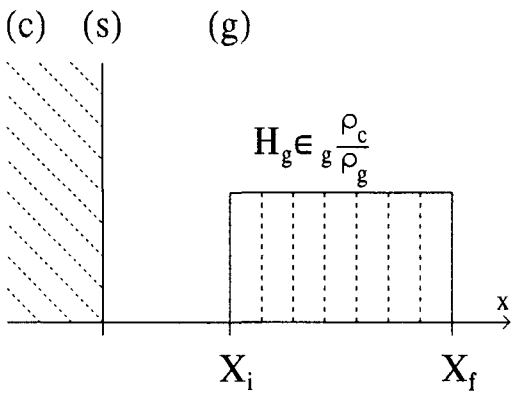

Figure 3.2: Schematic of heat release distribution by the KTSS-model.

The KTSS-flame can be seen as an example of *spacewise thick flames* (*broad chemical reaction zones* in the Soviet literature), and is physically representative of combustion processes controlled by mass diffusion.

The KTSS-flame is the most simple model of chemical reactivity in the gas phase. All other flame models are similar in approach. The differences between the KTSS model and other quasi-steady models lie in the spatial distribution of the gas phase heat release rate, the assumption of equal specific heats of gas phase and solid phase, and the pyrolysis law for gasification of the solid propellant.

In particular, a Dirac delta function was suggested to offer a convenient description of flames with a very large activation energy, see figure 3.3. Physically this kind of flame is representative of combustion processes controlled by chemical kinetics with a very large activation energy. An example of this work can be found in ref. [10]. These flame sheets are an example of *sharp flames* (*narrow chemical reaction zones* in the Soviet literature).

Also combinations of a rectangular pulse (KTSS-flame) with a delta function (flame-sheet) have been made [40]. This so called MTS-flame, accounts for chemical kinetics

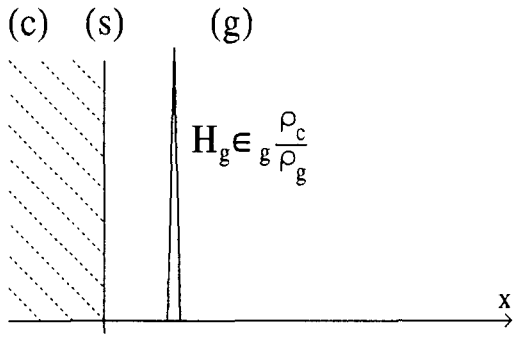

Figure 3.3: Schematic of heat release distribution by a Dirac delta function.

and mass diffusion in transient flames. In this work the concept of characteristic times is introduced.

In the next section the $\alpha\beta\gamma$-model is discussed. The heat release rate distribution of this model differs from the previous mentioned flames, in describing the heat release rate by a more complicated function.

3.4.2 The $\alpha\beta\gamma$-flame model.

The models for the heat release in the gaseous phase reviewed in the previous section, are far too simple to describe the processes actually taking place. Considering the temperature measurements mentioned earlier, DeLuca et al. [15] developed the so-called $\alpha\beta\gamma$-model. This mechanistic model accommodates different types of propellant flames by changing the parameters α, β and γ. In this approach for the heat release distribution $H_g \epsilon_g \frac{\rho_g}{\rho_c}$ it is assumed that

$$H_g \epsilon_g \frac{\rho_c}{\rho_g} = \begin{cases} H_g W \left(\beta + \frac{1-\beta}{\alpha} \frac{X}{X_f} \right) & 0 \leq X < \alpha X_f \\ H_g W \left(\frac{1-X/X_f}{1-\alpha} \right)^{\gamma} & \alpha X_f \leq X \leq X_f \,, \end{cases} \tag{3.22}$$

where W is the maximum value of the chemical mass reaction rate $\epsilon_g \rho_g / \rho_c$ per unit volume, αX_f the flame thickness fraction where W is located, βW is the fraction of the maximum chemical mass reaction rate per unit volume occurring at the gas-phase side of the burning surface, and γ is a power describing the decay of heat release for $X > \alpha X_f$, see figure 3.4.

By definition the three parameters depend on pressure and are bounded as follows:

$$0 \leq \alpha(P) \leq 1, \quad 0 \leq \beta(P) \leq 1, \quad \gamma(P) \geq 0. \tag{3.23}$$

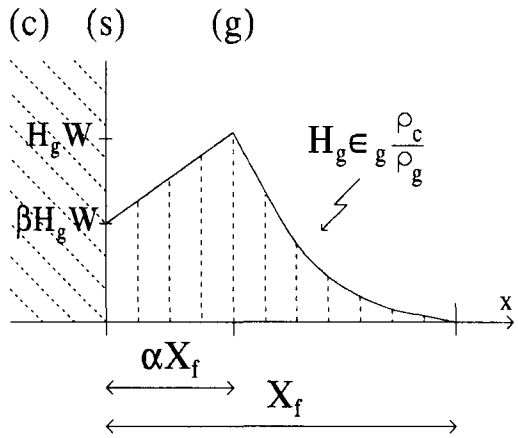

Figure 3.4: Schematic of heat release distribution by the $\alpha\beta\gamma$-model.

The value of parameter W can be found from the normalization condition

$$\int_0^{X_f} H_g \epsilon_g \frac{\rho_g}{\rho_c} dX = H_g R\,, \tag{3.24}$$

yielding

$$W(\tau) = \frac{R(\tau)}{X_f(\tau)} \frac{\gamma + 1}{1 + \alpha[\beta(\gamma + 1) + \gamma - 1]/2}\,. \tag{3.25}$$

To be able to calculate the flame length, X_f, of equation 3.22 characteristic time parameters of the gas phase have to be introduced. The quantity $< \tau_g' >$ is a characteristic gas phase time parameter, first defined by Summerfield and coworkers [40]

$$< \tau_g' > \equiv < \tau_g > \frac{C_g}{K_g} \frac{\rho_c}{< \rho_g >}\,, \tag{3.26}$$

where $< \tau_g >$ is the residence time in the gas-phase. The quasi-steady mass conservation across the burning surface and gaseous flame yields

$$< \tau_g > \equiv \frac{X_f}{< U >} = \frac{X_f}{R} \frac{< \rho_g >}{\rho_c}\,. \tag{3.27}$$

With the definition of equation (3.26), one finds

$$< \tau_g' > = \frac{C_g}{K_g} \frac{X_f}{R}\,. \tag{3.28}$$

For the $\alpha\beta\gamma$-model the integration in equation (3.18) from 0 to ∞, is replaced by an integration from 0 to X_f. With the above equation, the flame length X_f can be calculated, when the time parameter $< \tau_g' >$ is known.

Substituting the $\alpha\beta\gamma$-heat release distribution (equation (3.22)) in the formal integration of equation (3.18), yields the heat flux from the gas phase to the burning surface. It is found that

$$q_{g,s}(P,R) = \frac{H_g}{X_f(\tau)}\frac{K_g}{C_g}\frac{\gamma+1}{1+\alpha[\beta(\gamma+1)+\gamma-1]/2}F(\alpha,\beta,\gamma;R^2<\tau_g'>), \tag{3.29}$$

where

$$F(\alpha,\beta,\gamma;R^2<\tau_g'>) = \beta + \frac{1-\beta}{\alpha R^2<\tau_g'>} - \frac{(-1)^\gamma\gamma!}{(1-\alpha)^\gamma(R^2<\tau_g'>)^\gamma}\exp(-R^2<\tau_g'>)+$$

$$+\left[\sum_{i=1}^{\gamma}\frac{(-1)^i\gamma!}{(\gamma-i)!(1-\alpha)^i(R^2<\tau_g'>)^i} - \frac{1-\beta}{\alpha R^2<\tau_g'>}\right]\exp(-\alpha R^2<\tau_g'>). \tag{3.30}$$

In the derivation of these equations it has been assumed that γ is an integer. Notice that for $\alpha = 0$ (which necessarily implies $\beta = 1$), and $\gamma = 0$, the $\alpha\beta\gamma$-model exactly recovers the KTSS type of transient flame model. For $\gamma > 0$, the flame thickness associated with $\alpha\beta\gamma$-approach is $\gamma+1$ times larger than the thickness associated with KTSS type of flame. For $\alpha = 1$ and $\beta = 0$ (the value of γ is irrelevant is this case) the flame sheet type of flame model is obtained.

For the common case $\alpha = 0$ and $\beta = 1$, i.e. the maximum heat release rate is located at the burning surface, the above expression yields

$$q_{g,s}(P,R) = \frac{H_g}{X_f(\tau)}\frac{K_g}{C_g}(\gamma+1)F(\alpha=0,\beta=1,\gamma;R^2<\tau_g'>), \tag{3.31}$$

where

$$F(0,1,\gamma;R^2<\tau_g'>) = 1 - \frac{(-1)^\gamma\gamma!}{(R^2<\tau_g'>)^\gamma}\exp(-R^2<\tau_g'>) + \sum_{i=1}^{\gamma}\frac{(-1)^i\gamma!}{(\gamma-i)!(R^2<\tau_g'>)^i}. \tag{3.32}$$

Using this relations the linearized version of the $\alpha\beta\gamma$-model can be found easily ($F \to 1$). In case of $\gamma = 0$ the linearized KTSS flame is recovered ($q_{g,s} \propto 1/R$). These linearized relationships are useful for intrinsic stability analysis for small deviations from the steady state solution, see chapter 4.

The determination of the characteristic time of the gas phase is the most difficult task of the whole approach. An additional submodel is needed to determine this parameter. In general one can assume that

$$<\tau_g'(P,R,\cdots)> = f(P)g(R,\cdots)\,, \tag{3.33}$$

where the function f(P), can be determined from steady state operations, because of the quasi-steady assumption of the gas phase. A summary of the different possibilities in modeling g is given in reference [16], where expressions for nonaluminized AP-based propellants

and double base propellants are discussed. An extensive discussion on the modeling of double base flames with the $\alpha\beta\gamma$-model is given by DeLuca and Galfetti [17].

If only pressure dependence is assumed for the characteristic gas phase parameter, i.e. $< \tau_g' >=< \tau_g'(P) >$, its value can be obtained by a steady state energy balance written at the surface under adiabatic conditions. Due to the quasi-steadiness of the gas phase this calculated value can also be used in case of transient burning. The energy balance at the surface can be written as

$$\bar{q}_{g,s} = \bar{q}_{c,s} - \bar{R}\bar{H}_s. \tag{3.34}$$

With the equations (3.28), (3.31) and the first integral of the steady state energy equation in the solid phase, i.e.[3]

$$\bar{q}_{c,s} = \bar{R} \int_{\Theta_a}^{\bar{\Theta}_s} C_c(\Theta) d\Theta - \bar{R} \cdot \sum H_c \ , \tag{3.35}$$

the energy balance (equation 3.6) can be rewritten to give

$$< \tau_g' >= \frac{(\gamma+1)H_g}{\bar{R}^2 \left(\int_{\Theta_a}^{\bar{\Theta}_s} C_c(\Theta) d\Theta - \bar{H}_s - \sum \bar{H}_c \right)} F(\alpha = 0, \beta = 1, \gamma; \bar{R}^2 < \tau_g' >). \tag{3.36}$$

Solution of this equation requires an iterative loop as the equation is implicit in $< \tau_g' >$. The heat release in the gaseous phase, H_g, can be found from an energy conservation. In spirit of a quasi-steady gas phase, it is assumed that the steady state value of H_g can also be used for transient calculations,

$$H_g(P) = H_g(\bar{P}) = \int_{\Theta_a}^{\bar{\Theta}_s} C_c(\Theta) d\Theta + C_g(\bar{\Theta}_f - \bar{\Theta}_s) - H_s(\bar{P}) - \sum H_c. \tag{3.37}$$

In this section the $\alpha\beta\gamma$-model for the heat release in the gaseous phase was extensively discussed. The heat feedback from the gas phase to the burning surface was calculated for this model (equation 3.29). In the next chapters the $\alpha\beta\gamma$-model will be used in all calculations. By proper selection of the parameters α, β and γ, all other flame models of section 3.4.1 can be recovered.

[3]The steady state equation is the condensed phase is given by

$$\bar{R} C_c(\Theta) \frac{d\Theta}{dX} = \frac{d}{dX} K_c(\Theta) \frac{d\Theta}{dX} + H_c \epsilon_c(\Theta)$$

Integrating over the solid phase yields

$$\bar{R} \int_{\Theta_a}^{\bar{\Theta}_s} C_c(\Theta) d\Theta = K_c(\Theta) \frac{d\bar{\Theta}}{dX} + H_c \int_{-\infty}^{0} \epsilon_c(\Theta) dX.$$

From this equation, $\bar{q}_{c,s} \equiv K_c(\Theta) \frac{d\bar{\Theta}}{dX}$ can be calculated.

Chapter 4

Linear frequency response functions.

In this chapter the frequency response function of a burning propellant surface is considered, within the framework of a linear thermal theory. The extensive work on pressure driven frequency response functions is summarized by Culick [12]. The discussion of radiation driven frequency response functions is based on the work by Milfeith et al. [41] and Finlinson et al. [24].

We want to determine the fluctuation of the burning rate subject to an externally controlled perturbation, e.g. pressure or radiant fluctuations. The situation during transient burning is sketched in figure 4.1. The x-axis is anchored to the mean equilibrium position $x = 0$. The condensed phase moves with a speed $\bar{r}_b$ toward right, the surface fluctuates between two unknown locations, $x = s^-$ and $x = s^+$, because of burning rate fluctuations r_b'. Consider the assumptions of section 3.1 and assume also that the condensed phase is chemically inert and thermophysical properties are constant, i.e. $\epsilon_c(\Theta)H_c = 0$, and $K_c(\Theta) = C_c(\Theta) = 1$.

4.1 Condensed phase.

With the assumptions mentioned above, the *dimensional* energy equation for the solid phase (equation (3.3)), can be rewritten as:

$$\frac{\partial T}{\partial t} + \bar{r}_b \frac{\partial T}{\partial x} = \alpha_c \frac{\partial^2 T}{\partial x^2} + N_t \frac{\bar{\bar{a}}_\lambda}{\rho_c c_c}(1 - \bar{\bar{r}}_\lambda) I_0 e^{\bar{\bar{a}}_\lambda x}, \tag{4.1}$$

where α_c is the thermal diffusitivity defined as $\alpha_c = k_c/(\rho_c c_c)$, N_t is the radiation fraction absorbed below the surface layer, $\bar{\bar{a}}_\lambda$ is the volumetric absorption coefficient, $\bar{\bar{r}}_\lambda$ is the reflectivity of the surface layer, and I_0 is the external radiant flux intensity. Note that the transmission of the radiation is assumed to obey Beer's law (see equation (2.12)), with a spatially constant absorption coefficient $\bar{\bar{a}}_\lambda$. The natural radiant feedback from the flame to the solid is neglected.

Applying a linear perturbation of r_b, T, and I_0, the steady state form of the solid phase energy equation and the time-dependent energy equation can be obtained and solved,

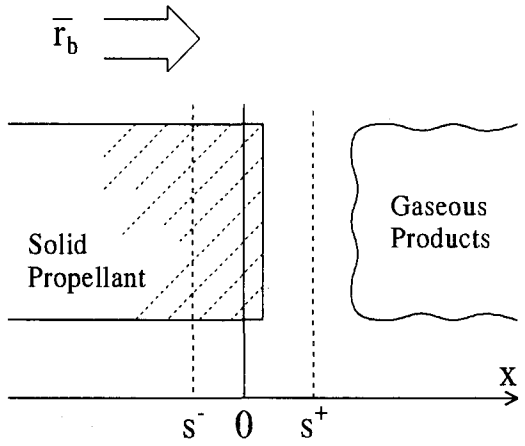

Figure 4.1: Surface of solid propellant during burning transients. The condensed phase moves with velocity $\bar{r}_b$ to the right. Due to the transients the surface can be seen to fluctuate between $x = s^-$ and $x = s^+$.

using the appropriate boundary conditions, see appendix A.1. The basic mathematical assumption of linear theories is that all time-dependent variables $(\ldots)$ can be expressed as the sum of a steady state value $(\bar{\ldots})$ and a small disturbance of the type $(\ldots)' \cdot e^{i\omega t}$. the amplitude of the disturbance has to be much smaller than the steady state counterpart, typically below 10% of the steady state value [52]. The temperature is assumed of the type

$$T(x,t) \;=\; \bar{T}(x) + T'(x) \cdot e^{i\omega t}, \tag{4.2}$$

where $\bar{T}(x)$ the steady state solution and $T'(x)$ has to be determined. Linearizing and solving the energy equation in the condensed phase it is found that [19] (for derivation see appendix A.1 and A.2)

$$T'(x) \;=\; T'_{x=0,c}\, e^{\lambda \bar{r}_b x/\alpha_c} + N_t \bar{I}_0 \frac{\dfrac{I'_0}{\bar{I}_0} + \dfrac{1}{l_r - 1}\dfrac{r'_b}{\bar{r}_b}}{\rho_c c_c \bar{r}_b \left(l_r - 1 - \dfrac{i}{\bar{r}_b}\dfrac{\omega}{\bar{\bar{a}}_\lambda} \right)} \left[e^{\lambda \bar{r}_b x/\alpha_c} - e^{\bar{\bar{a}}_\lambda x} \right] +$$

$$+ \frac{r'_b}{\bar{r}_b} \frac{\rho_c c_c \bar{r}_b (\bar{T}_s - T_0) + \dfrac{N_t \bar{I}_0}{l_r - 1}}{\rho_c c_c \bar{r}_b \, i\omega \dfrac{\alpha_c}{\bar{r}_b^2}} \left[e^{\lambda \bar{r}_b x/\alpha_c} - e^{\bar{r}_b x/\alpha_c} \right], \tag{4.3}$$

where, from now on, for convenience the factor $(1 - \bar{\bar{r}}_\lambda)$ was incorporated in the radiant flux intensity I_0, $l_r = \bar{\bar{a}}_\lambda \alpha_c / \bar{r}_b$ is the ratio of thermal to radiant layer thickness, and λ is the complex characteristic root defined as

$$\lambda(\lambda - 1) \;=\; i \frac{\omega \alpha_c}{\bar{r}_b^2} \;=\; i\,\Omega, \tag{4.4}$$

where Ω nondimensional circular frequency, see appendix A.2. To avoid divergence of the solution at the cold propellant boundary ($x \to -\infty$) only one solution of the two solutions of this equation is valid,

$$\lambda = \frac{1 + \sqrt{1 + 4i\omega\alpha_c/\bar{r}_b^2}}{2}. \tag{4.5}$$

As described above, the surface fluctuates between $x = s^-$ and $x = s^+$. Apply a Taylor's series to relate the variables at the $x = s$ position to those at the fixed surface ($x = 0$), to obtain the heat flux at the fluctuating surface on the solid phase side of the surface, see appendix A.2

$$\left(q'_{g,s}\right)_s \equiv k_c \left(\frac{dT'}{dx}\right)_s \simeq k_c \left(\frac{dT'}{dx}\right)_{0-} + k_c s \left(\frac{d^2\bar{T}}{dx^2}\right)_{0-} + \ldots. \tag{4.6}$$

From the mass balance it can be shown that

$$\frac{\rho_c s}{\bar{m}} = -\frac{1}{i\omega}\frac{m'}{\bar{m}}, \tag{4.7}$$

for harmonically varying fluctuations.

As shown by Finlinson et al. [24] the transient heat flux (on the solid phase side of the surface) is found to be

$$k_c \left(\frac{dT'}{dx}\right)_{s-} = \bar{m} c_c \lambda T'_s + \frac{m'}{\bar{m}}\left[\frac{\bar{m} c_c (\bar{T}_s - T_0)}{\lambda}\right] - \frac{m'}{\bar{m}}\left[N_t \bar{I}_0 \frac{1-\lambda}{\lambda(1-\lambda-l_r)}\right] + \frac{I'_0}{\bar{I}_0}\left[\frac{N_t \bar{I}_0 l_r}{1-\lambda-l_r}\right]. \tag{4.8}$$

A derivation of this equation is presented in appendix A.2. The first two terms on the right hand side are the familiar terms that appear in all studies where radiant heat flux is not considered. The last two terms originate from the external radiant heat flux.

4.2 Surface connection relations.

The surface reaction layer is assumed to be infinitely thin at the surface. The perturbed energy balance at the surface (equation (3.6)) is given by

$$\left(q'_{g,s}\right)_{s+} = \left(q'_{c,s}\right)_{s-} - m'\bar{Q}_s + \bar{m}(c_g - c_c)T'_s - (1 - N_t)I'_0, \tag{4.9}$$

where $\bar{Q}_s$ is the sum of all heats of melting, vaporization and subsurface reactions per unit mass of propellant. As in most calculations $\bar{Q}_s$ is assumed to be pressure and temperature independent. The last therm on the right hand side expresses the amount of radiant energy absorbed by the surface layer.

The mass consumption (m) matching condition for the steady state is

$$\bar{m}_s = \bar{m}_g = \bar{m}, \tag{4.10}$$

where $\bar{m} = \rho_c \bar{r}_b$, for the fluctuating portion this is

$$m'_s = m'_g = m'. \tag{4.11}$$

Arrhenius surface pyrolysis (see equation (3.11)) provides the temperature fluctuation as

$$\frac{T'_s}{\bar{T}_s} = \frac{1}{\tilde{E}_s} \cdot \frac{m'_s}{\bar{m}_s}, \tag{4.12}$$

whereas the power law by Krier et al, (equation (3.12)) provides the temperature fluctuation as

$$\frac{T'_s}{\bar{T}_s} = w_s \frac{\bar{T}_s - T_0}{T_0} \frac{m'_s}{\bar{m}_s}. \tag{4.13}$$

See appendix A.3 for a derivation of the equations (4.12) and (4.13).

4.3 Gas phase.

The gas phase energy term is obtained from equation (3.19), but requires modeling of the volumetric mass reaction rate. In section 3.4 several heat release models were discussed. For the linearized calculations is is necessary to use linearized expressions of the heat feedback from the gaseous phase. Following DeLuca et al. [19], it is assumed that the heat feedback from the gas phase is given by the $\alpha\beta\gamma$-model as described in section 3.4.2, for $\alpha = 0$, and $\beta = 1$. The dimensional form of equation (3.31) can then be written as

$$\left(q'_{c,s}\right)_{s+} = mQ_g \frac{\gamma + 1}{\zeta_f} F(\gamma, \zeta_f), \tag{4.14}$$

where $\zeta_f = mc_g/k_g x_f$ a nondimensional position. This heat feedback describes distributed flames with the maximum heat release just at the burning surface. This thesis concentrates on the condensed phase and no derivation of the linearized heat feedback is given. For detailed information see e.g. reference [11].

4.4 Pressure-driven frequency response function.

The pressure-driven frequency response function is defined in equation (2.1). From the equations (4.9), (4.8), and (4.14) the pressure driven response function for distributed flames can be calculated [19]. Cast in the "two parameter" form (with parameters A and B) it becomes

$$R_p(\omega) = \frac{nAB_p + n_s(\lambda - 1)}{\lambda + \frac{A}{\lambda} - (1 + A) + AB_p}, \tag{4.15}$$

where λ is defined in equation (4.5), n is the burning rate exponent, n_s is the pressure exponent in the Arrhenius pyrolysis law, $A = (1 - T_0/\bar{T}_s)\tilde{E}_s/R\bar{T}_s$ is the normalized activation

energy for the surface reactions, which is characteristic of the solid phase only, and varies with the approach [12]. B is a parameter whose value depends on the model used for the gas phase. For the current case

$$B_p = B_p(\gamma) \equiv \frac{1}{n}\left[W_p(\gamma) + \frac{c_g}{c_c}\frac{n_s}{A}\right] \tag{4.16}$$

$$W_p(\gamma) \equiv n\frac{(\gamma+1)(1-\frac{2\gamma}{\bar{\zeta}_f})\frac{H_g}{\bar{\zeta}_f}[2+\frac{\bar{T}_s}{E_s}(\frac{g_{T_s}}{g}+\frac{n_s}{n}\frac{g_{T_f}}{g})]+\frac{c_g}{c_c}\frac{1-n_s/n}{A}}{1-(\gamma+1)(1-\frac{2\gamma}{\bar{\zeta}_f})A\frac{H_g}{\bar{\zeta}_f}\frac{c_c}{c_g}\frac{\bar{T}_s}{E_s}\frac{g_{T_f}}{g}}, \tag{4.17}$$

where the subscripts T_s and T_f denote the derivative of g (as defined in equation (3.33)) with respect to T_s and T_f respectively.

Culick [12] showed that all linearized pressure-driven response functions can be cast in the above "two parameter" form. This common result is a consequence of several basic assumptions [3]:

1. The assumption of a homogeneous solid phase with constant thermal properties.
2. A quasi-steady gas phase restricting the analyses to the frequency range in which the gas phase responds much faster than the solid.
3. The assumption that a one-dimensional description is adequate.
4. Neglect of condensed phase reactions.

Figure 4.2 shows a typical response function for $A = 14$, $B = 0.8$, $n = 0.5$, $n_s = 0$ and $n_s = 1$. For low frequencies the response functions goes to the static limit given by equation (2.6). For $\Omega \rightarrow \infty$ the response function tends towards zero, since the intertia of the system becomes more and more important for faster change of the applied sinusoidal pressure.

4.5 Radiation-driven frequency response function.

From the equations (4.9), (4.8), and (4.14) the radiation driven response function for distributed flames can be calculated [19]

$$R_q(\omega) = \frac{n_q A B_q \frac{(1-N_t)(1-\lambda)-l_r}{1-\lambda-l_r}}{\lambda+\frac{A}{\lambda}-(1+A)+AB_q-n_qAB_q\frac{N_t(1-\lambda)}{\lambda(1-\lambda-l_r)}}, \tag{4.18}$$

being

$$B_q = B_q(\gamma) \equiv B_p(\gamma) + \bar{q}_r = \frac{1}{n}[W_p(\gamma) + \frac{c_g}{c_c}\frac{n_s}{A}] + \bar{q}_r, \quad \text{and} \quad n_q \equiv \frac{\bar{q}_r}{B_q(\gamma)}, \tag{4.19}$$

where q_r the nondimensional external heat flux given by $q_r = I_0/[\rho_c c_{ref}\bar{r}_b(\bar{T}_s - T_{ref})]$.

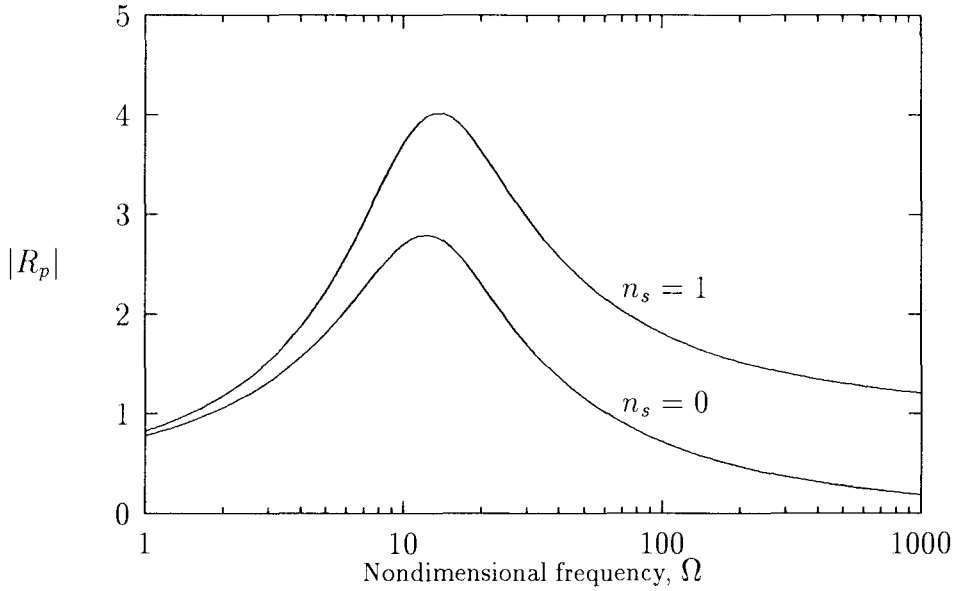

Figure 4.2: Response function for $A = 14$, $B = 0.8$, $n = 0.5$, $n_s = 0$ and $n_s = 1$.

4.6 Transfer function.

It was explained in section 2.3 that the determination of the pressure driven response functions through radiation tests simplifies the experimental setup. However a relation beteen the pressure driven and radiation driven response functions has to be known, to be able to experimentally determine the pressure driven frequency response functions from these radiation tests. The relation between the two response functions is given by the *Transfer Function* (TF). A convenient definition of the normalized TF is

$$TF(\omega) \equiv \frac{R_q(\omega)/R_q(\omega = 0)}{R_p(\omega)/R_p(\omega = 0)}, \tag{4.20}$$

which can immediately be computed from the previous relationships. In general, TF is a complex function whose magnitude and shape depend on the propellant nature and the specific set of operating conditions. A very simple result if found for $n_s = 0$, fully opaque condensed phase at the working wavelength(s), and negligible average radiant flux. For this situation $TF = 1$ implying that there is only a scale factor between the normalized pressure driven and radiation driven frequency response functions. An example of such a derivation is given by Strand et al. [54].

4.7 Summary of the assumptions.

In the previous sections the linearized pressure driven and radiation driven frequency response functions were derived. In this derivation several assumptions were made. These assumptions are summarized below:

- **Overall problem:**
  - The problem is treated homogeneous.
  - The problem is treated one-dimensional.
  - Velocity coupling is neglected.
  - No external forces.
  - No photochemistry.
  - External radiant heat flux is of thermal nature.
  - Natural radiant feedback from the gasses to the solid is neglected.
  - Constant thermal properties.
- **Condensed phase:**
  - Isotropic composition.
  - No chemical reactions.
  - Absorption of the radiation obeys Beer's law.
- **Surface layer:**
  - Surface is considered to be infinitesimally thin.
  - Pyrolysis is described by an Arrhenius law.
- **Gas phase:**
  - Quasi-steady gas phase.
  - Gas flow is laminar, nonviscous, one-phase, and low subsonic.
  - Gas phase is described by a thermal model with Lewis number $Le = 1$.
  - Flame model describes distributed flames featuring the maximum heat release just at the burning surface.

From the list above it becomes clear that a lot of assumptions are necessary to allow for an analytical calculation of response functions. Some of these approximations will have a large effect on the response function as will be shown in chapter 6. In that chapter the assumptions of constant thermophysical properties in the condensed phase, and the nonreacting condensed phase are dropped.

Another disadvantage of the linearized models lies in the linear approximation. Simple nonlinear systems can behave unpredictable in contradiction to their linear counterparts. This also applies for rocket motors and the combustion processes therein. Chapter 6 will show the effect of the linearization, and its validity.

Chapter 5

Model for the transient burning of AP-composites.

Most transient combustion models neglect the solid phase reactions. Deluca et al. [17] developed a two step reaction process for double base propellants. In the solid phase of ammonium perchlorate (AP) based composite propellants also reactions take place. In addition there are two phase transitions of AP in the temperature range of interest. The first is the crystalline transformation of orthorombic AP to cubic AP which occurs at 513 K [8]. Due to this transition the properties of the propellant change abruptly. The thermal conductivity is reduced by approximately a factor three. The density of the AP crystals changes from 1.95 g/cm^3 to 1.76 g/cm^3. This transition from cubic to orthorombic is endothermic requiring 21.3 cal/g (89.1 J/g). The second transition occurs at a temperature of 723 K, when the AP starts to melt. This transition is also endothermic, requiring 59.6 cal/g (249 J/g). See appendix D for a detailed description of the thermophysical properties of AP-composites.

From the discussion above it becomes clear that the treatment of the condensed phase as nonreacting with constant thermal properties is a very crude approximation of the processes actually taking place. In the next section a model for the condensed phase which accounts for these processes is presented.

5.1 Model for a reacting condensed phase.

In figure 5.1 a schematic view of the system considered is given. Far away from the burning surface ($X \to -\infty$), the propellant has its initial temperature Θ_a. The solid is heated due to conductive heat transfer from the gas phase.

At $X = X_{tra}$ the solid reaches the crystalline transition temperature of AP. At this point the latent heat of transition is withdrawn from the solid. The boundary condition at this point can be expressed as

$$\left[K_c(\Theta)\frac{\partial\Theta}{\partial X}\right]_{X_{tra}^-} = \left[K_c(\Theta)\frac{\partial\Theta}{\partial X}\right]_{X_{tra}^+} + RH_{tra}\,, \tag{5.1}$$

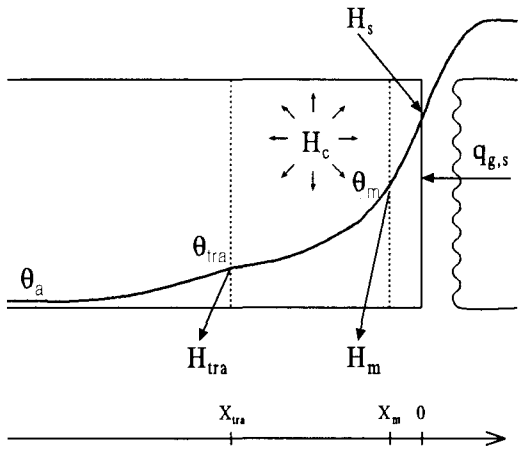

Figure 5.1: Schematic of the temperature distribution in an AP-propellant.

where H_{tra} the latent heat of the crystallographic-phase transition ($H_{tra} < 0$). In the cubic zone the temperature of the solid increases further, until the melting temperature of AP is reached. Like the previous phase transition this transition requires energy,

$$\left[K_c(\Theta)\frac{\partial\Theta}{\partial X}\right]_{X_m^-} = \left[K_c(\Theta)\frac{\partial\Theta}{\partial X}\right]_{X_m^+} + RH_m\,, \tag{5.2}$$

where X_m the point where the melting occurs, and H_m the latent heat accompanying the melting of AP ($H_m < 0$).

Measurements show that the surface temperatures for composite propellants are well above the typical degradation temperatures of the binder and the oxidizer [57], so chemical reactivity in the condensed phase is expected. These subsurface reactions can be modeled by a first-order Arrhenius equation,

$$H_c\epsilon_c(X) = H_cA_c(P)\exp\left(-\frac{\tilde{E}_c}{\Re T(x)}\right)\,, \tag{5.3}$$

where $\epsilon_c(X)$ is the chemical reaction rate, and H_c is the total heat release in the solid due to the reactions. The activation energy E_c has a typical value of 30 kcal/mole (125 kJ/mole) for composite propellants [35]. Because of the high value of E_c the chemical reactivity falls to exponentially small values even at short distances from the surface. The maximum surface temperature is about 1000 K, so the chemical reactivity at the surface is orders of magnitude larger ($10^5 \sim 10^6$) than at the transition point. From this it is seen that it is justified to neglect chemical reaction in the orthorombic zone. $A_c(P)$ is found

from the normalization condition [18]

$$\int_{-\infty}^{0} H_c \epsilon_c(X) dX = H_c R \,, \tag{5.4}$$

yielding,

$$A_c(P) = \frac{R}{\int_{X_{tra}}^{0} \exp\left[-\tilde{E}_c/\Re T(X)\right] dX} \,. \tag{5.5}$$

5.2 Summary of the equations.

In the model described above the energy equation for the condensed phase (equation (3.3)) becomes a set of equations, coupled by the energy conservation equations across the transition surfaces (equations (5.1) and (5.2)). If it is further assumed that the absorption of the external radiation obeys Beer's law, then this set can be written as

$$\begin{aligned} C_c(\Theta)\left[\frac{\partial\Theta}{\partial\tau} + R\frac{\partial\Theta}{\partial X}\right] &= \frac{\partial}{\partial X}\left[K_c(\Theta)\frac{\partial\Theta}{\partial X}\right] + \frac{1-\bar{\bar{r}}_\lambda}{\delta_a} F_0 e^{X/\delta_a} + \\ &+ \begin{cases} 0 & \text{for } -\infty < X < X_{tra} \\ H_c \epsilon_c(\Theta) & \text{for } X_{tra} < X < 0 \end{cases} \,, \end{aligned} \tag{5.6}$$

where δ_a the optical layer thickness, defined as $(1/\bar{\bar{a}}_\lambda)/(\alpha_c/r_{b,ref})$.

On the cold boundary side, $X \to -\infty$, the boundary condition is given by

$$\Theta(X \to -\infty, \tau) = \Theta_a \,. \tag{5.7}$$

On the burning surface the energy balance (see equation (3.6)) yields the boundary condition

$$\left[K_c(\Theta)\frac{\partial\Theta}{\partial X}\right]_{c,s} = q_{g,s} + RH_s \,, \tag{5.8}$$

where the energy loss due to radiation has been neglected. For typical propellants the emissivity is 0.85 [50] and with this value the radiation contributes less then 0.5% to the energy equation, so it is justified to neglect this term.

The burning rate R is found from an Arrhenius law, as given by equation (3.11). The surface heat release is found from equation (3.13). Unless noted otherwise, the gas phase is modelled by the $\alpha\beta\gamma-$model with $\alpha = 1$ and $\beta = 0$, see section 3.4.2.

Chapter 6

Numerical calculations of non-steady burning.

6.1 Transformation of the problem.

As derived in appendix A.1 for the steady state, the thermal profile in the condensed phase is exponential. Such a profile is characterized by steep gradients near the burning surface, and is varying slowly near the cold boundary. For the numerical computations to be performed efficiently it is necessary to either use a nonuniform mesh size or to use a scale transformation. Because of the exponential profile in the solid phase, an exponential transformation first proposed by Sills [53] is very appropriate. This transformation maps the semi-infinite domain, $-\infty < X < 0$, into the finite region $-1 < X' < 0$, and is given by

$$X' = e^{\beta X} - 1 \ . \tag{6.1}$$

This transformation is shown in figure 6.1. From this figure it can be seen that intervals near the origin are enlarged, and intervals far away from the origin are reduced. Note that this transformation has an explicit inverse relation. Another advantage of this transformation is that the boundary condition at the cold side may be imposed directly as opposed to being satisfied asymptotically.

Transformation of the energy equation (5.6), and its boundary conditions (equations (5.1), (5.2), (5.7), and (5.8)), yields

$$\begin{aligned} C_c(\Theta)\left[\frac{\partial\Theta}{\partial\tau} + R\beta(X'+1)\frac{\partial\Theta}{\partial X'}\right] &= \beta^2(X'+1)\frac{\partial}{\partial X'}\left[K_c(\Theta)(X'+1)\frac{\partial\Theta}{\partial X'}\right] + \\ +\frac{1-\bar{r}_\lambda}{\delta_a}F_0(X'+1)^{1/(\beta\delta_a)} &+ \begin{cases} 0 & \text{for } -\infty < X' < X'_{tra} \\ H_c\epsilon_c(\Theta) & \text{for } X'_{tra} < X' < X'_m \end{cases} , \qquad (6.2) \\ \Theta(X=-1,\tau) &= \Theta_a \ , \qquad (6.3) \\ \left[K_c(\Theta)\beta\frac{\partial\Theta}{\partial X'}\right]_{X'^-_{tra}} &= \left[K_c(\Theta)\beta\frac{\partial\Theta}{\partial X'}\right]_{X'^+_{tra}} + RH_{tra} \ , \qquad (6.4) \end{aligned}$$

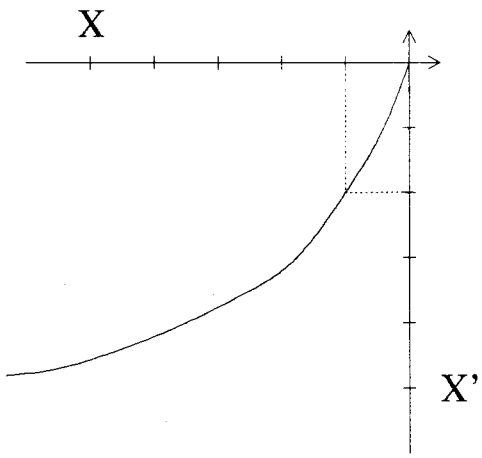

Figure 6.1: Illustration of the transformation.

$$\left[K_c(\Theta)\beta\frac{\partial\Theta}{\partial X'}\right]_{X'^{-}_m} = \left[K_c(\Theta)\beta\frac{\partial\Theta}{\partial X'}\right]_{X'^{+}_m} + RH_m \ , \tag{6.5}$$

$$\left[K_c(\Theta)\beta\frac{\partial\Theta}{\partial X'}\right]_{c,s} = q_{g,s} + RH_s \ . \tag{6.6}$$

For accurate calculations it is desirable to use a large value of β, so the intervals near the burning surface are greatly stretched. However, there is an upper limit which bounds the maximum value of β. The steady-state temperature profile in the condensed phase is given by equation (A.14). In the new coordinates this becomes

$$\bar{\Theta}(X') = \Theta_a + (\bar{\Theta}_s - \Theta_a)(X'+1)^{\bar{R}/\beta} + \frac{1-\bar{\bar{r}}_\lambda}{\bar{R}-1/\delta_{rad}}\left[(X'+1)^{1/\beta\delta_{rad}} - (X'+1)^{\bar{R}/\beta}\right] \ . \tag{6.7}$$

Differentiating this equation with respect to X' yields

$$\frac{\partial\bar{\Theta}(X')}{\partial X'} = (\bar{\Theta}_s - \Theta_a)\frac{\bar{R}}{\beta}(X'+1)^{\bar{R}/\beta} + \tag{6.8}$$

$$+ \frac{1-\bar{\bar{r}}_\lambda}{\bar{R}-1/\delta_{rad}}\left[(\frac{1}{\beta\delta_{rad}} - 1)(X'+1)^{(1/\beta\delta_{rad})-1} - (\frac{\bar{R}}{\beta} - 1)(X'+1)^{(\bar{R}/\beta)-1}\right] \ .$$

This derivative has to be bounded at the cold boundary, i.e. at $X' = -1$

$$\lim_{X'\downarrow -1}(X'+1)^{\bar{R}/\beta} \neq \pm\infty \ \Rightarrow \ \beta \leq \bar{R} \ , \tag{6.9}$$

$$\lim_{X'\downarrow -1}(X'+1)^{1/\beta\delta_{rad}} \neq \pm\infty \ \Rightarrow \ \beta \leq \frac{1}{\delta_{rad}} \ . \tag{6.10}$$

This derivation only holds for the analytical solution, however calculations by Galfetti et al. [25] show that with this condition reliable numerical solutions are also obtained for systems which can not be solved analytically.

For brevity the primes are not longer printed from now on.

6.2 Finite difference approximation.

The transformed set of equations was first solved using the common Crank-Nicholson finite-difference method. This method assumes constant mesh size in the transformed space and implicit finite-difference schemes. However, the calculations showed that this method was not able to accurately calculate the combustion transients, unless a fine space grid, and small time step were used. Because this turned out to be very inefficient, an other implicit method, as suggested by Galfetti et al. [25], was used. This scheme is described in reference [45] (page 191, scheme 13), and is shown in figure 6.2. The space coordinate is discretisized by NX grid points; $j = 1$ at the burning surface to $j = NX$ at the cold end. The time level is noted as n, $n+1$ indicating the current (unknown) timestep, n the previous time step, etc.

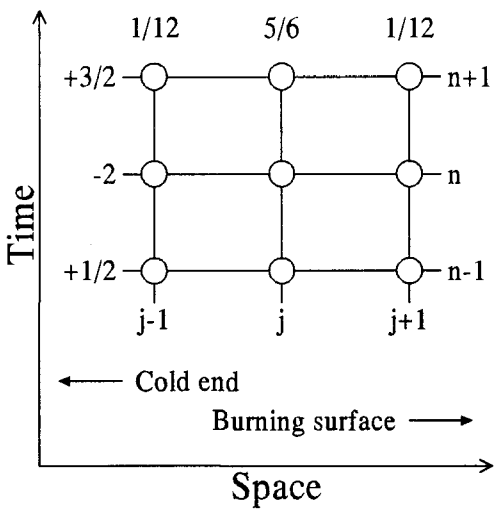

Figure 6.2: Schematic of the computational molecule.

To improve stability of the time derivative, the time derivative is approximated by a weighted average of the points next to the point to be solved

$$\frac{\partial \Theta}{\partial \tau} \simeq \frac{1}{\Delta \tau}\left[\frac{1}{12}(\Theta_w)_{j+1} + \frac{5}{6}(\Theta_w)_j + \frac{1}{12}(\Theta_w)_{j-1}\right] , \tag{6.11}$$

where Θ_w is the time derivative at a fixed position, calculated from

$$(\Theta_w)_j = \frac{3}{2}\Theta_j^{n+1} - 2\Theta_j^n + \frac{1}{2}\Theta_j^{n-1} . \tag{6.12}$$

The convective term is approximated by forward differences

$$R(P,\Upsilon_s)\beta[X+1]\frac{\partial\Theta}{\partial X} \simeq R(P^{n+1},\Upsilon_s^k)\beta[X_j+1]\frac{\Theta_{j-1}^{n+1}-\Theta_j^{n+1}}{\Delta X}\ , \tag{6.13}$$

where the superscript k indicates the estimated temperature profile. This temperature profile is necessary to be able to calculate the temperature dependent properties at each grid point. The diffusive term is approximated by central differences

$$\beta^2(X+1)\frac{\partial}{\partial X}\left[K_c(\Theta)(X+1)\frac{\partial\Theta}{\partial X}\right] \simeq \frac{\beta^2}{(\Delta X)^2}(X_j+1)\left[K_c(\Theta_{j-1/2}^k)\cdot\right.$$

$$\left.\cdot(X_{j-1/2}+1)(\Theta_{j-1}^{n+1}-\Theta_j^{n+1}) - K_c(\Theta_{j+1/2}^k)(X_{j+1/2}+1)(\Theta_j^{n+1}-\Theta_{j+1}^{n+1})\right]\ . \tag{6.14}$$

Following Nogotov [42], the thermal properties between the grid points ($j \pm \frac{1}{2}$), are calculated as

$$K_c(\Theta_{j\pm1/2}^k) = K_c(\frac{1}{2}(\Theta_j^k+\Theta_{j\pm1}^k))\ . \tag{6.15}$$

Substitution of these approximations in equation (6.2) yields the finite difference form of the energy equation

$$-A_j\Theta_{j+1}^{n+1} + B_j\Theta_j^{n+1} - C_j\Theta_{j-1}^{n+1} = D_j\ . \tag{6.16}$$

For the definition of the coefficients A, B, and C, see appendix B.1. This equation is applied to all points of the grid, except for the boundaries and at the transition points X_{tra} and X_m, leading to a linear set of equations, whose coefficients can be cast in a tridiagonal matrix.

At the cold boundary side ($j = NX-1$), equation (6.16) is rewritten to fit in a tridiagonal form using the boundary condition

$$\left.\begin{array}{l} -A_{NX-1}\Theta_{NX}^{n+1} + B_{NX-1}\Theta_{NX-1}^{n+1} - C_j\Theta_{NX-2}^{n+1} = D_{NX-1} \\ \Theta_{NX} = \Theta_a \end{array}\right\} \Longrightarrow$$

$$B_{NX-1}\Theta_{NX-1}^{n+1} - C_j\Theta_{NX-2}^{n+1} = D_{NX-1} + A_{NX-1}\Theta_a\ . \tag{6.17}$$

The boundary condition at the burning surface (equation (6.6)) is evaluated from

$$\left(\frac{\partial\Theta}{\partial X}\right)_{X=0^-} = \frac{1}{K_c(\Theta_{3/2}^k)\beta}\left\{q_{g,s}(P^{n+1},\Theta_1^k) + R(P^{n+1},\Upsilon_1^k)H_s(P^{n+1},\Theta_s^k)\right\}\ , \tag{6.18}$$

where the surface derivative is evaluated using a four point forward formula

$$\left(\frac{\partial\Theta}{\partial X}\right)_{X=0^-} = \frac{11\Theta_1^{n+1} - 18\Theta_2^{n+1} + 9\Theta_3^{n+1} - 2\Theta_4^{n+1}}{6\Delta X}\ . \tag{6.19}$$

With these equations Θ_1^{n+1} can be eliminated from equation (6.16), for $j = 2$. The resulting equation can be made tridiagonal by subtracting a suitable multiple of equation (6.16), for $j = 3$.

The condition at the transition points (X_{tra} and X_m) is approximated by replacing the partial derivatives by the first order approximations, e.g. equation (6.4) becomes

$$K_c(\Theta^k_{jtra+1/2})\frac{\Theta^{n+1}_{jtra} - \Theta^{n+1}_{jtra+1}}{\Delta X} = K_c(\Theta^k_{jtra-1/2})\frac{\Theta^{n+1}_{jtra-1} - \Theta^{n+1}_{jtra}}{\Delta X} + R(P^{n+1}, \Upsilon^k_s)H_{tra} \ , \quad (6.20)$$

where $jtra$ is the grid position where the transition takes place. This equation is in tridiagonal form, and can be solved along with the other equations, however $jtra$ is unknown and must be solved iteratively until the condition $\Theta^{n+1}_{jtra} = \Theta_{tra}$ is satisfied. The equations describing the melting of AP are analogous. The resulting equation is in a tridiagonal form, and is solved using the "Thomas algorithm', which is described in appendix B.2.

To determine the initial condition to start the transient computations the steady state solution is calculated first. The steady state calculations are also solved with finite-difference procedures, instead of the familiar Runge-Kutta methods for ordinary differential equations. The finite-difference method yields a more compact code, because the same procedures used for transient burning can be applied. This method is as fast as the Runge-Kutta methods [25].

6.3 Implementation in software.

The model as described previously was implemented in FORTRAN-77 because of it's portability and speed. Figure 6.3 shows the concept of the program. After initialization, the steady-state situation is calculated. This condition serves as a starting point for the transient calculations, which is then perturbed by a prescribed time dependent (e.g. sinusoidal) pressure and/or radiation disturbance with frequency f. From the response of the propellant on these perturbations the pressure and radiation driven response function can be calculated for the frequency f. These calculations are repeated for several frequencies and yield as output the frequency plots of the two response functions and the transfer function. The calculation of the response function from the propellants response is explained later on (see section 6.5.3).

As described earlier the steady-state and the transient temperature profiles are calculated in an analogous way. Figure 6.4 shows a flow chart of the temperature profile computation method. This part of the program is executed during steady-state calculations and during the determination of the response of the propellant on a perturbing signal.

Because the thermophysical properties are temperature dependent it is necessary to estimate the thermal profile (Θ^k) to be able to calculate the finite-difference coefficients at each grid point. If a steady-state calculation is performed this initial profile is estimated by the analytical solution (see equation (A.14)). For transient calculations the profile is estimated by a linear extrapolation of the previous two time steps, according to

$$\Theta^k_j = 2\Theta^n_j - \Theta^{n-1}_j; . \quad (6.21)$$

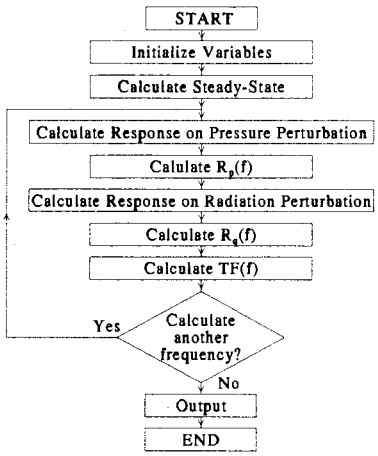

Figure 6.3: Flow chart of the program.

Next the heat release by the gas phase, H_g, and the characteristic gas phase time parameter $< \tau_g' >$, are calculated.

For calculations where the phase transitions are taken into account, the transition points (given by j_{tra} and j_m) are determined from the estimated thermal profile. With these estimations the thermal profile is calculated. If the difference between the calculated and the estimated temperature profiles is larger than the prescribed tolerance, the estimated profile is adjusted by successive substitution. It was found that a direct substitution of the calculated profile does not yield convergence for all situations. Because of this the estimation profile, Θ_j^k, is only partially adjusted for each iteration step

$$\Theta_j^k = a\Theta_j^k + b\Theta_j^{n+1}(\Theta_j^k) \; . \tag{6.22}$$

For stability reasons this adjustment is small for steady state calculations (e.g. $a = 0.9$ and $b = 0.1$), and may be larger for transient calculations ($a = 0.5$ and $b = 0.5$).

Next it is verified whether the temperature at the transition points is correct. If not, the transition points are moved, and calculations with the adjusted points are performed again.

If all conditions are satisfied, the thermal profile in the condensed phase is known. For transient calculations these computations are repeated for a large number of points of the perturbing function (e.g. 50 calculations per cycle of the perturbation).

6.4 Steady-state burning.

Most time-dependent burning calculations start from the steady-state situation, which is then disturbed e.g. by changing pressure, or external radiation (for ignition transients the initial temperature profile is constant, and equal to the ambient temperature). So, it is necessary to calculate the steady-state temperature profile. This section shows some typical

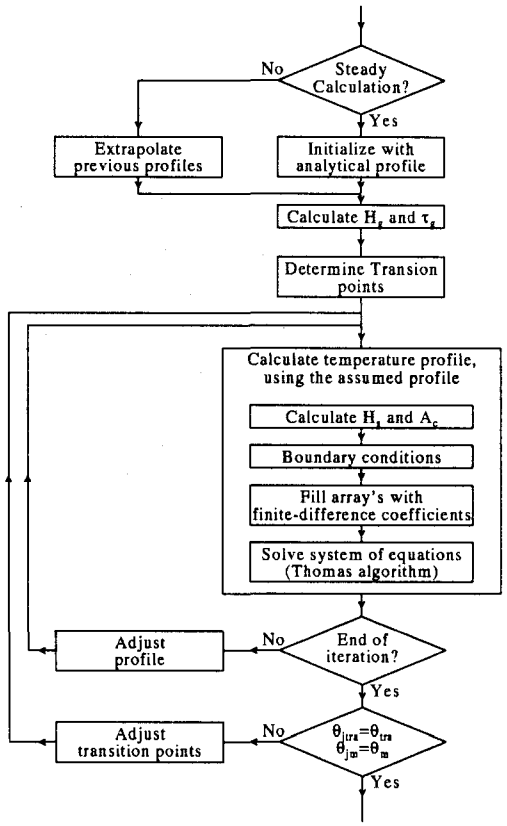

Figure 6.4: Flow chart of the calculation of the thermal profile in the condensed phase.

temperature distributions calculated for the dataset of appendix D. Unless noted otherwise, all calculations were performed at a pressure of 1 MPa, and with temperature dependent thermal properties in the condensed phase. The nonlinear heat-feedback from the gas phase was modeled with a characteristic time dependent on pressure only ($\tau_g = f(p)$), and with $\alpha = 0$, $\beta = 1$, and $\gamma = 0$, i.e. a nonlinear KTSS flame.

The empirical burning rate equation, $r_b = ap^n$, can only be used for steady state calculations. For the transient calculations the Arrhenius pyrolysis law of equation (3.11) is used. Of course this pyrolysis law should have the steady state burning law as a limit for steady burning. In figure 6.5 the steady-state burning rate equation and the Arrhenius equation as used for the transient calculations are plotted. From this figure it can be concluded that the Arrhenius law describes the burning rate accurately in the pressure range of interest.

First the influence of thermal properties is examined. As described in chapter 5, thermal properties may not be regarded as constant over the temperature range in solid propellants. Figure 6.6 shows two steady-state profiles in the condensed phase, one is the analytical

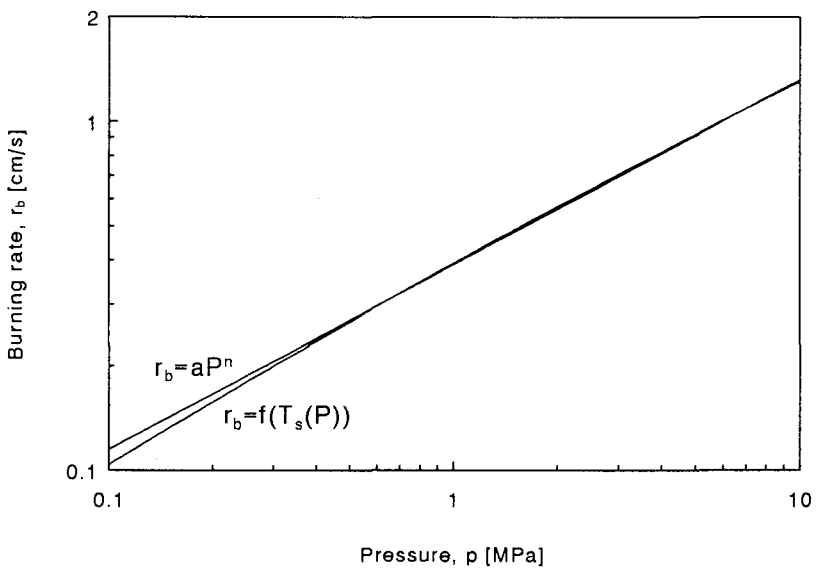

Figure 6.5: Comparison of the steady-state equation $r_b = ap^n$ and the Arrhenius pyrolysis law.

solution for a nonreacting solid with constant thermal properties (see equation A.14), the other one is calculated with variable thermal properties (latent heat of phase change neglected), see appendix D for details. From this figure it can be seen that for accurate calculations it is not allowed to consider the thermal properties as being constant. It should be noted that the discontinuities in the thermal properties have been removed by connecting the different regimes between transitions in the thermal conductivity by straight lines between the points 20 K before and after the transitions, see figure 6.7. The reason for this is twofold; for the numerical calculations the convergence is better, and because of the inhomogeneous structure of AP-composites the measured temperature profiles are not sharp, but rounded at the transition points. By introducing the small connection lines, the calculated temperature profile in the solid becomes smoother, because no more discontinuities in the properties exist.

As described in the previous chapter, the crystallographic transition, and the melting of AP require energy. Due to these heat sinks the temperature profile will change. Figure 6.8 shows the effect of the latent heats Q_{tra}, and Q_m. These are calculated as $Q_{tra} = f_{AP}Q_{tra,AP}$, and $Q_m = f_{AP}Q_{m,AP}$ where f_{AP} the weight fraction AP in the propellant, $Q_{tra,AP}$ the latent heat of crystal transition for pure AP, and $Q_{m,AP}$ the melting heat for pure AP. The value of $Q_{m,AP}$ is not found in open literature, so the melting heat of potassium perchlorate was used in the calculations, as suggested by Guirao [28]. As expected, the profile which accounts for the latent heats lies below the profile where these heats have been neglected.

To validate the calculations, measurements of temperature profiles in the condensed phase were sought for, however very few accurate measurements of profiles in the condensed

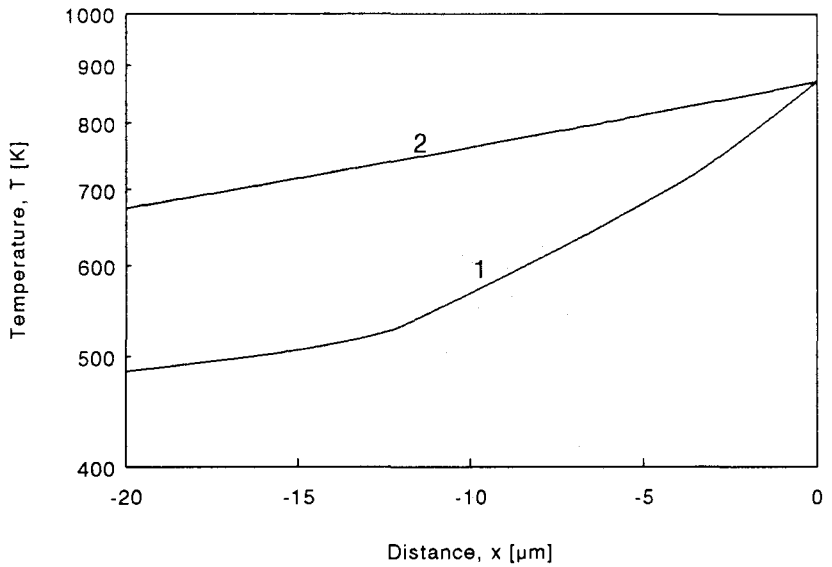

Figure 6.6: Steady-state thermal profiles in the condensed phase. Profile 1 is obtained by calculations with variable thermal properties, and profile 2 is the analytical solution of the energy equation.

phase exist. Figure 6.9 compares the results of measurements from a recent work [57] with the thermal profile obtained by numerical calculations, at a pressure of 1.5 MPa. The thermophysical properties used in the calculations, were derived from these experimental steady-state temperature profiles. For the derivation of these properties, it is necessary to assume that $Q_m = Q_{tra} = 0$. So, to obtain the same results as in the experiments the latent heats have been set to zero in the calculations. It is further seen that the measured profile only shows a bend at the crystal transition point, and not at the melting point. To reproduce these results the thermal conductivity had to be adjusted, so that the thermal conductivity was continues at the melting point of AP.

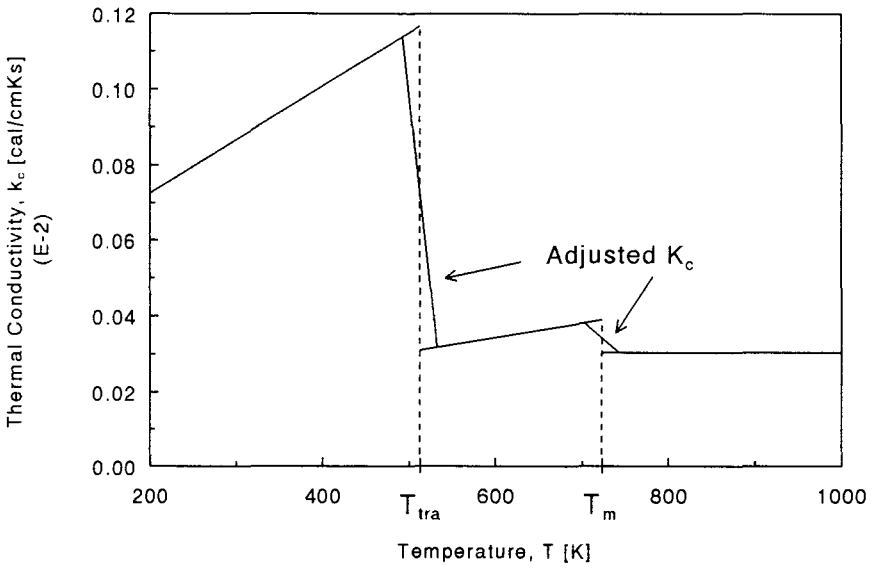

Figure 6.7: Removal of the discontinuties of the thermal conductivity.

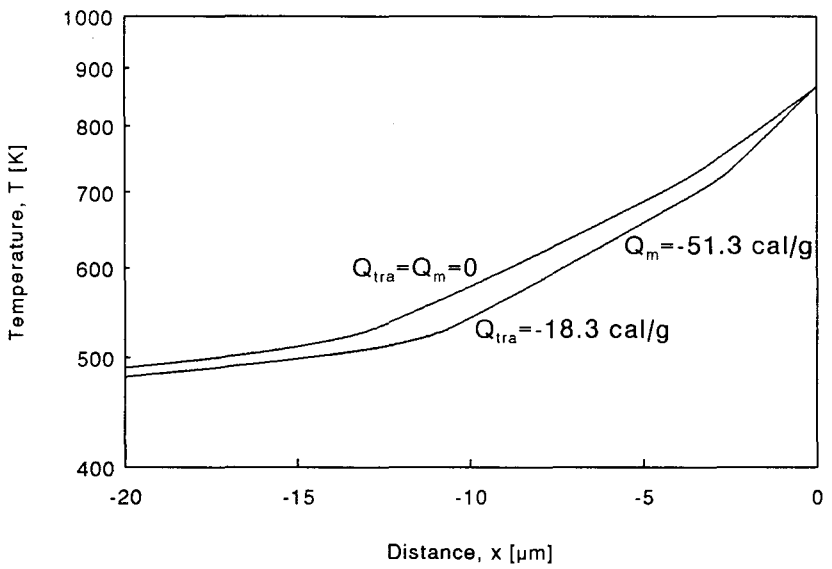

Figure 6.8: Effect of the latent heat of crystal transition and melting of AP on the steady-state thermal profiles in the condensed phase.

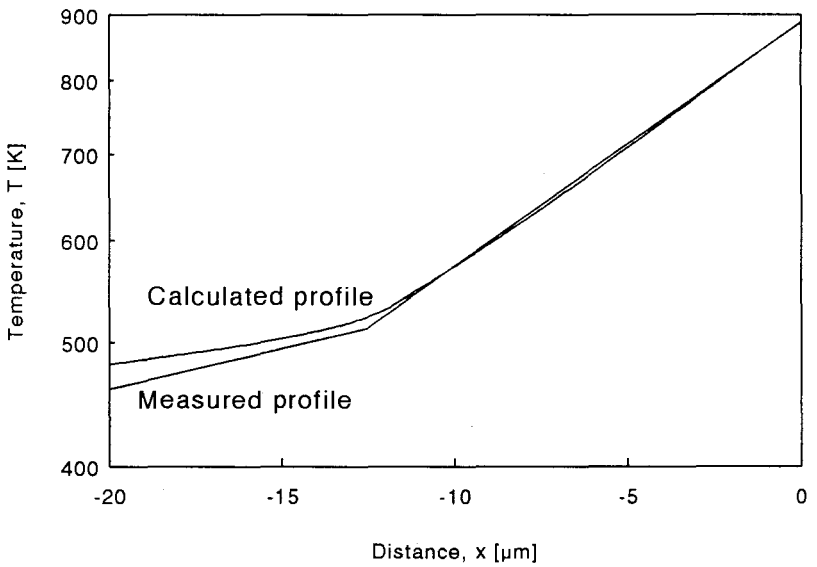

Figure 6.9: Comparison of calculated and measured thermal profile at 1.5 MPa. In the calculation the latent heat of crystallographic transition, and melting have been set to zero.

6.5 Time-dependent burning.

In order to examine the effects of the propellant parameters on the transient combustion, several numerical experiments were performed. This section describes the results of these experiments, and summarizes the sensitivity of the combustion transients to some of the propellant parameters.

6.5.1 Introduction.

To explain the transient combustion of a solid rocket propellant, an illustrative example will be discussed first. Figure 6.10 shows the response of a solid rocket propellant to a sinusoidal pressure disturbance. At $\tau = 0$ the propellant is in its steady state. Because of the inertia of the propellant, the disturbance has a phase lead to the response. At several positions in time, the temperature profile was monitored.

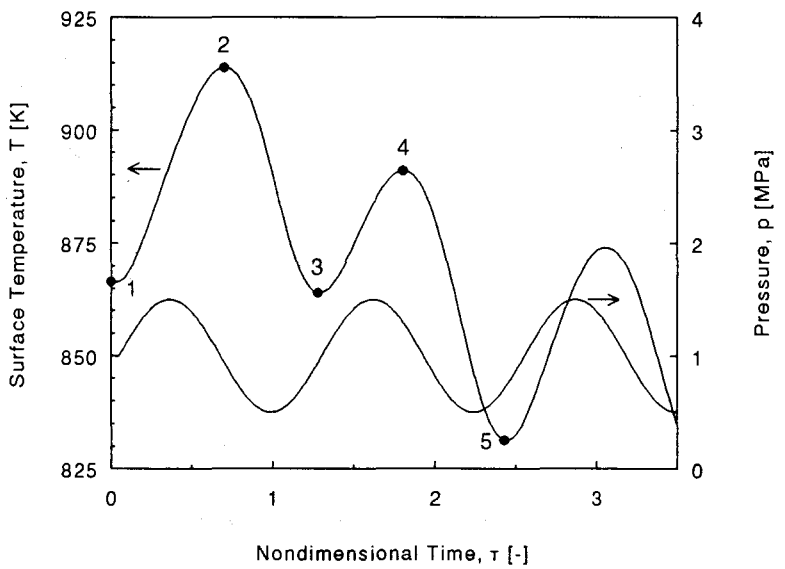

Figure 6.10: Combustion transient during a sinusoidal pressure disturbance.

Figure 6.11 shows the temperature profiles of the several situations of figure 6.10. It is seen that the temperature profiles continuously change during nonsteady combustion. It is also seen that the combustion is not only determined by the temperature profile at that time, but also by the previous profiles. The profiles 1 and 3 e.g. are almost equal, but the envelope of the surface temperature is different.

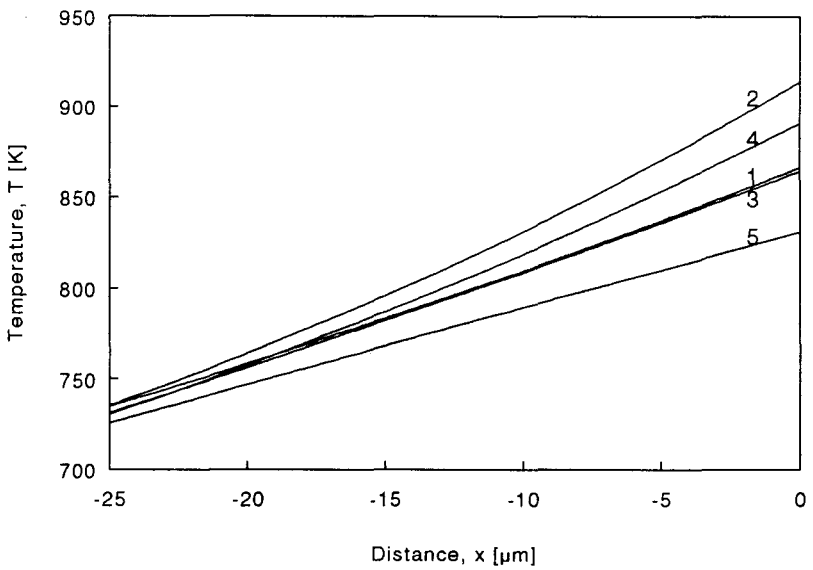

Figure 6.11: Temperature profiles in the condensed phase during transient burning.

6.5.2 Combustion transients.

First the effect of pressurization is verified. These calculations start from a steady state situation followed by a raise in pressure according to

$$P(t) = \begin{cases} \bar{P} & \text{if } \tau < 0 \\ \bar{P} + \Delta P(1 - e^{-\tau}) & \text{if } \tau > 0 \,. \end{cases} \tag{6.23}$$

For the standard dataset as described in appendix D, the pressurization transients can be followed easily without any transients. However, the propellants response is very sensitive to the value of the surface heat release, Q_s [6] [39], and literature shows great scatter of its value. From thermocouple measurements Sabadell et al. found $Q_s = 130$ cal/g (544 J/g) for a AP/PBAA-propellant [47]. Finlinson et al. reported a value of $Q_s = 160$ cal/g (669 J/g) for a trimodal AP/HTPB-propellant [24]. When this value is used in the calculations the propellants response is much larger as shown in figure 6.12. Calculations for a step function for the pressure increase show the same response. It was tried to find nonlinear instability as shown in figure 2.1, but this type of instability was not found, all calculations showed a damped response, identical to that of figure 6.12.

The condensed phase heat release is exponentially distributed below the burning surface according to equation 5.3. The surface heat release can be seen as a limiting case for the condensed phase heat release, when all the heat is released in an infinitesimally thin layer below the surface. Also shown in figure 6.12 is the combustion transient for $Q_s = 0$ and $Q_c = 160$, i.e. all exothermic heat release located in the solid phase. From this figure it becomes clear that surface heat release and condensed phase heat release have a very similar effect on the (in)stability of a solid propellant in this model.

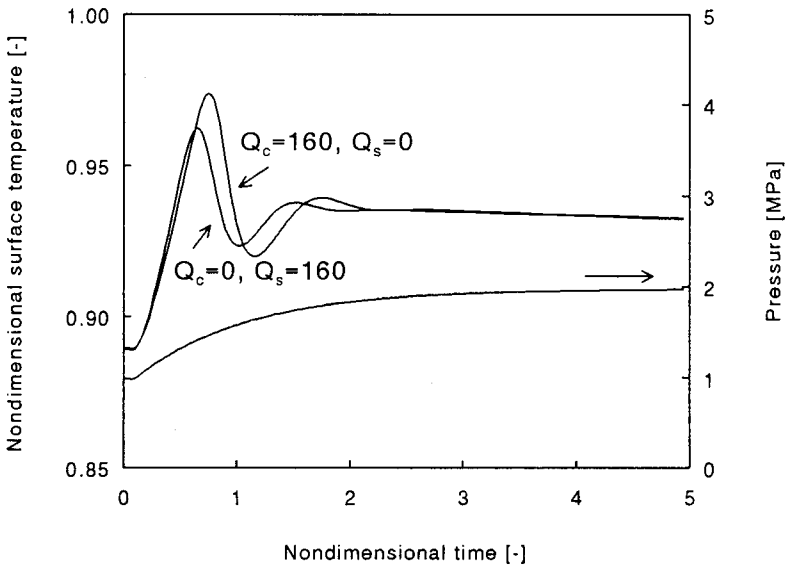

Figure 6.12: Combustion transient during a pressurization from 1 to 2 MPa. It can be seen that the effect of the surface and condensed phase heat release, Q_s and Q_c is identical.

An analogous calculation can be performed for a radiation perturbation. Figure 6.13 shows the result of an increase of external radiation from 50 cal/cm^{2}s to 75 cal/cm^{2}s (209 to 314 W/cm^2). For the calculations two extreme values of the absorption coefficient were used. The minimum absorption has a characteristic layer thickness of 100 μm (a_λ = 100 cm^{-1}), while a maximum absorption has a layer of 5 μm (a_λ = 2000 cm^{-1}). It is shown that a high absorption coefficient yields a fast response. This is easily understood, because for a low absorption the radiant energy is absorbed far in the solid, for high absorption however, all radiant energy is absorbed near the burning surface, leading to a large increase of temperature below the surface. The ultimate response however is the same. As will become clear later, this figure is an example of self-sustained oscillatory combustion, see section 7.1.2.

Until the recent advance of powerful computers, most instability calculations were performed with the linearized equations as discussed in chapter 4. Within these calculations the disturbance amplitude is assumed to be small as compared to the steady state value. However, during real combustion large fluctuations may occur, e.g. by nozzle blockage or resonance in the rocket motor cavity. Due to the nonlinearity of the equations the response of the propellant is dependent on the disturbance amplitude. Measurements show that propellants may be stable for small disturbances, but unstable for large perturbations. Figure 6.14 shows the effect of the perturbation amplitude on the propellants response, in analogy with equation (2.1) defined as

$$\text{Response} = \frac{\Delta\Theta_s/\bar{\Theta}_s}{\Delta P/\bar{P}} \,. \tag{6.24}$$

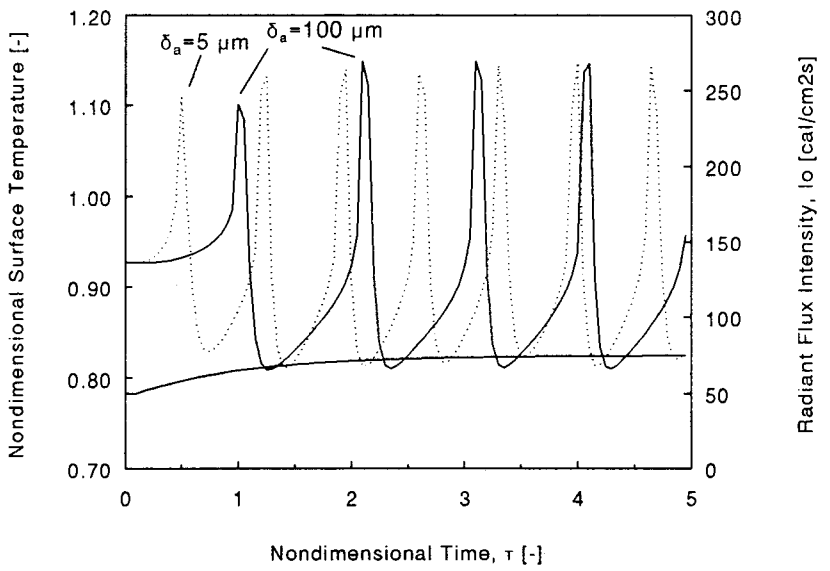

Figure 6.13: Effect of increase of external radiant flux on the surface temperature, for two extreme values of condensed phase absorption.

This figure is obtained by disturbing the steady state situation with a sinusoidal pressure having a frequency of 500 Hz, and an amplitude of 10% and 50% of its steady state value of 1.0 MPa. For small perturbations the response is approximately sinusoidal, i.e. linear with its source. For large amplitudes however, the response is no longer linear, and large fluctuations may occur.

To further analyze the effect of the nonlinearity for large amplitudes, power spectrum analysis of the combustion transients have been performed. For the calculation of the discrete Fourier transforms the Fast Fourier Transformation (FFT) subroutine of the Turbo Pascal Numerical Toolbox software package is used. This routine calculates the FFT of dataseries with 2^i (i and nonnegative integer).

Because of this limitation it is necessary to truncate the waveform to be analyzed after these 2^i points. In general this truncation does not take place at a multiple of the period of the propellants response. Because of this, sharp discontinuities are introduced, which results in additional frequency components in the frequency domain [5]. This effect is called *leakage*, and is inherent in the Discrete Fourier Transform (DFT) because of the required time domain truncation.

To reduce leakage, a truncation function $x(t)$ can be used, i.e. in stead of calculating the DFT of $f(t)$, the DFT of $x(t)f(t)$ is calculated. A good truncation function is the Hanning function given by $x(t) = \frac{1}{2} - \frac{1}{2}\cos(2\pi t/T_c)$, for $0 \leq t \leq T_c$, where T_c he length of the truncation interval. The utilization of this function will reduce leakage significantly [5].

To clearly illustrate the effect of the disturbance amplitude on the response of the propellant a large surface heat release ($Q_s = 150$ cal/g, 628 J/g) is used for the calculations.

Figure 6.15 shows the effect of the disturbance amplitude on the power spectrum of

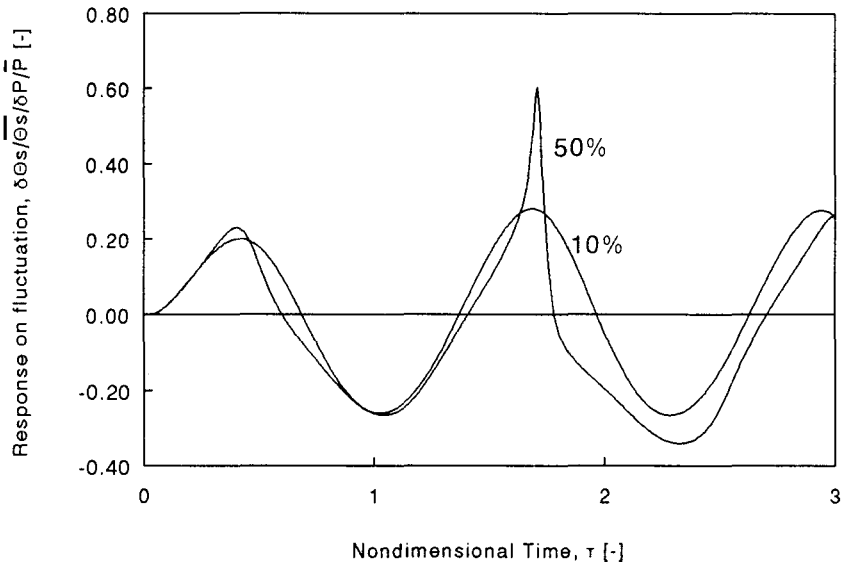

Figure 6.14: Response of the propellant on a sinusoidal pressure perturbation, with an amplitude of 10% and 50% of its steady state value of 1.0 MPa.

the response, for a signal of 1024 datapoints ($i = 10$). For small amplitudes the response contains only one frequency, the driving frequency f_0 of the pressure disturbance. For large disturbances the response of the system becomes nonlinear, and other frequencies are introduced. It is interesting to note that these frequencies are higher harmonics of the perturbing frequency f_0. From the figure is becomes clear that for the usual limit of 10% disturbance the system responds almost linearly, and it is justified to consider it as linear.

It has been reported that it is possible to calculate the response of the system for different frequencies with one measurement with a pulsating disturbance [52]. However, this is only allowed when the perturbation is so small that the response is linear. This it opposite to the desired large amplitude disturbances for a good signal to noise ratio in experiments.

The response of the system to a rectangular pulse of 500 Hz, with an amplitude of 10% is shown in figure 6.16. The FFT of these two signals are shown in figure 6.17. The FFT curves have been normalized by their value at the disturbance frequency f_0. It is seen that the response exhibits a response with a frequency $\frac{3}{2}f_0$, i.e. a noninteger multiple of the base frequency, which is not a frequency of the disturbing signal. So when pulsating experiments are carried out, the disturbance amplitude has to be vary small, in order to stay in the linear regime.

In this section several examples of transient burning were discussed. It was shown that the nonlinearity plays an important role when the perturbing amplitudes are large. Especially the surface heat release, Q_s, and condensed phase heat release, Q_c, are important parameters. In the next section these calculations will be extended to the calculation of response functions.

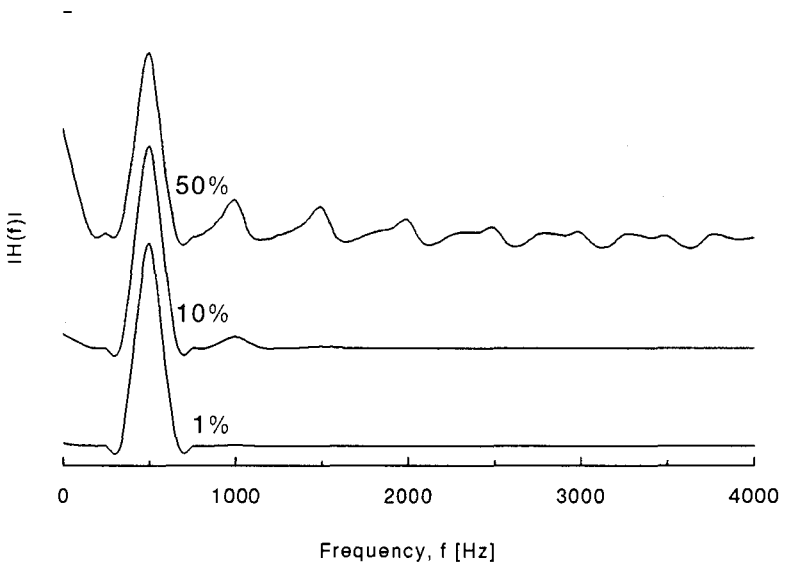

Figure 6.15: Effect of the disturbance amplitude on the fft-spectrum.

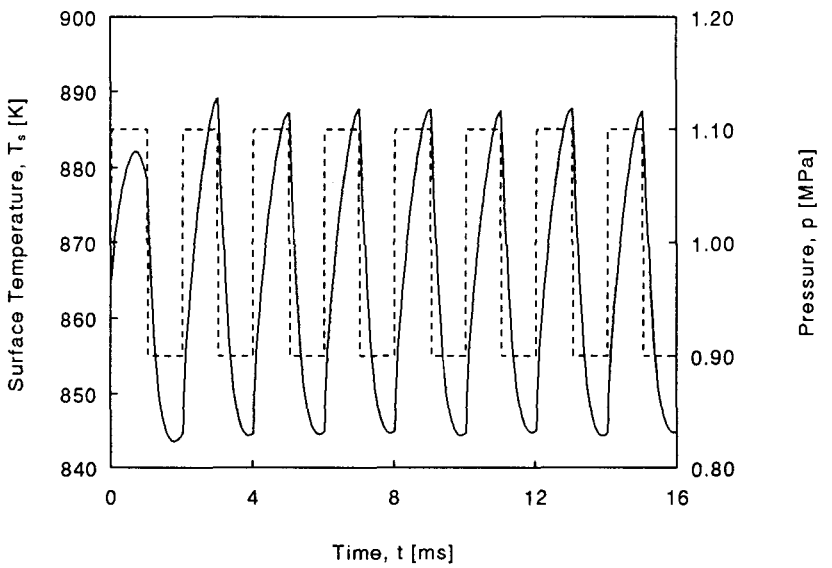

Figure 6.16: Pulsating perturbation and the response of the propellant.

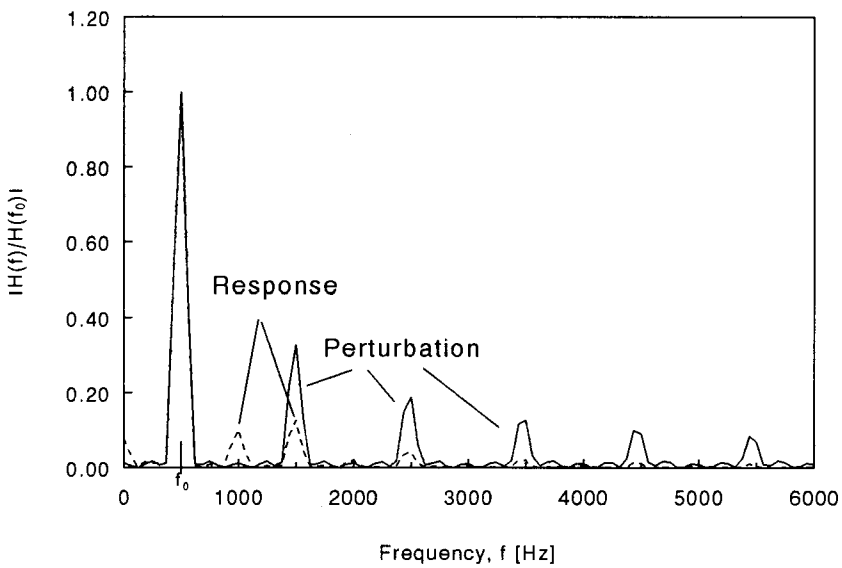

Figure 6.17: FFT spectrum of the pulsating perturbation and the response of the propellant.

6.5.3 Pressure driven frequency response functions.

When the steady-state burning is perturbed with sinusoidal pressure and radiant flux disturbances of different frequencies, the response functions of the propellant can be calculated. As seen from figure 6.14, the response from the propellant is nonlinear, and is dependent on the previous history.

A large number of responses have been calculated, and it was found that for frequencies below the resonance frequency the response becomes periodically[1] after a few cycles (usually two or three). This is in agreement with the findings of DeLuca et al. [20]. For frequencies above the resonance frequency however, it was found that more cycles had to be calculated in order to achieve a periodical situation. For high frequencies the distance burned during one disturbance cycle is smaller than the thermal layer thickness, hence it takes more cycles to burn through the disturbed zone and to achieve the dynamic equilibrium situation. Figure 6.18 shows a typical surface temperature history, during a sinusoidal pressure disturbance.

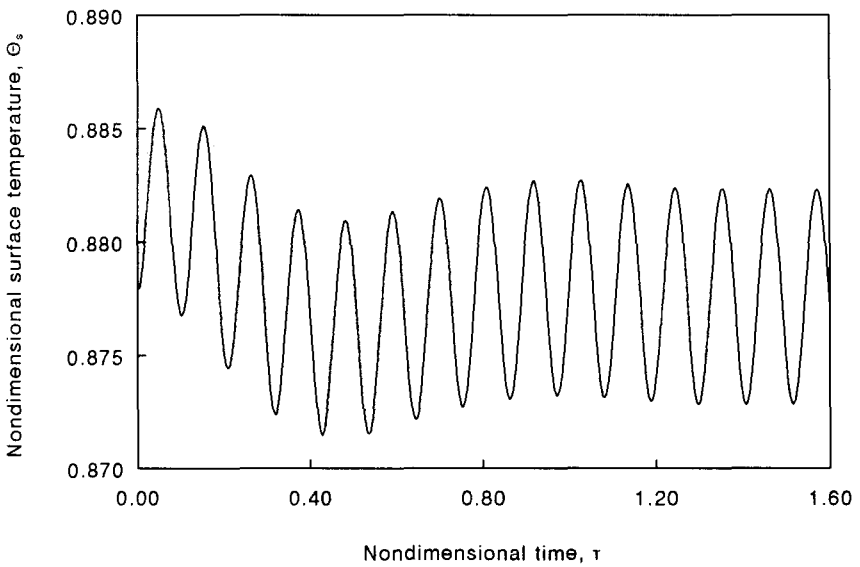

Figure 6.18: Fluctuating surface temperature due to a sinusoidal pressure disturbance. After a few initial cycles the surface temperature responds periodically.

It was found generally valid that the response becomes periodical after approximately 10 to 15 cycles. Because of the wider thermal layer for calculations with condensed phase reactions, these type of calculations take more cycles to obtain this situation.

The response function for a given frequency is defined as the maximum relative change in burning rate occurring in the the disturbance in the situation of dynamic equilibrium.

To validate the numerical calculations in the limit of small perturbations, a comparison has to be made with the linear analysis. Figure 6.19 shows the results of this calculation.

[1] Periodical in the sense of $f(\tau) = f(\tau + p)$, where p is period.

The calculations in this figure were performed with constant thermal properties, a surface heat release of 125 cal/g (523 J/g), and a sinusoidal pressure change, with an amplitude of 10% of its mean value. Unless noted otherwise all calculations in this section are performed with this type of disturbance. As seen from the figure the calculations correspond, but still show some deviation from the linear profile.

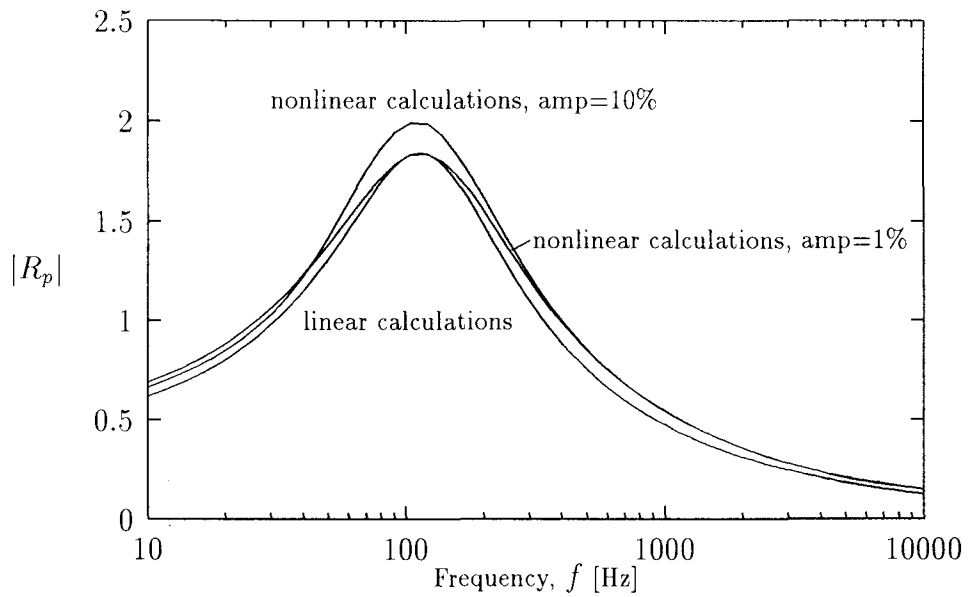

Figure 6.19: Nonlinear pressure driven response function versus linear calculated response function (constant thermal properties).

Because of this deviation, a second calculation was performed, with an amplitude of 1% of its mean value, see figure 6.19. This response function still shows a small deviation from the linear response function, but now the maxima correspond.

Two explanations have been found for the remaining difference between linear and nonlinear calculations. First there is the heat feedback from the gas phase and the pyrolysis law. For the nonlinear calculations a nonlinear KTSS-flame is used, while the linear response function is calculated for a linear KTSS-flame. A further difference is the pyrolysis law. For the nonlinear calculations an Arrhenius type of pyrolysis law was assumed (equation (3.11)), while the linear calculations are based on the power law by Krier (equation (3.12)).

Most measurements of pressure-coupled response functions are carried out under low pressures. The reason for this is the that high pressure measurements can only be performed with expensive equipment. However, typical pressures in solid rocket motors vary from 4 to 15 MPa, and cannot be compared with the conditions under which the experiments are carried out.

Figure 6.20 shows the effect of the pressure on the response functions. The resonance peaks decrease in magnitude for increasing pressure, and shift towards higher frequencies. So, when the propellant is burning at a higher pressure, it becomes more stable. This

phenomenon can be explained as follows. At low pressures the burning rate is small, yielding a broad thermal layer ($d \sim \frac{\alpha_c}{r_b}$). When the pressure is increased the burning rate increases, resulting in a thin thermal layer. The thermal layer can be seen as a "memory" in which the previous combustion processes are stored. Broad thermal layers have a large memory, and respond fiercely on the disturbance. Thin thermal layers burn away fast, so the memory is short. Note that the analogy with a memory is not complete, for high frequencies there is a phase lead of the burning rate on the applied disturbance, for an extensive discussion see Finlinson et al. [24]. The maxima shift to higher frequencies, because the thermal layer is smaller for higher frequencies. Smaller thermal layers have a higher resonance frequency.

It is necessary to make a comment on these calculations. It was discussed in chapter 3 that the quasi-steady assumption of the gaseous phase is only valid for low frequencies and at low combustion pressures. Thus the high pressure calculations have to be interpreted carefully, because they may violate both conditions. The condensed phase characteristic time t_c^* at 10 MPa is calculated as

$$t_c^* = \frac{\bar{\alpha}_c}{r_b^2} = \frac{\alpha_c(300\ K) + \alpha_c(1000\ K)}{r_b^2} = 6.9 \cdot 10^{-4}\text{s}\ , \tag{6.25}$$

where the mean value of the thermal diffusitivity in the thermal layer, $\bar{\alpha}_c$, is approximated by the mean of it's value at the cold boundary and at the burning surface. The gas phase characteristic time t_g^* is calculated as

$$t_g^* = \frac{\alpha_g}{u_g^2} = \frac{\alpha_g}{\left(\bar{r}_b \frac{\rho_c}{\rho_g}\right)^2}\ , \tag{6.26}$$

where the last equality is obtained from a mass balance across the burning surface. The density of the gas phase, ρ_g, is calculated from the ideal gas equation

$$p = \frac{\rho_g \Re T_f}{M}\ , \tag{6.27}$$

where M the average molecular mass of the gas products. With the NASA SP-273 code [26] it is found that $M = 25$ at 10 MPa. Finally it is found that $t_g^* = 1.4 \cdot 10^{-6}$s. The resonance peak at 10 MPa occurs at an external disturbance frequency of approximately 4000 Hz, i.e. $t_{ext}^* = 2.5 \cdot 10^{-4}$s. So, for the calculations at 10 MPa it is found that $t_{ext}^* \sim t_g^* \gg t_c^*$. So the quasi-steady theory is applicable at 10 MPa.

The relations between the several curves of figure 6.20 can be made clear by plotting them as a function of the nondimensional circular frequency Ω, as shown in figure 6.21. Because this frequency incorporates the steady-state burning rate (see equation (4.4)), the x-axis scaling factor is different for each pressure. It is seen that Ω is a good nondimensional quantity, shifting all maxima to the same frequency, even for these nonlinear calculations.

The same calculations have also been performed for constant thermal properties. Figure 6.22 and 6.23 show the result of these calculations. Several conclusions can be drawn

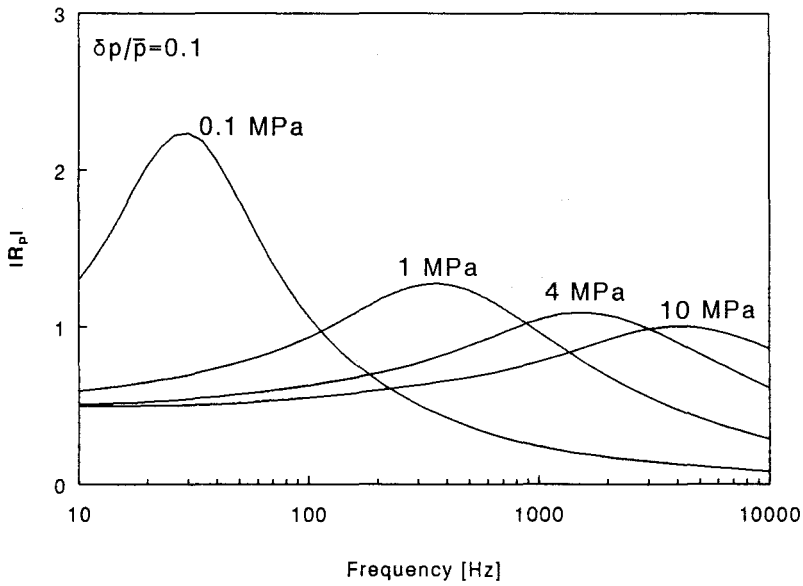

Figure 6.20: Effect of the value of the steady-state pressure on the pressure coupled response function, for temperature dependent thermophysical properties.

from the comparison of the figures 6.21 and 6.23. The location of the maxima does not coincide. This is easily explained. The nondimensional frequency Ω is based on the thermal diffusivity at reference conditions, $\alpha_{c,ref}$, i.e. at temperature 300 K. For temperature dependent thermophysical properties this value does not describe the actual diffusivity in the thermal layer, hence the calculations are based on a different α_c as they are scaled with.

The effect of the temperature dependent thermal properties is obvious. The response functions are shifted towards higher frequencies, as seen from figure 6.24. Resonance will occur when the characteristic time of the external disturbance t^*_{ext} is of the same order as the characteristic time of the condensed phase t^*_c. t^*_c is dependent on the thermal diffusivity, so the location of the maximum is determined by the value of the thermophysical properties. Because the temperature dependence of the thermal properties yields steeper temperature profiles in the solid (see figure 6.6), the affected zone in smaller, and hence the "storage capability" is less. So, it is expected that response function for a calculation with temperature dependent properties has a smaller maximum. This expectation is confirmed by figure 6.24.

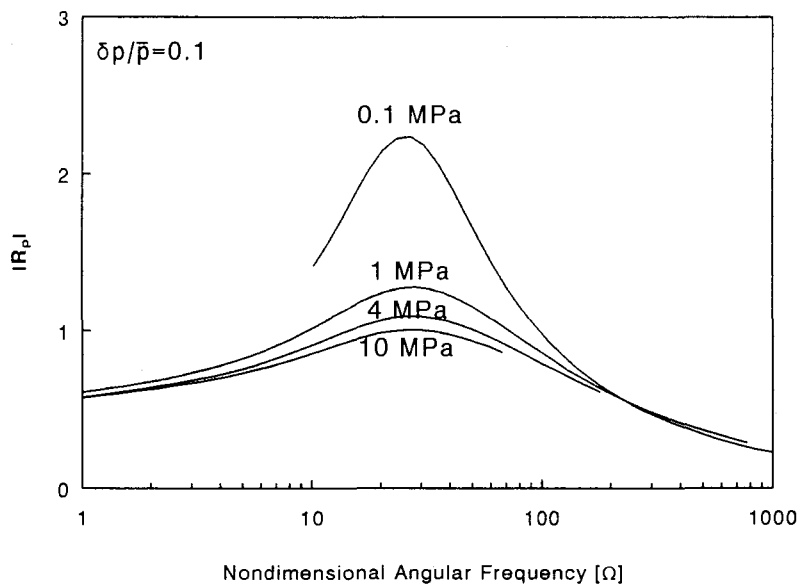

Figure 6.21: Effect of the value of the steady-state pressure on the pressure coupled response function, for temperature dependent thermophysical properties.

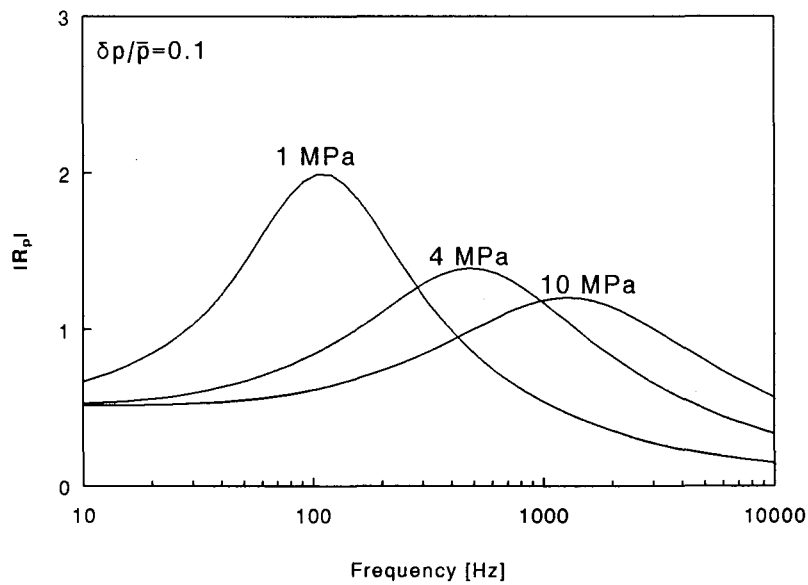

Figure 6.22: Effect of the value of the steady-state pressure on the pressure coupled response function, for constant thermophysical properties.

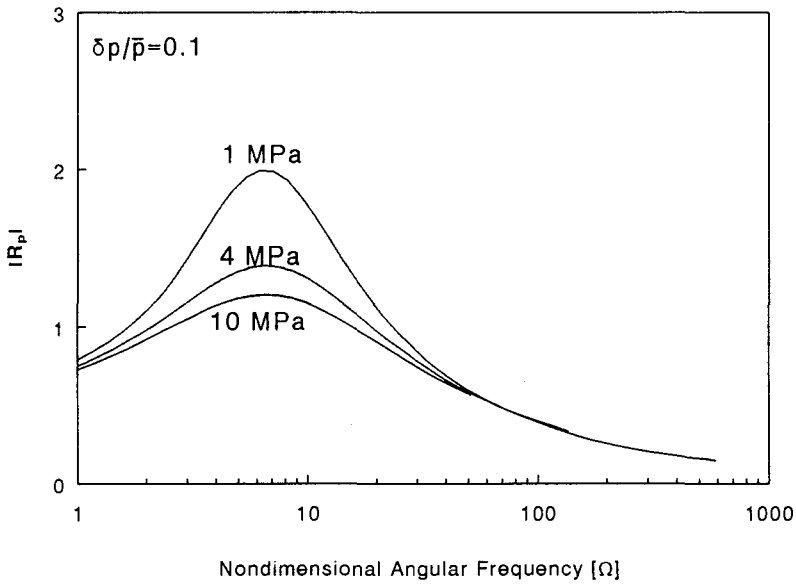

Figure 6.23: Effect of the value of the steady-state pressure on the pressure coupled response function, for constant thermophysical properties.

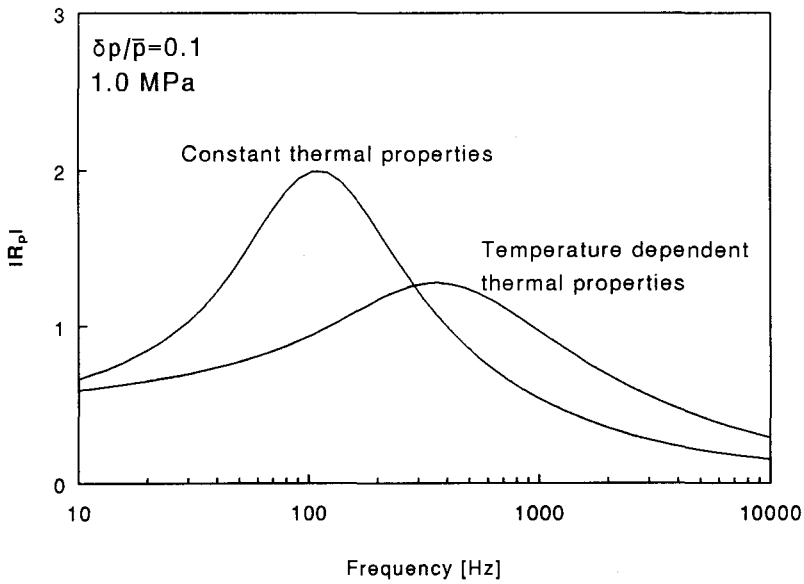

Figure 6.24: Effect of the thermal properties on the pressure coupled response function.

6.5.4 Radiation driven frequency response functions.

An important issue in contemporary rocket research is to determine the relation between radiation driven and pressure driven response functions. The ultimate goal is to measure the radiation driven response function and to calculate the pressure coupled response function from this data, via the theoretical transfer function. To determine this transfer function theoretically both response functions have to be calculated. The radiation driven response function is calculated in a similar way as the pressure driven response function, by disturbing the steady-state with a disturbance amplitude of 10% of it's steady-state value.

The volumetric absorption coefficient, $\bar{\bar{a}}_\lambda$, is an important parameter which should be known accurately to calculate the propellants response on the external fluctuating radiant source. Pure AP has a high absorption coefficient, $\bar{\bar{a}}_\lambda = 2000$ cm^{-1}, but measurements show much lower values of $\bar{\bar{a}}_\lambda$ for composite propellants. This discrepancy may be explained by scattering at the AP crystals and the transparency of the binder. Finlinson et al. [24] used $\bar{\bar{a}}_\lambda = 4000$ cm^{-1}, for a trimodal AP-propellant, containing 0.1% carbon black. These values are about an order of magnitude larger than the measured values. The reason for calculating with this unusual high value of the absorption coefficient were the experimental results. According to Finlinson et al. the high absorption can be contributed to the formation of a melt layer on the surface, or the crystalline phase change of AP, which could result in a surface with very different optical properties.

Figure 6.25 shows the response of the reference propellant for different values of $\bar{\bar{a}}_\lambda$ for a mean radiant heat flux of 50 cal/cm^{2}s (209 W/cm^2). As seen from this figure, the shape of the curve varies for different values of the absorption coefficient, changing from a monotonous decreasing function ($\bar{\bar{a}}_\lambda = 100, 500$ cm^{-1}), to a function with a maximum ($\bar{\bar{a}}_\lambda = 1000, 2000, 5000$ cm^{-1}). Not only the value of the maximum is affected by the absorption coefficient, but also the location of this maximum. These effects are comparable with the effects found for linearized calculations [14]. The static limit (equation (2.7) can be determined from this figure, yielding $n_q \simeq 0.25$. Measured values of n_q for AP-composites show large scatter. Finlinson et al. measured $n_q = 0.012$ and $n_q = 0.20$ [24]. Strand et al. reported $n_q = 0.42$ at a nominal pressure of 2.1 MPa, and a mean heat flux of 20 cal/cm^{2}s (84 W/cm^2) [54]. Recently a value of $n_q = 0.29$ was published by Son and Brewster [52], for a mean radiant power of 41 W/cm^2 (10 cal/cm^{2}s). So, the calculated value of n_q agrees with measured values, within experimental uncertainties.

Son and Brewster reported about the experimental dependence of the response function on the mean value of the radiant energy flux [52]. To verify this, a second series of calculations was performed for a energy which is twice as large as used for the previous calculations. The perturbing part was kept 10% of it's steady state value. Figure 6.26 shows the result of these calculations.

Two conclusions can be drawn from the comparison of these two calculations. First, the maxima of the response functions become larger, and are shifted towards a higher frequency. Second, the static limit, n_q, is different for both situations. This can be explained easily. Pressure response functions have a static limit $n_p = n$, because of the steady-state burning

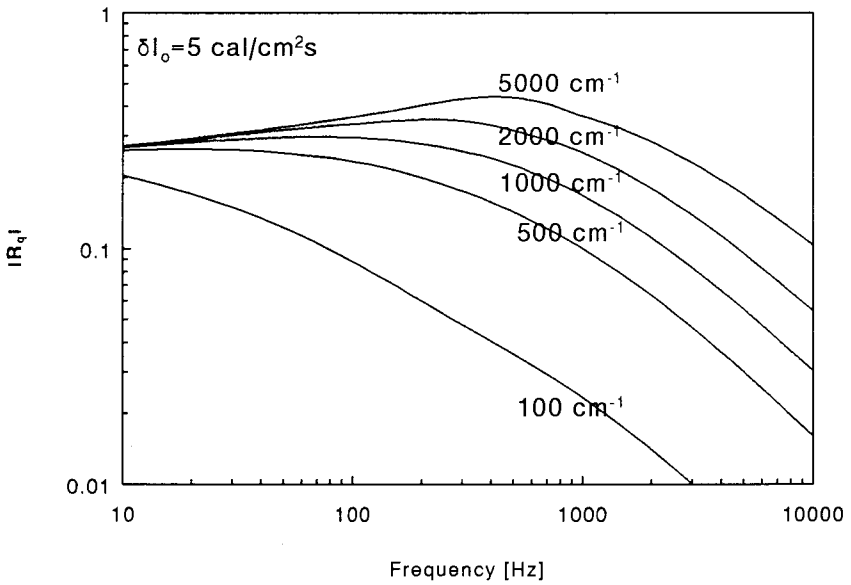

Figure 6.25: Effect of volumetric absorption coefficient $\bar{\bar{a}}_\lambda$ on the radiation driven response function for the reference propellant, for a heat flux of 50 cal/cm^{2}s. Crystal transitions and condensed phase reactions have been neglected in these calculations.

law $r_b = ap^n$. The dependence of the steady-state burning rate on the radiant heat flux is not given by such a power law, but is generally a nonlinear relation $r_b = \zeta(I_0)$ [24] [51] [52]. Figure 6.27 shows the measurements of Finlinson et al. [24]. The radiant heat flux fluctuates around it's steady-state value, and around this value the steady-state burning law can locally be described by $r_b = bI_0^{n_q}$. In this way the relation $r_b = \zeta(I_0)$ can be considered built up from power functions. Of course these power functions have coefficients, b and n_q, which are dependent on the mean value of the radiant flux.

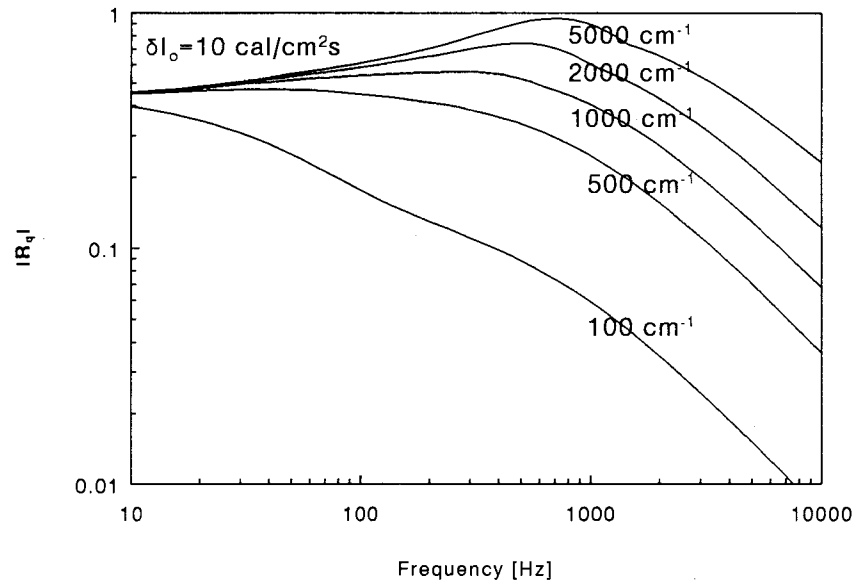

Figure 6.26: Effect of volumetric absorption coefficient $\bar{\bar{a}}_\lambda$ on the radiation driven response function for the reference propellant, for a heat flux of 100 cal/cm^{2}s. Crystal transitions and condensed phase reactions have been neglected in these calculations.

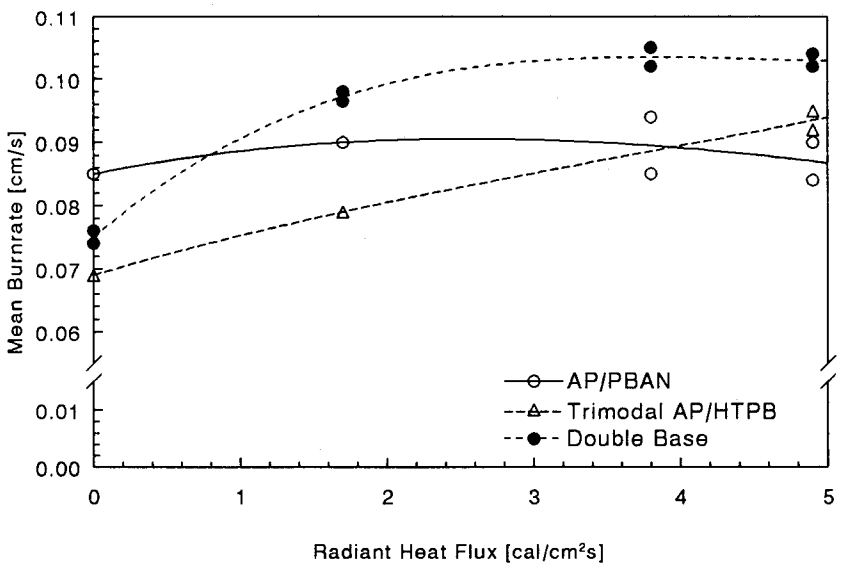

Figure 6.27: Experimentally determined steady-state burning rate as function of the applied external heat flux for three different propellants [24].

6.5.5 Condensed phase reactions.

Condensed phase reactions play an important role in the burning of both composite and DB propellants. To evaluate the effect of spatially different heat release rates, the effect of one typical group is further examined. It is assumed that the heat release can be modeled by

$$H_c\epsilon_c(X) = \begin{cases} 0 & \text{if } X < X_{tra} \\ A_c H_c (X - X_{tra})^n & \text{if } X_{tra} < X < 0 \end{cases} , \tag{6.28}$$

where n an integer, $n = 0, 1, 2, \ldots$. Figure 6.28 shows the effect of n on the heat release rate. This set of equations can be seen as an approximation of the processes taking place; the energy release in the condensed phase becomes larger near the burning surface. In the real situation the chemical reactivity is larger near the burning surface. An implicit temperature dependence is present, because X_{tra} is defined as $\Theta(X_{tra}) = \Theta_{tra}$, where Θ_{tra} the crystallographic transition temperature of ammonium perchlorate. Note that the situation for $n = 0$ is an exception, this describes a constant release of energy. In a recent publication of DeLuca et. al. [21] linearized calculations for a uniform distribution, i.e. $n = 0$, were performed.

The value of A_c can be found from the normalization condition

$$\int_{-\infty}^{0} H_c\epsilon_c(X)dX = H_c R \, . \tag{6.29}$$

The special form of equation (6.28) was selected such that this integration can be carried out easily

$$\int_{-\infty}^{0} H_c\epsilon_c(X)dX = \int_{X_{tra}}^{0} A_c H_c (X - X_{tra})^n dX \tag{6.30}$$

$$= \frac{(-1)^{n+1}}{n+1} A_c H_c (X_{tra})^{n+1} \, . \tag{6.31}$$

This yields

$$A_c = (-1)^{n+1} \frac{(n+1)R}{(X_{tra})^{n+1}} \, . \tag{6.32}$$

Figure 6.29 shows the effect of the parameter n on the steady state temperature profile, for a total condensed phase heat release $Q_c = 100$ cal/g (481 J/g) (note that the phase transitions are also accounted for in these calculations). For $n = 0$ a large part of this energy is released for away from the surface, which results in a higher temperature in the solid. For large n the heat release $H_c\epsilon_c(X)$ becomes very steep near the burning surface, yielding temperature profiles which are almost independent of n. Because the steady-state temperature profiles are different for each value of n, the transition point X_{tra} is also different for each n. This means that the chemical reaction zone width is determined by the value of n.

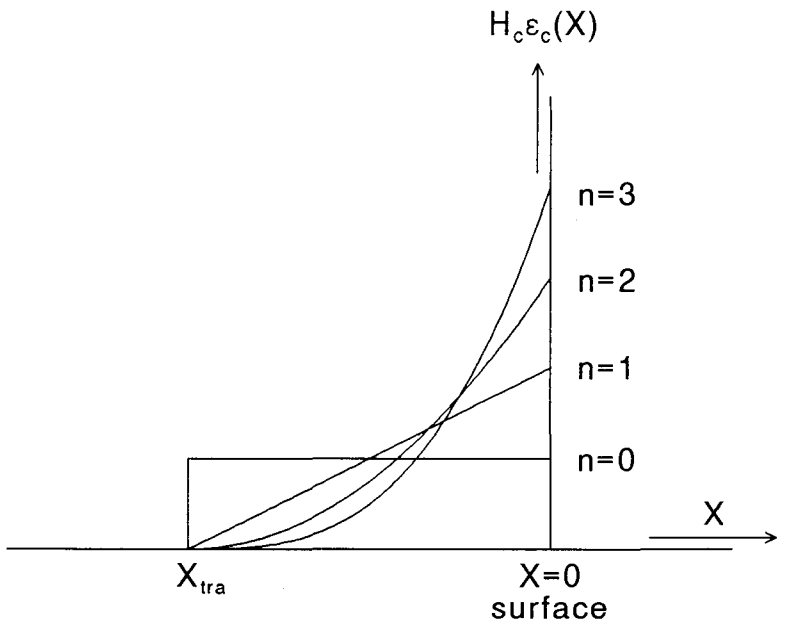

Figure 6.28: Heat release rates for different values of the parameter n.

Figure 6.30 shows the influence of the parameter n on the transient combustion of the propellant, for an sinusoidal disturbance, applied of 500 Hz. It is seen that, for this frequency, an increase of the value of the parameter n yields a larger response of the propellant, i.e. when more energy is released close to the surface, the response of the propellant becomes larger, hence it is shown that by collapsing the condensed phase energy to the surface ($n \rightarrow \infty$), the response function becomes larger for this frequency. Based on the linearized calculations mentioned before, DeLuca et. al. derived the same conclusions for an exothermic and endothermic heat release of 20 cal/g [21].

For a fixed frequency of 500 Hz, the response is larger for an increased heat release close to the surface. However, this does not mean that the response function is larger for *all* frequencies. To know the behavior of condensed phase reaction, the complete response function has to be calculated. Figure 6.31 shows the results of these calculations. By decreasing the reaction layer (increase of parameter n) the intrinsic stability increases, and the resonance peak shifts towards higher frequencies.

The chemical reactivity can also be modeled by a classical Arrhenius law as also discussed previously. Figure 6.32 shows the effect of the heat release distribution on the response function for three different cases. The first case is the common case $Q_s = 125$ cal/g, and $Q_c = 0$, i.e. all reactivity is assumed to take place on the surface. This result can be compared with the response function obtained from linearized analysis. The other two curves show the response function for a more realistic situation, $Q_s = 0$, and $Q_c = 125$ cal/g. Two activation energies have been used, a high activation energy 28.9 kcal/mole, as suggested by Kumar and Culick [35], and a low activation energy of 10 kcal/mole. The high activation energy resembles the situation of surface reactions, because for the high activation energy the chemical reactivity decreases very fast below the

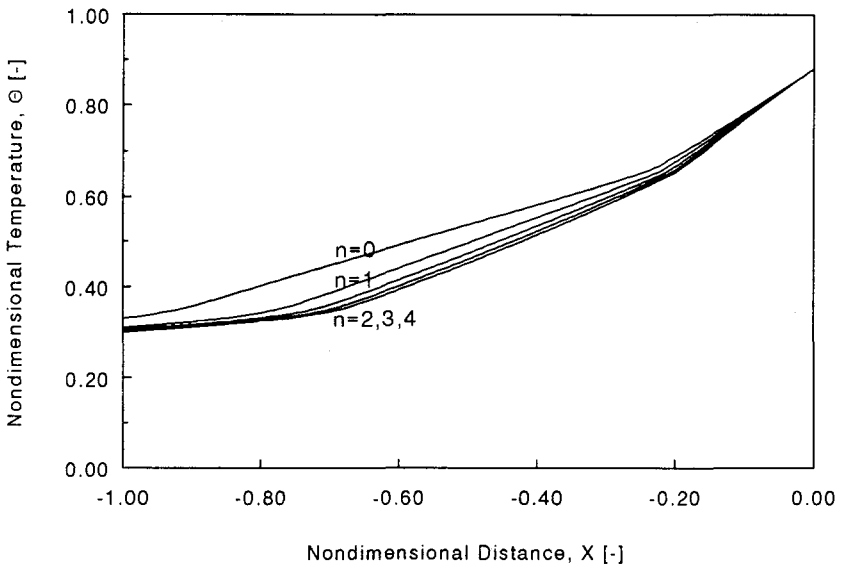

Figure 6.29: Steady state temperature profile for several values of the parameter n.

surface. It is seen that the condensed phase reactions lower the maximum response. So, when subsurface reactions are approximated by surface reactions, the propellant appears to be less stable. The maxima of the response function shift to lower frequencies, because the thermal layer is larger for subsurface reactions.

The results of the calculations with an Arrhenius-type reaction law and the above presented model are comparable. An increase of heat release near the surface decreases the stability (n larger or higher activation energy), and increases the resonance frequency.

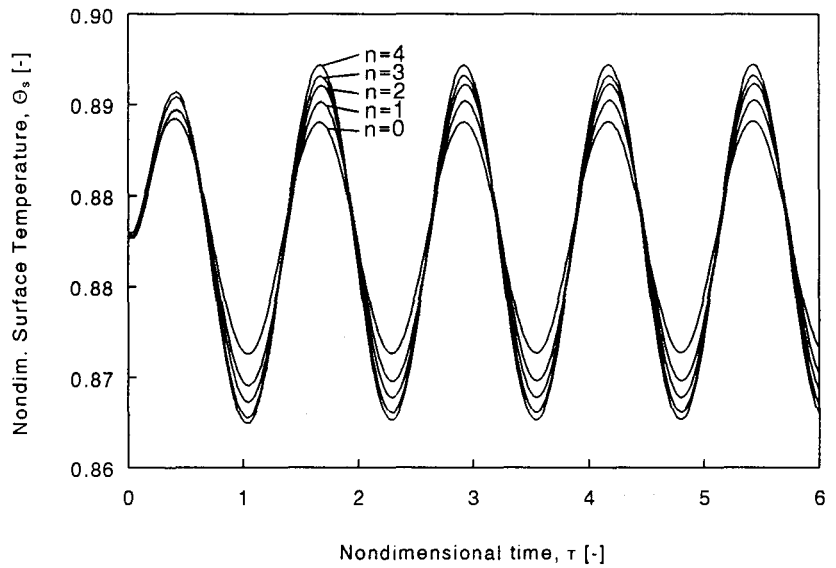

Figure 6.30: Transient burning due to a sinusoidal pressure disturbance for several values of the parameter n ($\bar{P} = 1.0$ MPa, $\Delta P/\bar{P} = 10$ %).

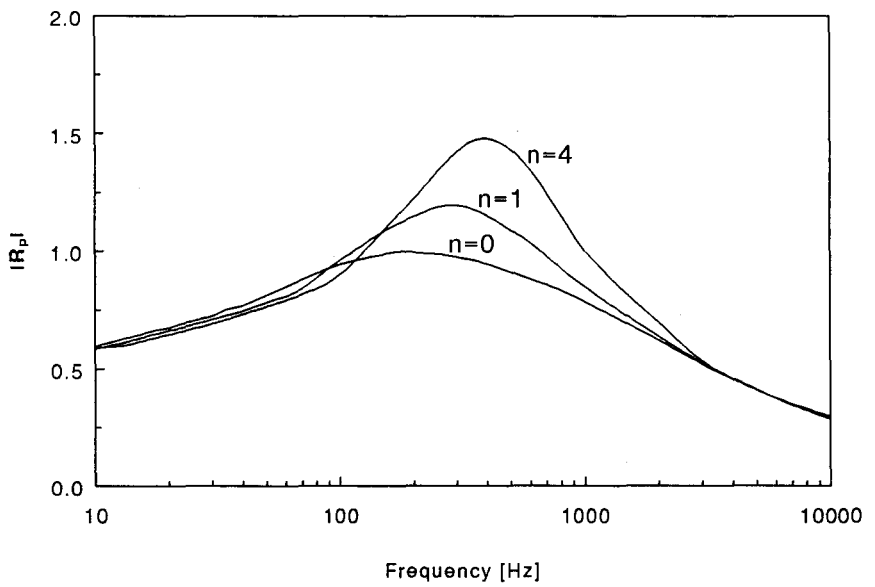

Figure 6.31: Effect of heat release distribution on the pressure coupled response function. By decreasing the reaction layer (increase of parameter n) the intrinsic stability increases, and the resonance peak shifts towards higher frequencies.

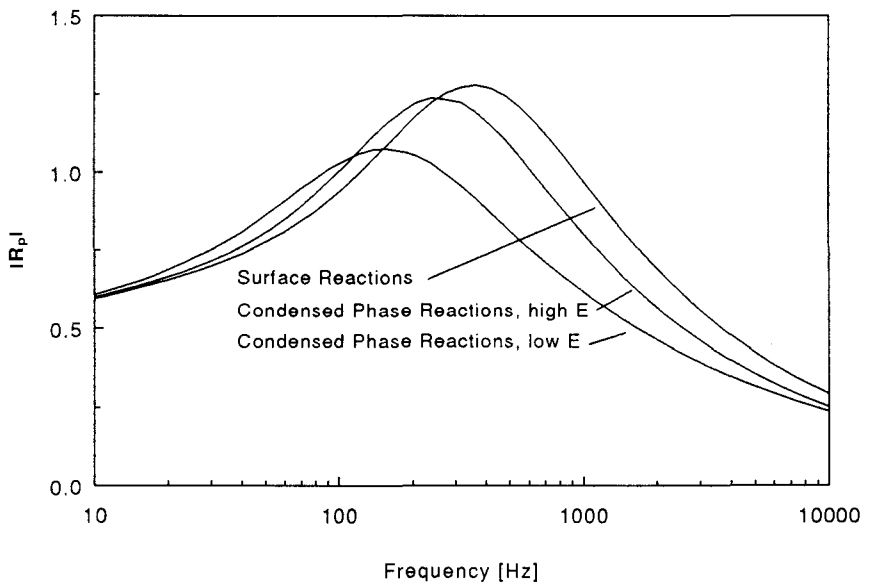

Figure 6.32: Effect of heat release distribution on the pressure coupled response function. Surface reactions (infinitesimally thin reaction layer) have the largest response. By increasing the reaction layer (decrease of activation energy) the intrinsic stability increases.

6.5.6 Response functions of AP-composites.

The current models for the determination of the response functions of solid propellants predict the experimental trends, but not within the desired accuracy. Several workers reported that the models could be improved by accounting for the chemical reactions in the solid phase. With the combustion model of chapter 5, this hypothesis can be verified.

Figure 6.33 shows two normalized pressure driven response functions as calculated for the reference propellant. One function is obtained assuming that all latent heats are zero, $Q_m = Q_{tra} = 0$. The other function is calculated for $Q_m \neq 0$ and $Q_{tra} \neq 0$. The figure shows a shift of the peak to a higher frequency, again due to an decrease in thermal layer thickness, see figure 6.8. It is also seen that the maximum decreases, i.e. the introduction of the latent heats predicts a more stable propellant response.

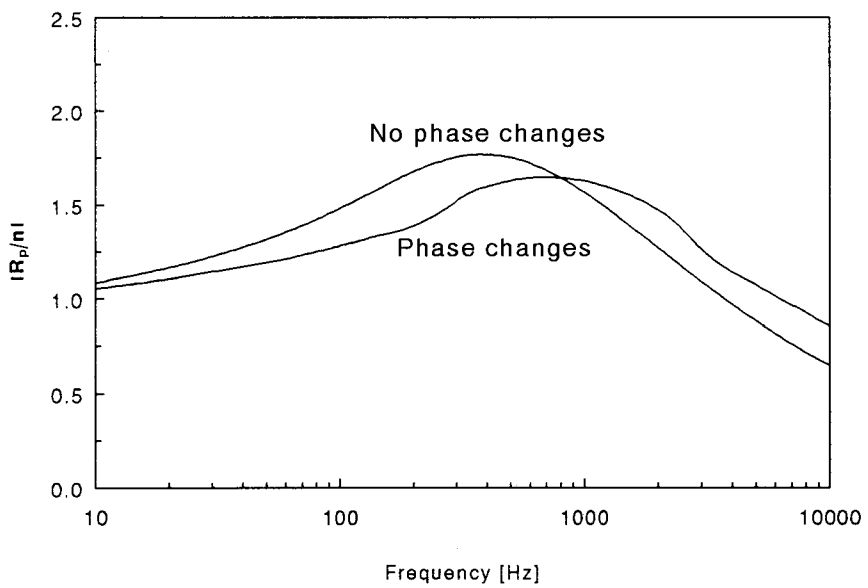

Figure 6.33: Effect of latent heats on the normalized pressure driven response function for the reference propellant.

A difficulty is the determination of the heat released in the solid phase, Q_c. Equation 3.10 gives a relation for Q_c for double base propellants. For composite propellants no such relation was found in the open literature, and an estimation has to be made.

Kishore and Verneker [32] have shown that composite propellant decomposition is a nonadditive phenomenon, i.e. the reactions in the condensed phase yield a larger exothermity of the propellant, compared to the additive heats of decomposition of its components.

The several processes in the condensed phase can be summarized as follows:

AP vaporization	requiring	1893	J/g propellant
AP decomposition	releasing	2879	J/g propellant
HTPB vaporization	requiring	251	J/g propellant
Overall exothermicity		735	J/g propellant (176 cal/g)

Measurements of the contribution from reactions in the solid phase to the overall heat release are not known from literature, so this contribution is neglected for the moment, and only the processes above are considered. The total exothermicity of the condensed phase is described by two terms in the model, the surface heat release, Q_s, and the condensed phase heat release Q_c. Because the relation between these two terms is not known, it is assumed that $Q_c = Q_s = 88$ cal/g (368 J/g). When calculations with this data were performed, it was found that the response function could not be calculated, because for these input data, the system is in a self-sustained regime (see section 7.1.2). The data used are actually measured values, so no self sustained burning is expected.

However, when also the phase transitions are accounted for, the calculations are performed in a normal combustion regime, and response functions can be calculated. This change of regime is caused by the stabilizing nature of the introduction of phase changes, because not all thermal energy is put in the heating of the solid, but also in the latent heats. Figure 6.34 shows the result of calculations where both condensed phase reactions, and phase transitions are accounted for. It turns out that the location of the maximum of the peak is determined by the phase transitions, because the resonance frequency is the same for both the calculations with and without the condensed phase heat release. The maximum of the response function is increased further.

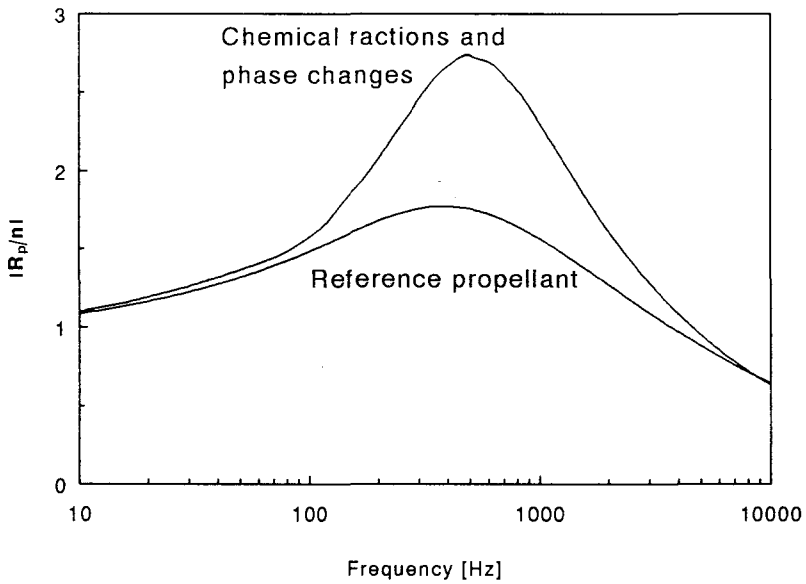

Figure 6.34: Effect of condensed phase heat release and phase transitions in the solid phase on the normalized pressure coupled response function.

Compared to the reference propellant a large increase in the response function is observed. It is concluded that chemical reactions and phase transitions have a pronounced effect on the pressure-coupled response function, and these effect may not be neglected.

6.5.7 Effect of gaseous heat release distribution.

Until now all calculations were performed with $\gamma = 0$ (KTSS-flame). By increasing γ, the heat is released wider zone (see figure 3.4). This means a weaker coupling between gas phase and condensed phase due to the decreased heat feedback from the gas phase, and hence a decrease of intrinsic combustion stability. The effect of increasing γ is illustrated in figure 6.35.

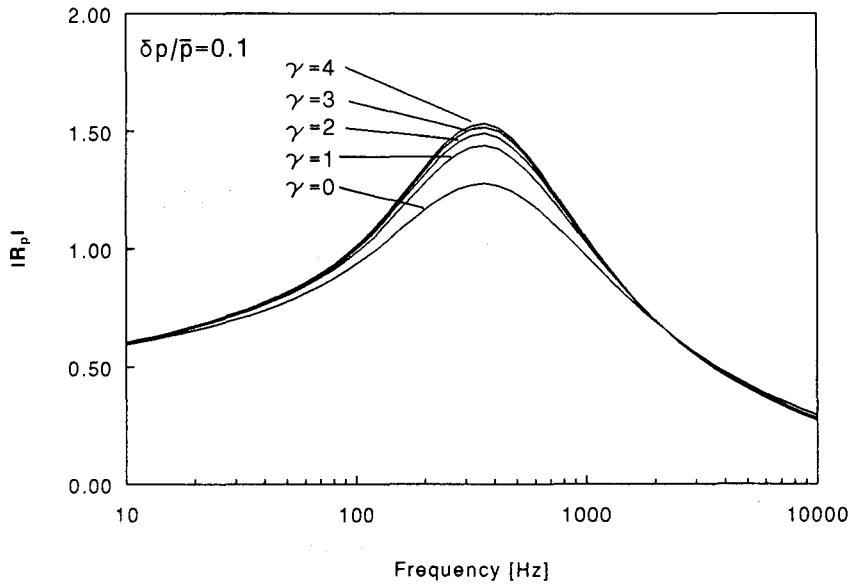

Figure 6.35: Effect of parameter γ on the pressure coupled response function ($\alpha = 0, \beta = 1$).

To illustrate the sensitivity of the pressure-driven response functions to the value of the parameter α several calculations with small changes in α were performed. Figure 6.36 shows that shifting the maximum heat release from the burning surface (increase of α) has a positive effect on the combustion stability.

Figures 6.35 and 6.36 show that the parameters α, β and γ influence the response function noticeable. So, both the condensed phase and the gas phase are important in determining the intrinsic instability of a solid rocket propellant.

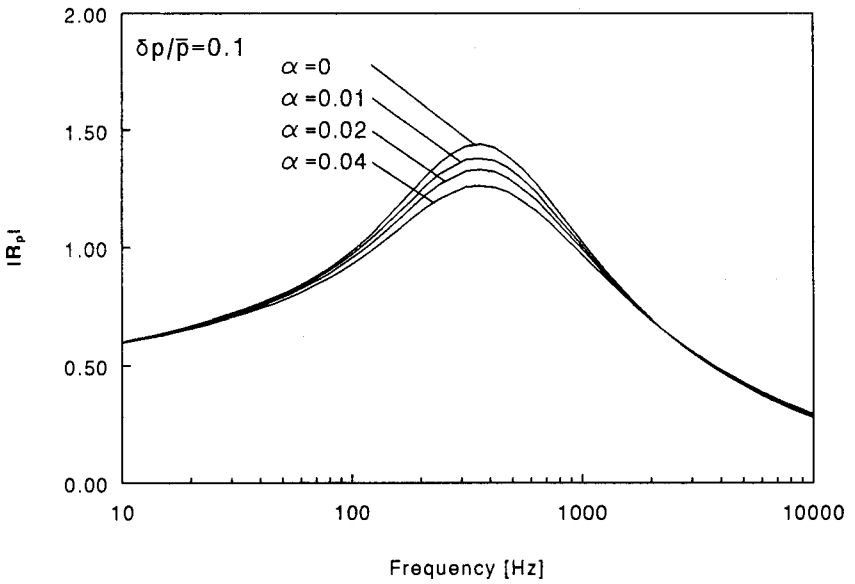

Figure 6.36: Effect of parameter α on the pressure coupled response function ($\gamma = 1$, and $\beta = 0.5$, except for $\alpha = 0$, then by definition $\beta = 1$).

Chapter 7

Intrinsic combustion instability.

Two types of stability can be distinguished. The first one is called the *static* stability, concerning the stability of an equilibrium situation. The self-sustained oscillatory combustion as already shortly mentioned in section 6.5.2 is an example of a static instable equilibrium. *Dynamic* combustion stability is concerned with the stability of burning transitions, between two stable steady state configurations, driven by an external time dependent forcing function, e.g. pressure. In this chapter only static stability will be discussed.

Two different methods of combustion instability analysis will be presented. Section 7.1 discusses a nonlinear approximate instability analysis based on an integral method as first published by DeLuca. In section 7.2 a method will be presented which determines the linear stability of an equilibrium state of a system. Both analysis will be applied to find the value of the surface heat release where static stability changes to static instability.

It should be noted however that any intrinsic stability theory can only extract the stability properties implicitly imbedded in the transient combustion model. It was assumed e.g. that the problem can be described by a one-dimensional model with homogeneous condensed phase, so possible instabilities due to three-dimensional effects, or heterogeneous condensed phase can not be predicted with this model.

7.1 Nonlinear combustion instability.

In this section a nonlinear approach towards combustion stability is presented. This method was first published by DeLuca, and is detailed in reference [18]. The approach is based on an integral method, transforming the energy equation of the solid phase (a partial differential equation, PDE) to an ordinary differential equation ODE. After transformation the question of stability is more traceable by means of the Lyapunov criterion. This approach preserves the nonlinearity of the equations.

The transformation of the PDE to an ODE is based on an approximate analytical procedure, which fully preserves the nonlinearity of the problem. This technique is similar to that proposed by Von Karman and Polhausen for boundary-layer analysis.

For static stability analyses, the initial condition is by definition the steady state profile,

i.e.

$$\Theta(X, \tau = 0) = \Theta_i(X) = \bar{\Theta}(X) \,, \tag{7.1}$$

whose stability is to be verified. So, this method requires an initial temperature profile. This profile can be obtained by using the numerical analysis of chapter 6.

The principle of transformation can be outlined with the help of figure 7.1. It is assumed that the steady state is perturbed over a layer thickness $\xi(\tau)$. The temperature disturbance profile is defined as the difference between the perturbed and the steady profile,

$$u(X, \tau) \equiv \Theta(X, \tau) - \bar{\Theta}(X) = u_s(\tau) \cdot u_c(X) \,. \tag{7.2}$$

The spatial dependence of the perturbation, $u_c(X)$ is *approximated* by a simple function, e.g. an exponential function, or polynomial, which has to satisfy the conditions $u_c(X = \xi) = 0$ and $u_c(X = 0) = 1$. By integrating the energy equation over this perturbed thermal layer the partial derivatives with respect to X disappear, and an ODE in τ remains. Appendix A.4 contains this, rather mathematical, derivation.

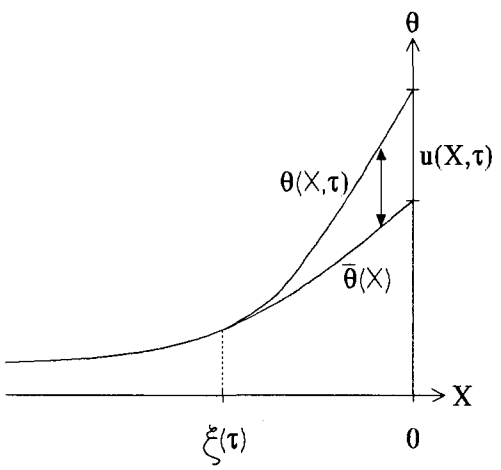

Figure 7.1: Condensed phase with two temperature profiles. The steady state profile $\bar{\Theta}(X)$, and the perturbed profile $\Theta(X, \tau)$. The perturbation is limited to the disturbance layer thickness $\xi(\tau)$.

In appendix A.4 it is shown that the energy equation of the condensed phase (PDE) can be reduced to an ODE by introduction of an approximation method. The result of this method is a nonlinear ODE in time describing the surface temperature history for a monotonic propagation in time of the disturbance layer thickness $\xi(\tau)$

$$\frac{d\Theta_s(\tau)}{d\tau} = f(\Theta_s - \bar{\Theta}_s) + g(\tau, \Theta_s - \bar{\Theta}_s) \,, \tag{7.3}$$

where f the static restoring function, and g the dynamic restoring function. The static restoring function describes the stability of an initial condition, in this chapter the steady

solution. The dynamic restoring function describes the stability during a time-dependent change of an external parameter such as e.g. the pressure, when two stable steady state situations exist.

7.1.1 Static restoring function.

The static restoring function $f(\Theta_s - \bar{\Theta}_s)$ was defined in appendix A.4. Figure 7.2 shows a typical plot of this function. The roots satisfy the relation $d\Theta_s(\tau)/d\tau = f(\Theta_s - \bar{\Theta}_s) = 0$, i.e. they are candidates for stationary burning. Root C is a trivial solution, describing the situation of a non-burning propellant. Generally two more roots exist, A and B.

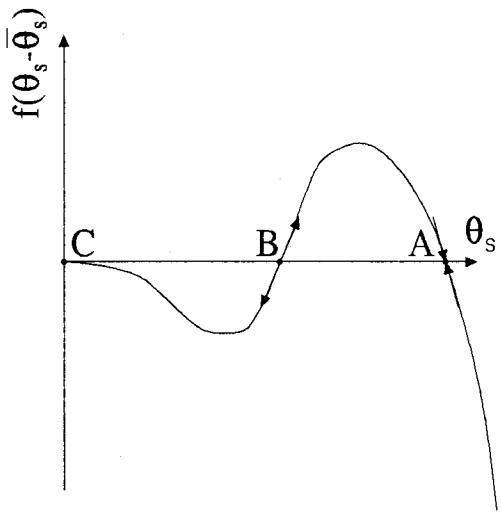

Figure 7.2: Typical plot of a static restoring function with three roots.

First consider root A. Assume that the surface temperature increases starting from root A., The time derivative of the surface temperature becomes negative, and the propellant forces the surface temperature to decrease in the direction of A. For the reverse situation it can be shown analogous that the response of the propellant also forces the surface temperature in the direction of A. So, it can be concluded that root A is stable.

The situation in root B is different. By the same arguments it can be shown that root B is unstable; any disturbance yields movement away from the point.

This static stability can be described by the first Lyapunov criterion: The solution of the nonlinear ODE of equation (A.58) is stable in the neighborhood of a given point $\bar{\Theta}_s^*$ if

$$\left(\frac{df(\Theta_s - \bar{\Theta}_s)}{d\Theta_s}\right)_{\bar{\Theta}_s = \bar{\Theta}_s^*} < 0\,. \tag{7.4}$$

The magnitude of the derivative $df/d\Theta_s$ at that point can be taken as measurement of the stability strength at that point.

By changing the operating conditions, the shape of the static restoring function changes. When the parameters are changed below or above a critical value, the number of roots may change suddenly. For example by increasing Q_s (or Q_c, or decreasing P), two new roots appear, D and E (figure 7.3).

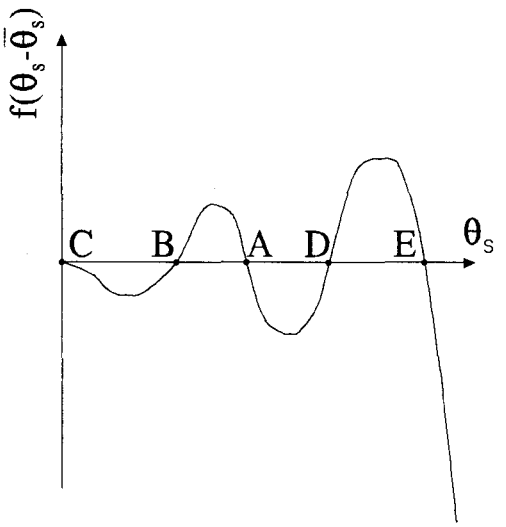

Figure 7.3: Typical plot of a static restoring function with five roots.

For the case of figure 7.3, two unstable roots (B and D) are next to the stable root (A). If the surface temperature passes the root B or D during a transient, the surface temperature will decelerate towards C (lower instability) or E (upper instability). For lower instability this means extinction of the propellant. The situation for upper stability is more complicated. For slow acceleration past D, slow deceleration from E towards A will occur, i.e. the equilibrium position will settle again. For strong acceleration past D, strong deceleration from E to D and A and possibly C (extinction) will occur, due to overstability.

By further changing the operating conditions, the restoring function of figure 7.4 may occur. In this situation, the A and D roots have moved towards each other, until coalescence and exchange of stability occurs. Then the B and D roots disappear. Under these circumstances, the only allowed solution is the trivial nonreacting configuration, represented by root C.

7.1.2 Bifurcation diagrams.

Different combustion regimes such as stable combustion, self-sustained oscillatory burning, and dynamic extinction can be distinguished. These regimes ar better understood if the roots of the static restoring function are plotted vs any of the parameters of interest. These plots are called bifurcation plots, because they show when and if the steady-state bifurcates from the time invariant A-root solution to e.g. a self-sustained oscillatory configuration. Reference [18] gives a large survey of different bifurcation plots for a large number of varying parameters.

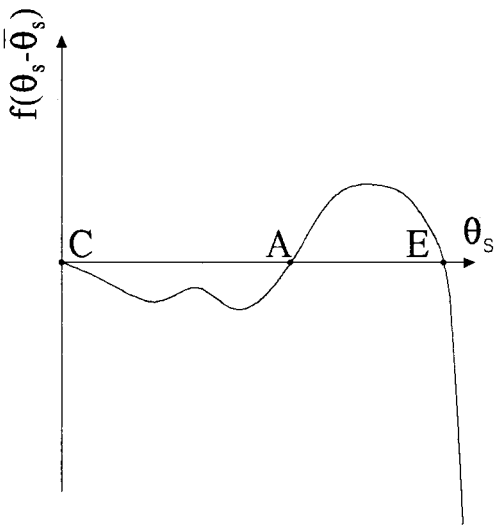

Figure 7.4: Typical plot of a static restoring function when roots B and D have exchanged stability. The only possible stable configuration is the nonreacting situation, represented by root C.

Self-sustained oscillatory combustion.

When figure 6.13 is carefully studied, it is noticed that the spikes in the response of the propellant seem to sustain, even when the external radiant flux has become constant, and no driving force is present anymore. This type of transient burning is called self-sustained oscillatory combustion. This phenomenon was extensively discussed by DeLuca [13]. It will be shown that the occurrence of self-sustained combustion is related to high values of the surface heat release, Q_s.

To verify the effect of the parameter Q_s on the transient burning, the surface temperature was monitored, during a very slow increase of Q_s. This increase is performed as follows. First the steady state is calculated. Then the value of Q_s is increased a small amount (typically 0.25%). Next, the propellant is allowed to relax for a large time (for example $100 \cdot t_c^*$). Then the value of Q_s is increased again, etc. This method closely resembles the "brute force method" of reference [44]. Figure 7.5 shows the result of such a calculation for constant thermal properties. The upper limit for Q_s is given by $Q_{s,max} = \int_{T_a}^{T_s} c_c(T)dT = 163.8$, for the nonlinearized KTSS flame. It is seen that for values of Q_s below a critical value, the surface temperature responds mildly to the increase in surface heat release. However, for values above 131.25, the response is fierce. It was verified that this response sustains when Q_s is not increased anymore. So, the oscillations are self-sustained. The sudden increase of Q_s acts as a disturbance triggering the self-sustained oscillations. This can also be achieved by any other disturbance, e.g. a pressurization or increase in external radiation. It was shown by DeLuca that the response in a self-sustained regime is only determined by the final operating conditions, and not by the history of the combustion [13].

When a part of figure 7.5 is enlarged, characteristic spikes are observed. Figure 7.6

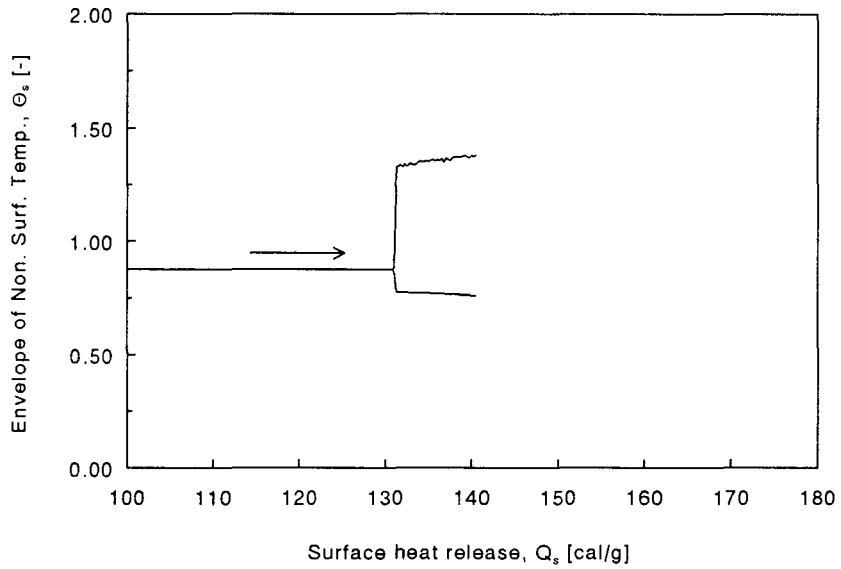

Figure 7.5: Envelope of the fluctuating surface temperature for a slowly varying surface heat release, Q_s.

shows the typical form of these spikes. The physical interpretation of these spikes is as follows: The intense heat source near the burning surface (large Q_s) results in a thermal "explosion", with associated high burning rates. During these high burning rate periods, the preheated zone is burned away completely. Due to the slow thermal layer build-up, the propellant recovers slowly, until a new thermal explosion occurs.

The behavior of figure 7.5 can be made clear by plotting the roots of the surface heat release as function of the surface temperature. In this way the bifurcation diagram of figure 7.7 is found. The calculations were performed for $n = 3$, as suggested by DeLuca [20]. For values of $Q_s < 108$, the situation of figure 7.2 exists. When the surface heat release is increased further, the roots D and E appear, according to figure 7.3. For $Q_s > 157$, the situation of figure 7.4 arises.

This bifurcation diagram shows that between A-D roots and B-D roots coalescence, selfsustained oscillatory burning may be found, i.e. $132 < Q_s < 157$. In this range the burning propellant bounces back and forth under the competing influence of D and E roots.

For $Q_s > 157$, no stable roots exist, and extinction occurs. This is verified by figure 7.8, which shows the extinction of the propellant for $Q_s = 160$, and a perturbation by a pressurization from 0.9 to 1.0 MPa.

The envelope of the surface temperature of figure 7.5 is obtained for an increasing surface heat release. When the surface heat release is then decreased, the situation of figure 7.9 occurs. It is seen that hysteresis emerges. This hysteresis cannot be predicted by the nonlinear stability analysis.

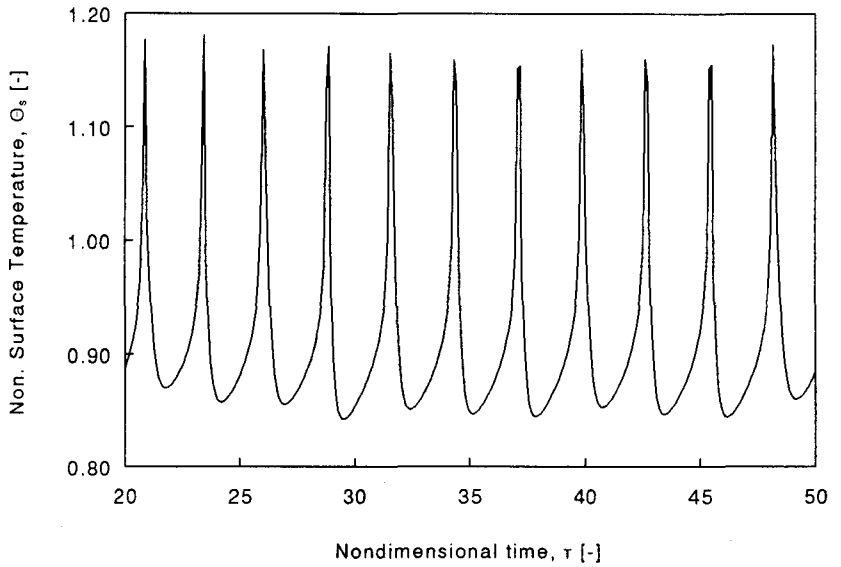

Figure 7.6: Characteristic spikes during self-sustained transient burning.

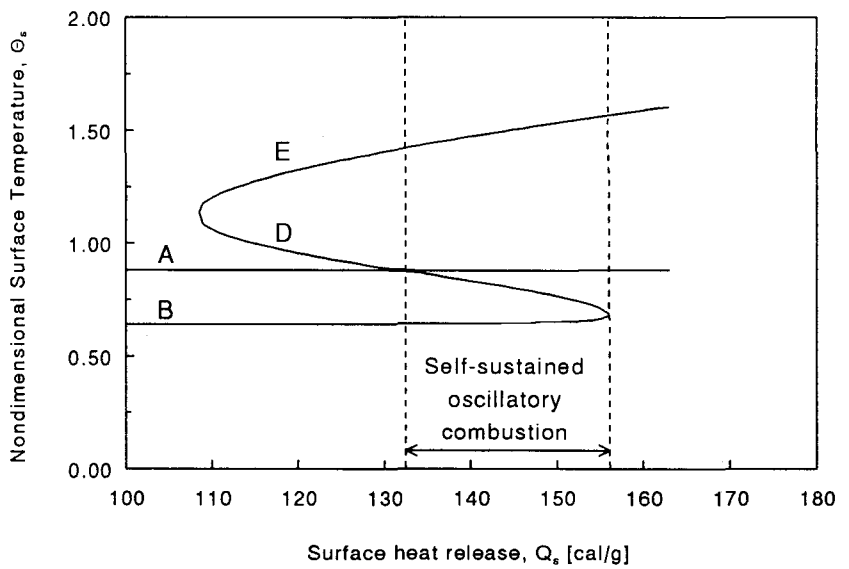

Figure 7.7: Bifurcation diagram at 1.0 MPa pressure. Shown are the roots of the static restoring function, (A, B, C, and D), and the envelope of a numerical calculation, by slowly varying Q_s.

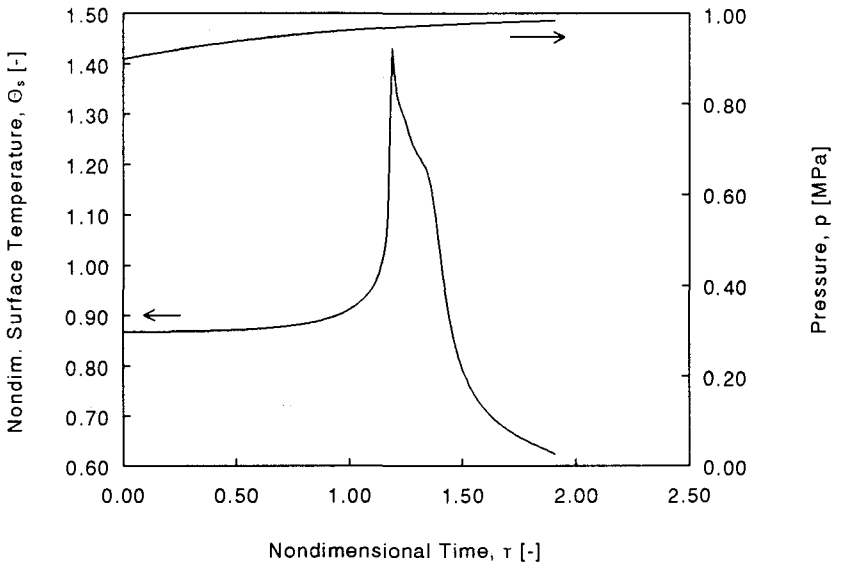

Figure 7.8: Extinction during a pressurization from 0.9 to 1.0 MPa.

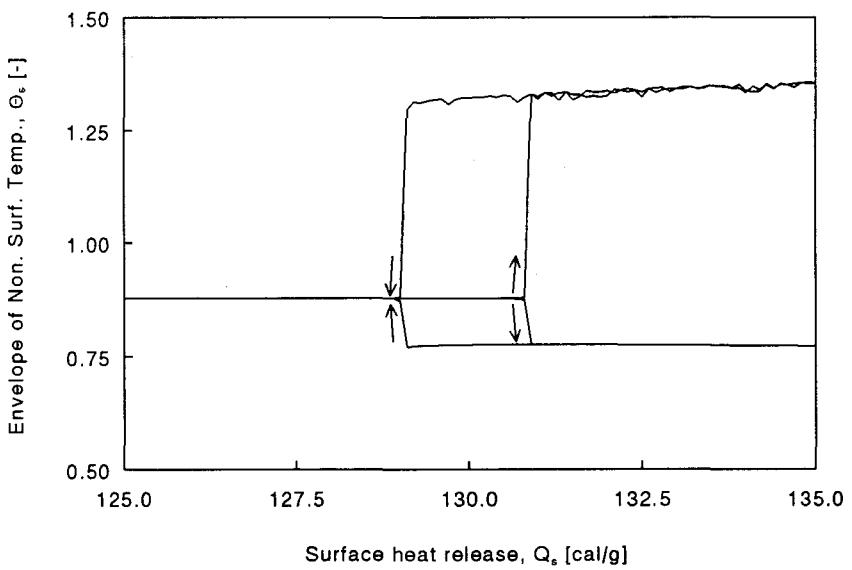

Figure 7.9: Hysteresis in the envelope of the fluctuating surface temperature for an increase in surface heat release, followed by a decrease in surface heat release.

7.2 Stability of an equilibrium of a linearized system

In case there are no time dependent external disturbances, the complete system of the solid propellant combustion can be considered as an autonomous system, described by a vector field $\vec{\vec{F}}$. The equilibrium vector $\vec{x}_{eq}$ describes the equilibrium point of the system. For a numerical calculation of the combustion of a solid rocket propellant, this vector is given by $\vec{x}_{eq} = (\Theta_2, \Theta_3, \ldots, \Theta_{NX-1})^T$, where NX the number of grid points in the numerical approach. Note that $\Theta_1 = \Theta_s$ and Θ_{NX} are not part of $\vec{x}_{eq}$, because they are determined by the boundary conditions.

The local behavior of the system near $\vec{x}_{eq}$ is determined by linearizing the vector field at $\vec{x}_{eq}$. The relation

$$\dot{\vec{\delta}}(t) = \nabla \vec{\vec{F}}(\vec{x}_{eq})\vec{\delta}(t) \,, \tag{7.5}$$

describes the time evaluation of a perturbation $\vec{\delta}(t)$ in the neighborhood of the equilibrium point $\vec{x}_{eq}$.

The solution of this equation describes the envelope of the disturbance $\vec{\delta}(t)$, due to the disturbance $\vec{\delta}_0$ at $t = 0$,

$$\vec{\delta}(t) = e^{\nabla \vec{\vec{F}}(\vec{x}_{eq})t}\vec{\delta}_0 \,. \tag{7.6}$$

Let the eigenvectors of $\nabla \vec{\vec{F}}(\vec{x}_{eq})$ be λ_i with corresponding eigenvectors $\vec{\eta}_i$, for $i = 2 \ldots NX - 1$, then this can be rewritten to give

$$\vec{\delta}(t) = c_2 e^{\lambda_2 t}\vec{\eta}_2 + \ldots + c_{NX-1}e^{\lambda_{NX-1}t}\vec{\eta}_{NX-1} \,, \tag{7.7}$$

where the coefficients c_i are chosen to satisfy the initial condition.

If λ_i is real, and $\vec{\eta}_i$ and c_i are also real, it is clear that the eigenvalue is the rate of contraction ($\lambda_i < 0$) or expansion ($\lambda_i > 0$) near $\vec{x}_{eq}$ in the direction of $\vec{\eta}_i$.

Because $\nabla \vec{\vec{F}}(\vec{x}_{eq})$ is a real matrix, complex eigenvalues occur only in complex conjugate pairs, from this it can be shown that the real part of λ_i gives the rate of expansion (or contraction) and the imaginary part of the eigenvalue is the frequency of rotation.

Depending on the position in the complex plane of the eigenvalues, several situations can be distinguished [44]:

- If $Re[\lambda_i] < 0$ for all λ_i then all perturbations tend toward 0 if $t \to \infty$, and $\vec{x}_{eq}$ is asymptotically stable.
- If $Re[\lambda_i] > 0$ for all λ_i then all perturbations grow with time and $\vec{x}_{eq}$ is unstable.
- If there exists i and j such that $Re[\lambda_i] < 0$ and $Re[\lambda_j] > 0$, then $\vec{x}_{eq}$ is non-stable.

The stability of an equilibrium situation for solid rocket propellants is tested as follows:

1. At $\tau = 0$ the steady-state is calculated, this defines the state vector $\vec{x}_{eq}$.

2. At $\tau = \Delta\tau$ the components of this state are successively disturbed by the perturbation vector $\vec{\delta}$, of which the components are given by $(\vec{\delta})_i = 0.05\delta_{i,j}\bar{\Theta}_i$, for $j = 2, 3, \ldots, NX - 1$ ($\delta_{i,j}$ is Kronecker-delta). This means that each of the different components is disturbed by 5% of its steady state value. Also calculations for a 1% perturbation have been carried out.

3. The disturbed situation at $\tau = 2\Delta\tau$ is calculated, $\vec{x}_{dis}$. Points 2 and 3 are repeated for all j.

4. From the above calculations $\nabla\vec{\vec{F}}$ can be calculated according to

$$\left(\nabla\vec{\vec{F}}\right)_{i,j} = \frac{(\vec{x}_{dis})_j - (\vec{x}_{eq} + \vec{\delta})_j}{\Delta\tau\,\vec{\delta}_i} . \tag{7.8}$$

5. The eigenvalues of $\nabla\vec{\vec{F}}$ are calculated with the Mathcad program. Because the maximum number of points is limited, only the points most closely to the surface are considered, i.e. $j = 2, 3, \ldots, M$ (typically $M = 300$ and $NX = 2500$).

For the situation of self-sustained oscillator combustion (section 7.1.2), the stability was verified with the integral method. These results can be compared with the results of the linear stability calculations.

Table 7.1 shows the calculated eigenvalues for several values of the parameter Q_s. For $Q_s = 100$ only negative eigenvalues are found, implying a stable equilibrium. This situation holds, until Q_s is increased above 105. At that time a positive eigenvalue emerges, and the equilibrium situation is not longer linear stable anymore. When the value of 105 is compared with the transition value found from the figures 7.5, and 7.7 an discrepancy is seen. The linear stability analysis predicts that the propellant becomes unstable at lower values of Q_s.

It was considered that the disturbance amplitude of 5% was to large, and would not reveal the eigenvalues of the linearized system. Hence the calculations were repeated for a disturbance of 1%. As seen from table 7.1 the difference between the two calculations is very small, so the system can be seen linear, even for the 5% disturbance.

As explained before, the steady state at $\tau = 0$ is perturbed at $\tau = \Delta\tau$ and then the temperature profile at $\tau = 2\Delta\tau$ is calculated. The numerical method used calculates the new profile based on the two previous calculations. For stable situations the perturbed temperature should return to its steady state value, but because of the memory of the numerical method this means a very large time derivative.

To determine the effect of the numerical method, also calculations were performed where the profile at $\tau = 0$ was also perturbed. This means that the calculations for $\tau = 2\Delta\tau$ are started with two identical thermal profiles at $\tau = 0$ and $\tau = \Delta\tau$. The result of these

Q_s	Eigenvalues, 1% disturbance	Eigenvalues, 5% disturbance
100	-0.493, -7.582, -9.200, ...	-0.491, -7.582, -9.200, ...
105	-0.204, -7.559, -9.197, ...	-0.202, -7.559, -9.187, ...
110	+0.118, -7.536, -9.195, ...	+0.120, -7.535, -9.195, ...
120	+0.882, -7.488, -9.190, ...	+0.886, -7.487, -9.189, ...
130	+1.862, -7.438, -9.184, ...	+1.869, -7.437, -9.184, ...
140	+3.154, -7.387, -9.179, ...	+3.168, -7.385, -9.179, ...
150	+4.935, -7.332, -9.173, ...	+4.960, -7.331, -9.173, ...

Table 7.1: Calculated eigenvalues of $\nabla\vec{F}$ for several values of the parameter Q_s, and two different disturbances.

calculations are summarized in table 7.2. It is seen that for these calculations the transition from stable to unstable combustion is between $Q_s = 140$ and $Q_s = 150$, which is above the value of 131 found from the nonlinear combustion theory.

Q_s	Eigenvalues, 1% disturbance
100	-2.870, -8.187, -9.400, ...
120	-1.838, -8.116, -9.392, ...
130	-1.104, -8.079, -9.388, ...
140	-0.136, -8.040, -9.384, ...
150	+1.197, -7.999, -9.380, ...

Table 7.2: Calculated eigenvalues of $\nabla\vec{F}$ for several values of the parameter Q_s. For these calculations the temperature profile was perturbed at $\tau = 0$ and at $\tau = \Delta\tau$.

Now return the the first type of calculations with only a perturbation at $\tau = \Delta\tau$. To clarify the difference between the linearized and nonlinear stability approaches, the evolution of the $|\vec{x}_{dis}|$ was monitored. According to equation 7.7 the modulus of the disturbance, and hence $|\vec{x}_{dis}| = |\vec{x}_{eq} + \vec{\delta}|$, increases exponentially in time. So by plotting $|\vec{x}_{dis}|$ as function of the time, it becomes clear whether the disturbance grows in time, or decreases in time. Figure 7.10 shows the evolution of the normalized modulus. For $Q_s \leq 130$ the modulus reaches the steady state value after some time. For $Q_s \geq 135$ the modulus increases, suggesting a unstable situation. The results of this calculation are comparable with that of the nonlinear combustion analysis, based on the integral method, which is not surprising because the calculations of figure 7.10 are nonlinear as well.

It can be concluded that these linear stability calculations are very sensitive to the numerical approach. Dependent on the approach, they overpredict, or underpredict the stability boundary of the equilibrium state.

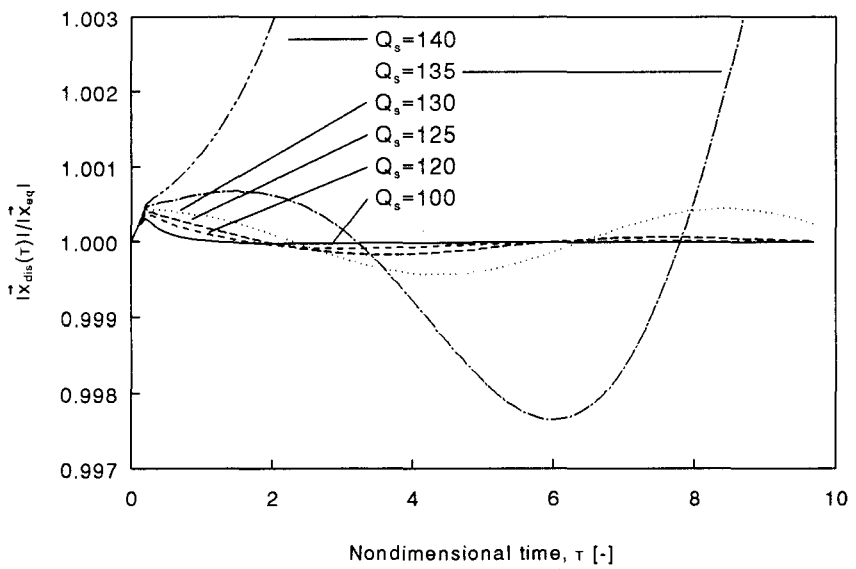

Figure 7.10: Plot of the normalized modulus of $\vec{x}_{dis}$ as function of the time. For $Q_s \leq 130$ the modulus returns to it's value at $\tau = 0$. For larger values the equilibrium is unstable, diverging from the steady situation because of the perturbation at $\tau = 0.1$.

Chapter 8

Conclusions and suggestions for future work.

It is shown that the steady state temperature profiles in the steady state are very different when calculated for constant thermal properties, as when calculated for actual measured temperature dependent thermal properties.

As an extension to this steady state burning it is shown that the transient combustion of solid rocket propellants is also largely affected by the introduction of temperature dependent thermal properties. For the situation of temperature dependent properties, the response becomes smaller, and the resonance frequency shifts to higher frequencies, because of the decrease in thermal layer thickness.

The introduction of phase transitions of AP to the model shows that these transitions can not be neglected. Phase transitions yield a more intrinsic stable propellant (lower resonance peak), with a higher resonance frequency.

Radiation driven transient burning is discussed briefly and the nonlinear numerical calculations show that the mean value of the transient radiation disturbance affects the radiation driven response function.

Comparison of subsurface and surface reactions shows that surface reactions yield a propellant which is less stable as compared to the propellant with the same amount of subsurface reactions. So, the classical linear calculations, which consider surface reactions only, tend to overpredict the intrinsic instability. Surface reactions are not practical, but just a mathematical limit of a very thin reaction zone near the surface.

It is shown that the response of the system may be considered linear for disturbances up to 1% of their mean value. For the common 10% perturbations, a deviation is seen from the linearized analysis.

For very high values of the surface heat release, self-sustained oscillations may exist. The occurrence of these oscillations is verified by a brute force method. Also nonlinear and linear combustion stability analysis have been performed, to show that the steady state in this case is unstable. The linear stability approach is unable to calculate the value of the surface heat release where self-sustained oscillatory combustion occurs. The nonlinear analysis however, show good agreement with the numerical calculations.

It is shown in this thesis that reactions, and other processes in the condensed phase have a pronounced effect on the intrinsic combustion stability of a solid rocket propellant. Hence a better knowledge should be obtained about condensed phase processes. Accurate temperature profiles measured by small thermocouples can be of great help to gain more information about the condensed phase.

Theoretically, the models can be improved by the introduction of an heterogeneous condensed phase. Calculations in this thesis show that the typical thermal layer thickness is of the same order as the typical AP particle size, so the homogeneous treatment of the condensed phase is questionable.

The flame models used at the moment are simple, but mathematically traceable. A systematical study towards the combustion stability for different flame models would reveal whether the current flame models cover the the real situation accurate enough. In recent studies the flame models have been extended to include the actual chemical reactions taking place. These models are less general, but describe the multiple flame processes. A comparison between these flames, and the common flames used for intrinsic combustion stability studies, could provide the knowledge whether these new models have an decisive effect on combustion stability.

Accurate experimental data should be generated to be able to compare theoretical results with measured data.

Bibliography

[1] Ames, W.F.
Numerical Methods for Partial Differential Equations
Academic Press, inc., San Diego, 1961.

[2] Beckstead, M.W., Derr, R.L, and Price, C.F.
A Model of Composite Solid-Propellant Combustion Based on multiple flames
AIAA Journal **8**, 2200 (1970).

[3] Beckstead, M.W., and Culick, F.E.C.
A Comparison of Analysis and Experiment for Solid-Propellant Combustion Instability
AIAA Journal **9**, 147 (1971).

[4] Brewster, M.Q., Hites, M.H., and Son, S.F.
Dynamic Burning Rate Measurements of Metalized Composite Propellants Using the Laser-Recoil Technique
Combustion and Flame **94**, 178 (1993).

[5] Brigham, E.O.
The Fast Fourier Transform
Prentice-Hall, Inc., Englewood Cliffs (1974).

[6] Brown, R.S., Muzzy, R.J., and Steinle, M.E.
Effect of Surface Reactions on Acoustic Response of Solid Propellants
AIAA Journal **5**, 1718 (1967).

[7] Brownlee, W.G.
Nonlinear Axial Combustion Instability in Solid Propellant Motors
AIAA Journal **2**, 275 (1964).

[8] Caveny, L.H., and Pittman, C.U.
Contribution of Solid-Phase Heat Release to AP Composite Propellant Burning Rate
AIAA Journal **6**, 1461 (1968).

[9] Clavin, P., and Lazimi, D.
Theoretical Analysis of Oscillatory Burning of Homogeneous Solid Propellant Including Non-Steady Gas Phase Effects
Combustion Science and Technology **83**, 1 (1992).

[10] Cohen, N.S, and Strand, L.D.
Analytical Model of High-Pressure Burning Rates in a Transient Environment
AIAA Journal **18**, 968 (1980).

[11] Cozzi, F.
Risposta in Frequenza Teorica e Sperimentale di Propellenti Solidi Soggetti a Radiazione Laser
Thesis (in Italian), Politecnico di Milano, Italy (1993).

[12] Culick, F.E.C.
A Review of Calculations for Unsteady Burning of a Solid Propellant
AIAA Journal **6**, 2241 (1968).

[13] DeLuca, L.
Self-sustained Oscillatory Combustion of Solid Rocket Propellants
Agard Conference Proceedings, No. 259, Solid Rocket Motor Technology (1979).

[14] DeLuca, L.
Frequency Response Function of Burning Solid Propellants
Meccanica, December 1980, 195.

[15] DeLuca, L., Riva, G., Bruno, C., Zanotti, C., Dondé, Volpi, A., Grimaldi, C., and Colombo, G.
Burning Stability of Double-Base Propellants
AGARD PEP 66th (A) Specialists' Meeting on Smokeless Propellants, Conference Proceedings No. 391, paper 10, (1986).

[16] DeLuca, L.
A Critical Review of Solid Rocket Propellant Transient Flame Models
Pure and Applied Chemistry **62**, 825 (1990).

[17] DeLuca, L., and Galfetti, L.
Combustion Modeling and Stability of Double Base Solid Rocket Propellants
Modern Research Topics in Aerospace Propulsion, Chapter 7, Springer Verlag, New York (1991).

[18] DeLuca, L.
Theory of Nonsteady Burning and Combustion Stability by Flame Models
In: Nonsteady Burning and Combustion Stability of Solid Propellants, edited by L. DeLuca, E.W. Price, and M. Summerfield, AIAA Progress in Astronautics and Aeronautics Vol. 143, Chapter 14, (1992).

[19] DeLuca, L., Cozzi, F., Di Silvestro, R., and Mazza, P.
Frequency Response of Radiation Driven Burning of Solid Rocket Propellants
ISTS 94-a-26, 19th International Symposium on Space Technology and Science, Yokohama, Japan, May 15-24, 1994.

[20] DeLuca, L.
Private communication 1995.

[21] DeLuca, L., Di Silvestro, R., and Cozzi, F.
Intrinsic Combustion Instability of Solid Energetic Materials
Journal of Propulsion and Power **11**, 804 (1995).

[22] Denison, M.R., and Baum, E.
A Simplified Model of Unstable Burning in Solid Propellants
ARS Journal **31**, 1112 (1961).

[23] Elbe, G. von, Friedman, R., Levy, J.B., and Adams, S.J.
Research on Combustion in Solid Rocket Propellants with Hydrazine Nitroform as a Propellant Ingredient
Kinetics and Combustion Division, Atlantic Research Corporation, Shirley Highway at Edsall Road, Alexandria, Virginia, July 21, 1964.

[24] Finlinson, J., Hanson-Parr, D., Son, S.F., and Brewster, M.Q.
Measurement of Propellant Combustion Response to Sinusoidal Radiant Heat Flux
AIAA Paper 91-0204 (1991).

[25] Galfetti, L., Riva, G. and Bruno, C.
Numerical Computations of Solid-Propellant Nonsteady Burning in Open or Confined Volumes
In: Nonsteady Burning and Combustion Stability of Solid Propellants, edited by L. DeLuca, E.W. Price, and M. Summerfield, AIAA Progress in Astronautics and Aeronautics Vol. 143, Chapter 16 (1992).

[26] Gordon, S., and McBride, B.J.
Computer Program for Calculation of Complex Chemical Compositions, Rocket Performance, Incident and Reflected Shocks, and Chapman-Jouget Detonations
NASA SP-273, NASA Lewis Research Center, Interim Revision, (1976).

[27] Green, L.
Some Properties of Solid Propellant Burning
Jet Propulsion **28**, 386 (1958).

[28] Guirao, C., and Williams, F.A.
A Model for Ammonium Perchlorate Deflagration between 20 and 100 atm
AIAA Journal **9**, 1345 (1971).

[29] Hart, R.W.
Acoustic Interaction with a Burning Propellant Surface
Journal Chem. Phys. **30**, 1503 (1959).

[30] Ibiricu, M.M., and Williams, F.A.
Influence of Externally Applied Thermal Radiation on the Burning Rates of Homogeneous Solid Propellants
Combustion and Flame **24**, 185 (1975).

[31] Ishihara, A., Brewster, M.Q., Sheridan, T.A., and Krier, H.
The Influence of Radiative Heat Feedback on Burning Rate in Aluminized Propellants
Combustion and Flame **84**, 141 (1991).

[32] Kishore, K., and Verneker, V.R. Pai
Condensed Phase Reactions in Solid Propellants
AIAA Journal **13**, 1240 (1975).

[33] Krier, H., T'ien, J.S., Sirignano, W.A., and Summerfield, M.
Nonsteady Burning Phenomena of Solid Propellants: Theory and Experiments
AIAA Journal **6**, 278 (1968).

[34] Kubota, N., and Sonobe, T.
Combustion Mechanism of Azide Polymer
Propellants, Explosives, Pyrotechnics **13**, 172 (1988).

[35] Kumar, R.N, and Culick, F.E.C.
Role of Condensed Phase Details in the Oscillatory Combustion of Composite Propellants
AIAA Paper 73-218 (1973).

[36] Kuo, K.K.
Principles of Combustion
John Wiley & Sons, New York, (1986).

[37] Kuo, K.K., and Gore, J.P.
Transient Burning of Solid Propellants
In: Fundamentals of Solid-Propellant Combustion, edited by K.K. Kuo, and M. Summerfield, AIAA Progress in Astronautics and Aeronautics Vol. 90, Chapter 11 (1984).

[38] Lengellé, G., Fourest, B., Godon, J.C., and Guin, C.
Condensed Phase Behavior and Ablation Rate of Fuels for Hybrid Propulsion
AIAA Paper 93-2314 (1993).

[39] Marxmann, G.A., and Wooldridge, C.E.
Effect of Surface Reactions on the Solid Propellant Response Function
AIAA Journal **6**, 471 (1968).

[40] Merkle, C.L., Turk, S.L., and Summerfield, M.
Extinguishment of Solid Propellants by Depressurization: Effects of Propellant Parameters
AIAA Paper 69-176 (1969).

[41] Mihlfeith, C.M., Baer, A.D., and Ryan, N.W.
Propellant Combustion Instability as Measured by Combustion Recoil
AIAA Journal **10**, 1280 (1972).

[42] Nogotov, E.F.
Applications of Numerical Heat Transfer
Unesco, Paris (1978).

[43] Novozhilov, B.V.
Theory of Nonsteady Burning and Combustion Stability of Solid Propellants by the Zeldovich-Novozhilov Method
In: Nonsteady Burning and Combustion Stability of Solid Propellants, edited by L. DeLuca, E.W. Price, and M. Summerfield, AIAA Progress in Astronautics and Aeronautics Vol. 143, Chapter 15 (1992).

[44] Parker, T.S., and Chua, L.O.
Practical Numerical Algorithms for Chaotic Systems
Springer Verlag, New York (1989).

[45] Richtmyer, R.D., and Morton, K.W.
Difference Methods for Initial-Value Problems
Sec. Ed., Interscience, New York (1967).

[46] Rossre, W.A., Inami, S.H., and Wise, H.
Thermal Diffusivity of Ammonium Perchlorate
AIAA Journal **4**, 663 (1966).

[47] Sabadell, A.J., Wenograd, J., and Summerfield, M.
Measurement of Temperature Profiles through Solid-Propellant Flames Using Fine Thermocouples
AIAA Journal **3**, 1580 (1965).

[48] Saitoh, T, Hori, K, Notono, K, and Iwama, A.
Synthesis and Physico-Chemical Properties of Glycidyl Azide Polymer (GAP) and the Application of GAP/Ammonium Nitrate based Propellants to a small Motor
21st International Annual Conference of ICT (1990).

[49] Schöyer, H.F.R., Schnorhk, A.J., Korting, P.A.O.G., Lit, P.J. van, Mul, J.M., Gadiot, G.M.H.J.L., and Meulenbrugge, J.J.
High-Performance Propellants Based on Hydrazinium Nitroformate
Journal of Propulsion and Power **11**, 856 (1995).

[50] Schor, de B.B., and Toni, J.E.
Emissivity Measurements of Solid Propellants
Thermochimica Acta **16**, 377 (1976).

[51] Son, S.F., and Brewster, M.Q.
Linear Burning Rate Dynamics of Solids Subjected to Pressure or External Radiant Heat Flux Oscillations
Journal of Propulsion and Power **9**, 222 (1993).

[52] Son, S.F, and Brewster, M.Q.
Unsteady Combustion of Homogeneous Energetic Solids Using the Laser-Recoil Method
Combustion and Flame **100**, 283 (1995).

[53] Sills, J.A.
Transformations for Infinite Regions and their Applications to Flow Problems
AIAA Journal **7**, 117 (1969).

[54] Strand, L.D., Weil, M.T., and Cohen, N.S.
Solid Propellant Combustion Response to Oscillatory Radiant Heat Flux
AIAA Paper No. 89-2667, 1989.

[55] Summerfield, M., Caveny, L.H., Battista, R.A., Kubota, N., Gostintsev, Yu. A., and Isoda, H.
Theory of Dynamic Extinguishment of Solid Propellants with Special Reference to Nonsteady Heat Feedback Law
Journal of Rockets and Spacecraft **8**, 251 (1971).

[56] Sutton, G.P.
Rocket Propulsion Elements: An Introduction to the Engineering of Rockets
Sixth Edition, J. Wiley & Sons, Inc., New York (1992).

[57] Zanotti, C., and Volpi, A.
Measuring Thermodynamic Properties of Burning Propellants
In: Nonsteady Burning and Combustion Stability of Solid Propellants, edited by L. DeLuca, E.W. Price, and M. Summerfield, AIAA Progress in Astronautics and Aeronautics Vol. 143, Chapter 5 (1992).

[58] Zarko, V.E., Simeonenko, V.N., and Kiskin, A.B.
Nonstationary Combustion of Condensed Substances Subjected to Radiaton
Combustion, Explosion and Shock Waves **23**, 16 (1987).

[59] Zarko, V.E., Simonenko, V.N., and Kiskin, A.B.
Radiation-Driven Transient Burning: Experimental Results
Combustion Stability of Solid Propellants, edited by L. DeLuca, E.W. Price, and M. Summerfield, AIAA Progress in Astronautics and Aeronautics Vol. 143, Chapter 10 (1992).

[60] Zarko, V.E., Simonenko, V.N., and Kiskin, A.B.
Study of Solid Propellant Combustion under External Radiation
Defence Science Journal **42**, 183 (1992).

[61] Zenin, A.A.
Universal Dependence for Heat Liberation in the K-Phase and Gas Macrokinetics in Ballistic Powder Combustion
Combustion, Explosion and Shock Waves **19**, 444 (1983).

Appendix A

Derivations.

A.1 Derivation of the steady state thermal profile.

In this section the steady state thermal profile in the condensed phase is calculated, neglecting chemical reactions in this phase. For convenience, write from now for $I_0 = (1 - \bar{\bar{r}}_\lambda)I_0$. Starting with the steady-state energy equation for the solid (equation (4.1))

$$r_b \frac{d\bar{T}}{dx} = \alpha_c \frac{d^2\bar{T}}{dx^2} + N_t \frac{\bar{\bar{a}}_\lambda}{\rho_c c_c} I_0 e^{\bar{\bar{a}}_\lambda x}. \tag{A.1}$$

The steady state temperature at position x can be written as [11]

$$\bar{T}(x) = \bar{T}_c(x) + \bar{T}_r(x), \tag{A.2}$$

where $\bar{T}_c(x)$ the thermal profile due to heat conduction, and $\bar{T}_r$ the thermal profile due to radiation. Substitution in the energy equation yields the following set of equations

$$\bar{r}_b \frac{d\bar{T}_c}{dx} = \alpha_c \frac{d^2\bar{T}_c}{dx^2} \tag{A.3}$$

$$\bar{r}_b \frac{d\bar{T}_r}{dx} = \alpha_c \frac{d^2\bar{T}_r}{dx^2} + N_t \frac{\bar{\bar{a}}_\lambda}{\rho_c c_c} I_0 e^{\bar{\bar{a}}_\lambda x}, \tag{A.4}$$

with boundary conditions

$$\bar{T}_c(x = 0) = \bar{T}_{s,c}\,, \tag{A.5}$$

$$\bar{T}_c(x \to -\infty) = T_a\,, \tag{A.6}$$

$$\bar{T}_r(x \to -\infty) = 0\,, \tag{A.7}$$

$$\frac{d\bar{T}_r}{dx}(x \to -\infty) = 0\,, \tag{A.8}$$

where $\bar{T}_{s,c}$ the surface temperature resulting from heat conduction only. Equation (A.3) and its boundary conditions yield the familiar exponential profile

$$\bar{T}_c(x) = T_a + (\bar{T}_{s,c} - T_a) e^{\bar{r}_b x/\alpha_c}. \tag{A.9}$$

The next problem is to find the solution of the differential equation for $\bar{T}_r(x)$. According to equation (A.7), the solution has to be zero far in the deep. Because of this

$$\bar{T}_r(x) = a\left(e^{\alpha x} - e^{\beta x}\right) \tag{A.10}$$

is tried as solution. Substituting of this function in equation (A.4), results in:

$$\alpha = \bar{\bar{a}}_\lambda, \tag{A.11}$$

$$\beta = \frac{\bar{r}_b}{\alpha_c}, \tag{A.12}$$

$$a = \frac{N_t \bar{I}_0}{\rho_c c_c(\bar{r}_b - \alpha_c \bar{\bar{a}}_\lambda)}. \tag{A.13}$$

So the steady state thermal profile can be written as

$$\bar{T}(x) = T_a + (\bar{T}_{s,c} - T_a)e^{\bar{r}_b x/\alpha_c} + \frac{N_t \bar{I}_0}{\rho_c c_c(\bar{r}_b - \alpha_c \bar{\bar{a}}_\lambda)}\left(e^{\bar{\bar{a}}_\lambda x} - e^{\bar{r}_b x/\alpha_c}\right). \tag{A.14}$$

A.2 Derivation of the transient thermal profile.

The transient thermal profile is obtained from linearizing the energy differential equation (equation (4.1))

$$\frac{\partial T}{\partial t} + \bar{r}_b \frac{\partial T}{\partial x} = \alpha_c \frac{\partial^2 T}{\partial x^2} + N_t \frac{\bar{\bar{a}}_\lambda}{\rho_c c_c} I_0 e^{\bar{\bar{a}}_\lambda x}. \tag{A.15}$$

This linearizing is done by substituting

$$T(x,t) = \bar{T}(x) + T'(x)e^{i\omega t} \tag{A.16}$$

$$I_0(x,t) = \bar{I}_0(x) + I_0'(x)e^{i\omega t}, \tag{A.17}$$

and neglecting terms of second order. When the differential equations for the steady state (equations (A.3) and (A.4)) are subtracted, the differential equation for the fluctuating portion of T is found

$$i\omega T' + \bar{r}_b \frac{dT'}{dx} = \alpha_c \frac{d^2 T'}{dx^2} + N_t \frac{\bar{\bar{a}}_\lambda}{\rho_c c_c} I_0' e^{\bar{\bar{a}}_\lambda x}. \tag{A.18}$$

As for the steady state, the fluctuating portion of the temperature profile can be written as

$$T'(x) = T_c'(x) + T_r'(x)\,. \tag{A.19}$$

Substitution of this equation in equation (A.18) yields two differential equations,

$$i\omega T_c' + \bar{r}_b \frac{dT_c'}{dx} = \alpha_c \frac{d^2 T_c'}{dx^2} \tag{A.20}$$

$$i\omega T_r' + \bar{r}_b \frac{dT_r'}{dx} = \alpha_c \frac{d^2 T_r'}{dx^2} + N_t \frac{\bar{\bar{a}}_\lambda}{\rho_c c_c} I_0' e^{\bar{\bar{a}}_\lambda x}\,. \tag{A.21}$$

The boundary conditions are

$$T_c'(x \to -\infty, t) = 0 \tag{A.22}$$
$$T_c'(x = 0, t) = T_{x=0,c}'(t) \tag{A.23}$$
$$T_r'(x \to -\infty, t) = 0 \tag{A.24}$$
$$\frac{dT_r'}{dx}(x \to -\infty, t) = 0 \tag{A.25}$$

The solution of equation (A.20) and its boundary conditions can be found by substituting

$$T_c'(x) = T_{x=0,c}'(t) e^{\lambda \epsilon x}, \tag{A.26}$$

where λ and ϵ have to be determined. Note that the boundary conditions are satisfied by this equation. Substitution in the differential equation results in

$$\epsilon = \frac{\bar{r}_b}{\alpha_c}, \tag{A.27}$$

and λ satisfying the equation

$$\lambda(\lambda - 1) = i \frac{\omega \alpha_c}{\bar{r}_b^2} = i\,\Omega, \tag{A.28}$$

where Ω is the nondimensional circular frequency. Solution of the fluctuating radiation part, equation (A.21), is performed in an analogous way to the steady-state radiation part. Substitution of

$$T_r'(x) = a\left(e^{\alpha x} - e^{\beta x}\right) \tag{A.29}$$

in equation (A.21) yields

$$T_r'(x) = \frac{N_t I_0'}{\rho_c c_c \bar{r}_b \left(l_r - 1 - \frac{i}{\bar{r}_b} \frac{\omega}{\bar{\bar{a}}_\lambda}\right)} \left(\frac{l_r}{\lambda} e^{\lambda \bar{r}_b x / \alpha_c} - e^{\bar{\bar{a}}_\lambda x}\right), \tag{A.30}$$

where $l_r = \bar{\bar{a}}_\lambda \alpha_c / \bar{r}_b$, the ratio of thermal to radiant layer thickness. From the equations (A.26) and (A.30) the transient part of the temperature profile is known

$$T'(x) = T_{x=0,c}'(t) e^{\lambda \bar{r}_b x / \alpha_c} + \frac{N_t I_0'}{\rho_c c_c \bar{r}_b \left(l_r - 1 - \frac{i}{\bar{r}_b} \frac{\omega}{\bar{\bar{a}}_\lambda}\right)} \left(\frac{l_r}{\lambda} e^{\lambda \bar{r}_b x / \alpha_c} - e^{\bar{\bar{a}}_\lambda x}\right). \tag{A.31}$$

From this equation the heat flux into the solid can be calculated. Because the surface fluctuates between $x = s^+$ and $x = s^-$, this flux is not calculated by the derivative at $x = 0$, but at $x = s$. The surface temperature fluctuation can be found by a Taylor expansion

$$T_s' = T'(x = 0^-) + s\left(\frac{d\bar{T}}{dx}\right)_{x=0^-} + O(s^2). \tag{A.32}$$

For small (linearized) variations, the terms of second order and higher can be neglected. The fluctuating part of the heat flux is then calculated as

$$k_c \left(\frac{dT'}{dx}\right)_s \simeq k_c \left(\frac{dT'}{dx}\right)_{x=0^-} + k_c s \left(\frac{d^2\bar{T}}{dx^2}\right)_{x=0^-} . \tag{A.33}$$

As for the temperature (see equation (A.32)), the value of I_0' at the surface can be approximated by a Taylor expansion

$$(I_0')_{x=s} \simeq I_0' + s \left(\frac{d\bar{I}_0}{dx}\right)_{x=0^-} . \tag{A.34}$$

The value of s is found from an continuity equation across the burning surface

$$\rho_c(\bar{r}_b - \dot{s}) = \rho_g(u_g - \dot{s}) \tag{A.35}$$

yielding

$$s = -\frac{1}{i\omega}\frac{m'}{\rho_c} , \tag{A.36}$$

where the term $\rho_g u_g$ has been neglected.

These equations, together with the steady and transient profiles, lead to

$$k_c \left(\frac{dT'}{dx}\right)_{s^-} = \bar{m} c_c \lambda T_s' + \frac{m'}{\bar{m}}\left[\frac{\bar{m} c_c(\bar{T}_s - T_0)}{\lambda}\right] - \frac{m'}{\bar{m}}\left[N_t \bar{I}_0 \frac{1-\lambda}{\lambda(1-\lambda-l_r)}\right] + \frac{I_0'}{\bar{I}_0}\left[\frac{N_t \bar{I}_0 l_r}{1-\lambda-l_r}\right] . \tag{A.37}$$

A.3 Derivation of the linearized pyrolysis laws.

The Arrhenius pyrolysis law is given by

$$m_s = A T_s^{\alpha_s} p^{n_s} \exp\left[-\frac{\tilde{E}_s}{R T_s}\right] . \tag{A.38}$$

No pressure dependent pyrolysis has experimentally been observed, so n_s is set to zero. Note that the assumption of $n_s = 0$ does not imply that the pressure exponent $n = 0$. The steady-state burning rate $\bar{r}_b = a p^n$ is hidden in this equation, because of the relation $T_s = T_s(p)$. In figure 6.5 the two relations $\bar{r}_b(p)$, and $r_b(p) = f(T_s(p))$ are compared. Differentiating with respect to T_s yields

$$\frac{\partial m_s}{\partial T_s} = \frac{m_s\left(\alpha_s + \dfrac{\tilde{E}_s}{R T_s}\right)}{T_s} . \tag{A.39}$$

With the definition $E_s = \alpha_s + \tilde{E}_s/RT_s$ this can be rewritten to give

$$\frac{T_s'}{\bar{T}_s} = \frac{1}{E_s} \cdot \frac{m_s'}{\bar{m}_s} = \frac{1}{E_s} \cdot \frac{r_b'}{\bar{r}_b} \,. \tag{A.40}$$

The KTSS pyrolysis law given by

$$m_s = BT_s^{\alpha_s} p^{n_s} (T_s - T_0)^{w_s} \,. \tag{A.41}$$

With the same assumption $n_s = 0$, and further $\alpha_s = 0$, as suggested by DeLuca [19], it can be derived in an analogous manner that

$$\frac{T_s'}{\bar{T}_s} = \frac{\bar{T}_s - T_0}{T_0} \cdot \frac{m_s'}{\bar{m}_s}. \tag{A.42}$$

A.4 Derivation of the static restoring function.

Define the temperature disturbance profile, u, propagating inside the condensed phase after a perturbation at the burning surface, as

$$u(X,\tau) \equiv \Theta(X,\tau) - \bar{\Theta}(X) \,. \tag{A.43}$$

Assume that within a perturbed thermal layer of thickness $\xi(\tau)$, the temperature disturbance can be separated into a space dependent and time dependent part, and can be expressed as:

$$u(X,\tau) = u_s(\tau) \cdot u_c(X/\xi), \qquad 0 \le |X| \le \xi(\tau) \,, \tag{A.44}$$

where u_s is left unknown, and u_c is approximated by

$$u_c(X/\xi) \equiv (1 + X/\xi)^n \,, \tag{A.45}$$

or

$$u_c(X/\xi) \equiv e^{nX/\xi} \,. \tag{A.46}$$

Both forms describe the monotonic decay in space of the disturbance. At the burning surface $u_c(0) = 1$, and at the end of the disturbance layer $u_c(-1) = 0$ for the polynomial profile, or $\simeq 0$ for the exponential profile if n large.

Differentiating equation (A.44) with respect to X yields the disturbance thickness as function of time

$$\xi(\tau) = n \frac{u_s}{(u_x)_{c,s}} \,, \tag{A.47}$$

where $(u_x)_{c,s} = (\partial u/\partial X)_{c,s}$, the disturbance gradient at the surface.

This disturbance thermal gradient can be evaluated as

$$(u_x)_{c,s} \equiv \left(\frac{\partial \Theta}{\partial X}\right)_{c,s} - \left(\frac{d\bar{\Theta}}{dX}\right)_{c,s} = \frac{q_{c,s}}{K_c(\Theta_s)} - \frac{\bar{q}_{c,s}}{K_c(\bar{\Theta}_s)} \,. \tag{A.48}$$

With the energy conservation at the surface (equation (3.6)), and the first integral of the energy equation this can be rewritten to give

$$(u_x)_{c,s} = \frac{q_{g,s} + RH_s - q_{out}}{K_c(\Theta_s)} - \frac{\bar{R}\int_{\Theta_a}^{\bar{\Theta}_s} C_c(\Theta)d\Theta - \bar{F}_0 - \bar{R}\Sigma H_c}{K_c(\bar{\Theta}_s)} . \tag{A.49}$$

Using the equation (A.43) and integrating the energy equation (3.3) over the perturbed thermal layer ($-\xi \leq X < 0$) it is found that

$$\int_{-\xi}^{0^-} C_c(\Theta)\frac{\partial u(X,\tau)}{\partial \tau}dX = -R(\tau)\int_{\Theta_\xi}^{\Theta_s} C_c(\Theta)d\Theta + \left[K_c(\Theta)\frac{\partial \Theta}{\partial X}\right]_{c,s}$$

$$- \left[K_c(\Theta)\frac{\partial \Theta}{\partial X}\right]_{-\xi} + \int_{-\xi}^{0^-} F_0 f(X)dX + \int_{-\xi}^{0^-} \epsilon_c H_c dX . \tag{A.50}$$

By integrating over the disturbed layer the PDE is reduce to an ODE in time. At the edge of the perturbed thermal layer $\Theta(X,\tau) \simeq \bar{\Theta}(X)$, because $u_c(-1) \simeq 0$. Using the equations (3.6) and (A.44) it is found that

$$\int_{-\xi}^{0^-} C_c(\Theta)\left[\frac{du_s(\tau)}{d\tau}u_c(X/\xi) + u_s(\tau)\frac{du_c(X/\xi)}{d\tau}\right]dX$$

$$= -R(\tau)\int_{\Theta_\xi}^{\Theta_s} C_c(\Theta)d\Theta + q_{g,s} + R(\tau)H_s - q_{out} - \left[K_c(\Theta)\frac{d\bar{\Theta}}{dX}\right]_{-\xi}$$

$$+ \int_{-\xi}^{0^-} F_0 f(X)dX + \int_{-\xi}^{0^-} \epsilon_c H_c dX \tag{A.51}$$

Rewrite the space integration as

$$\int_{-\xi(\tau)}^{0^-} \ldots dX \equiv \int_{-\infty}^{0^-} \ldots dX - \int_{-\infty}^{\xi(\tau)} \ldots dX , \tag{A.52}$$

and use the first energy integral of the steady-state energy equations, to find

$$\int_{-\xi}^{0^-} C_c(\Theta)\left[\frac{du_s(\tau)}{d\tau}u_c(X/\xi)+u_s(\tau)\frac{u_c(X/\xi)}{G_1}\left(-\frac{nX}{\xi^2(\tau)}\right)\frac{d}{d\tau}\left(\frac{nu_s}{(u_x)_{c,s}}\right)\right]dX$$

$$=-R(\tau)\int_{\Theta_a}^{\Theta_s} C_c(\Theta)d\Theta+R(\tau)\int_{\Theta_a}^{\Theta_\xi} C_c(\Theta)d\Theta-\bar{R}\int_{\Theta_a}^{\Theta_\xi} C_c(\Theta)d\Theta+q_{g,s}+R(\tau)H_s+F_0$$

$$-q_{out}+R(\tau)H_c+A_cH_c\int_{-\xi}^{0^-}\left\{\exp(-E_c/\Upsilon(X))-\exp(-E_c/\bar{\Upsilon}(X))\right\}dX\ , \qquad \text{(A.53)}$$

where the function G_1 is defined as

$$G_1=\begin{cases}(1+X/\xi) & \text{for polynomial disturbance}\\ 1 & \text{for exponential disturbance, and n large enough}\end{cases} \qquad \text{(A.54)}$$

The most influential term is the surface thermal gradient disturbance at the surface side, $(u_x)_{c,s}$, defined by equation (A.48). In general, this term depends on the momentary values of surface temperature, pressure, and other time dependent parameter possibly affecting the surface boundary condition. Thus, for common situations its time derivative can be written as

$$\frac{d(u_x)_{c,s}}{d\tau}=\frac{du_s(\tau)}{d\tau}\left[\frac{\partial(u_x)_{c,s}}{\partial u_s}\right]_P+\frac{dP(\tau)}{d\tau}\left[\frac{\partial(u_x)_{c,s}}{\partial P}\right]_{u_s}. \qquad \text{(A.55)}$$

Static burning stability.

Static burning stability implies that the operating conditions are maintained constant in time. Under these circumstances equation (A.55) becomes

$$\frac{d(u_x)_{c,s}}{d\tau}=\frac{du_s(\tau)}{d\tau}\left[\frac{\partial(u_x)_{c,s}}{\partial u_s}\right]_P. \qquad \text{(A.56)}$$

For the static situation the following term of equation (A.53) becomes

$$u_s(\tau)\frac{u_c(X/\xi)}{G_1}\left(-\frac{nX}{\xi^2(\tau)}\right)\frac{d}{d\tau}\left(\frac{nu_s}{(u_x)_{c,s}}\right)=-\frac{du_s(\tau)}{d\tau}u_c(X/\xi)\frac{X}{G_1}\left[\frac{(u_x)_{c,s}}{u_s}-\left(\frac{\partial(u_x)_{c,s}}{\partial u_s}\right)_P\right]. \qquad \text{(A.57)}$$

For monotonic propagation in time of the disturbance layer thickness $\xi(\tau)$, the following ODE is found for the surface temperature [1]

[1] From the equations (A.43) and (A.44) it is found that

$$\frac{du_s(\tau)}{d\tau}=\frac{d\Theta_s(\tau)}{d\tau}.$$

$$\frac{d\Theta_s(\tau)}{d\tau} = f(\Theta_s - \bar{\Theta}_s) =$$

$$\left(\int_{-\xi}^{0^-} C_c(\Theta) u_c(X/\xi(\tau)) \left\{ 1 - \frac{X}{G_1} \left[\frac{(u_x)_{c,s}}{\Theta_s - \bar{\Theta}_s} - \left(\frac{\partial (u_x)_{c,s}}{\partial(\Theta_s - \bar{\Theta}_s)} \right)_P \right] \right\} dX \right)^{-1} \times$$

$$\times \left[-R(\tau) \int_{\Theta_a}^{\Theta_s} C_c(\Theta) d\Theta + (R - \bar{R}) \int_{\Theta_a}^{\Theta_\xi} C_c(\Theta) d\Theta + q_{g,s} + R(H_s + \Sigma H_c) + \right.$$

$$\left. F_0 - q_{out} + A_c H_c \int_{-\xi}^{0^-} \left\{ \exp(-E_c/\Upsilon(X)) - \exp(-E_c/\bar{\Upsilon}(X)) \right\} dX \right] . \qquad \text{(A.58)}$$

This ODE defines the static restoring function $f(\Theta_s - \bar{\Theta}_s)$. The initial condition is given by

$$\Theta_s(\tau = 0) = \bar{\Theta}_s . \qquad \text{(A.59)}$$

Dynamic burning stability.

For the second part of equation (A.55) can be treated in an analogous way to obtain an expression of the form

$$\frac{d\Theta_s(\tau)}{d\tau} = g(\tau, \Theta_s - \bar{\Theta}_s) . \qquad \text{(A.60)}$$

This equation defines the dynamic restoring function $g(\tau, \Theta_s - \bar{\Theta}_s)$. Note that this equation is time dependent whereas the static restoring function is time independent.

Appendix B

Numerical methods.

B.1 Finite-differences approximation of the condensed phase energy equation.

The finite-differences approximation of the condensed phase energy equation can be written as (see equation (6.16))

$$-A_j\Theta_{j+1}^{n+1} + B_j\Theta_j^{n+1} - C_j\Theta_{j-1}^{n+1} = D_j \ , \tag{B.1}$$

where the coefficients A_j, B_j, C_j, and D_j are defined as

$$A_j = -\frac{C_c(\Theta_j^k)}{8\Delta\tau} + \frac{\beta^2}{(\Delta X)^2}(X_j+1)(X_{j+1/2}+1)K_c(\Theta_{j+1/2}^k) \ , \tag{B.2}$$

$$B_j = \frac{5}{4\Delta\tau}C_c(\Theta_j^k) - \frac{\beta}{\Delta X}R(P^{n+1},\Upsilon_s^k)(X_j+1)C_c(\Theta_j^k) + \frac{\beta^2}{(\Delta X)^2}\cdot$$
$$\cdot\ (X_j+1)\left[(X_{j-1/2}+1)K_c(\Theta_{j-1/2}^k) + (X_{j+1/2}+1)K_c(\Theta_{j+1/2}^k)\right] \ , \tag{B.3}$$

$$C_j = -\frac{1}{8\Delta\tau}C_c(\Theta_j^k) - \frac{\beta}{\Delta X}R(P^{n+1},\Upsilon_s^k)(X_j+1)C_c(\Theta_{j-1/2}^k)$$
$$+\ \frac{\beta^2}{(\Delta X)^2}(X_j+1)(X_{j-1/2}+1)K_c(\Theta_{j-1/2}^k) \ , \tag{B.4}$$

$$D_j = \frac{C_c(\Theta_j^k)}{\Delta\tau}\left[\frac{1}{12}(2\Theta_{j+1}^n - \frac{1}{2}\Theta_{j+1}^{n-1}) + \frac{5}{6}(2\Theta_j^n - \frac{1}{2}\Theta_j^n)\right.$$
$$\left.+\ \frac{1}{12}(2\Theta_{j-1}^n - \frac{1}{2}\Theta_{j-1}^{n-1})\right] + \frac{1-\bar{\bar{r}}_\lambda}{\delta_a}F_0^{n+1}(X_j+1)^{1/(\beta\delta_a)} + H_c\epsilon_c(\Theta_j^k) \ . \tag{B.5}$$

B.2 Thomas algorithm.

Applying finite difference methods to a partial differential equation yields a set of simultaneous equations for every timestep. For most problems these equations are linear. If

the system of equations to be solved is very large, the matrix inversion method may use excessive computer time. A number of explicit finite difference methods, e.g. the Crank-Nicolson method, yield a *tridiagonal* matrix to be solved. These systems can be solved efficiently, with the Thomas algorithm (see e.g. [1]).

Consider the following tridiagonal system of n equations

$$\begin{pmatrix} b_1 & c_1 & & & & \\ a_2 & b_2 & c_2 & & & \\ & a_3 & b_3 & c_3 & & \\ & & \ddots & \ddots & \ddots & \\ & & & a_{n-1} & b_{n-1} & c_{n-1} \\ & & & & a_n & b_n \end{pmatrix} \cdot \begin{pmatrix} u_1 \\ u_2 \\ u_3 \\ \vdots \\ u_{n-1} \\ u_n \end{pmatrix} = \begin{pmatrix} d_1 \\ d_2 \\ d_3 \\ \vdots \\ d_{n-1} \\ d_n \end{pmatrix} . \tag{B.6}$$

Successive subtraction of a suitable multiple of each equation from the preceding equation, transforms the system into a simpler one of *upper diagonal* form

$$\begin{pmatrix} 1 & c'_1 & & & & \\ & 1 & c'_2 & & & \\ & & 1 & c'_3 & & \\ & & & \ddots & \ddots & \\ & & & & 1 & c'_{n-1} \\ & & & & & 1 \end{pmatrix} \cdot \begin{pmatrix} u_1 \\ u_2 \\ u_3 \\ \vdots \\ u_{n-1} \\ u_n \end{pmatrix} = \begin{pmatrix} d'_1 \\ d'_2 \\ d'_3 \\ \vdots \\ d'_{n-1} \\ d'_n \end{pmatrix} , \tag{B.7}$$

where the coefficients c'_i, and d'_i are calculated from the relations

$$c'_1 = \frac{c_1}{b_1} , \qquad d'_1 = \frac{d_1}{b_1} , \tag{B.8}$$

$$\left.\begin{aligned} c'_{i+1} &= \frac{c_{i+1}}{b_{i+1} - a_{i+1}c'_i} \\ d'_{i+1} &= \frac{d_{i+1} - a_{i+1}c'_i}{b_{i+1} - a_{i+1}c'_i} \end{aligned}\right\} \quad i = 1, 2, \ldots, n-1 , \tag{B.9}$$

and, of course $c'_n = 0$.

From this u_n is directly known, $u_n = d'_n$. Using the special form of the upper diagonal matrix it is easily seen that all other values of u_n can be calculated successively from

$$u_i = d'_i - c'_i u_{i+1}, \qquad i = (n-1), (n-2), \ldots, 1 . \tag{B.10}$$

Note that computing time is short because no iteration is necessary. The memory used by the sparse matrix of equation (B.6) can be reduced by only storing the coefficients unequal to zero.

Appendix C

The Zeldovich-Novozhilov approach.

Although transient burning calculations within the flame approach are the subject of this report, the Zeldovich-approach is also shortly discussed in this appendix to be complete. The flame description approach, as discussed in the previous chapter, requires detailed knowledge of the heat release in the gas phase, in order to calculate the heat feedback from the gas phase to the condensed phase. Within the Zeldovich-Novozhilov (ZN) approach this feedback is calculated from experimental steady-state burning rate data, surface temperature, pressure, and initial propellant temperature. The assumptions made in this approach are similar to those of flame modeling approaches.

In the ZN-approach, it is assumed that the burning rate (r_b) depends on pressure (p), flame temperature (T_f), and the temperature gradient at the solid-gas interface ($\Phi_{g,s} = \partial T/\partial x$)

$$r_b = r_b(p, T_f, \Phi_{g,s}) \ . \tag{C.1}$$

The energy balance yields

$$r_b = r_b(\Phi_{c,s}, \Phi_{g,s}, Q_s) \ . \tag{C.2}$$

It is further assumed that the pyrolysis law, and the heat release at the surface are described by the following functional relations

$$r_b = r_b(T_s, p) \ , \tag{C.3}$$

and

$$Q_s = Q_s(T_s, p) \ . \tag{C.4}$$

An energy balance over a control volume on the surface yields

$$r_b \rho_c h_{c,s}(T_s) = r_b \rho_c h_{g,f}(T_f, p) + k_c \Phi_{c,s} \ , \tag{C.5}$$

where $h_{c,s}$ and $h_{g,f}$ the enthalpy in the condensed phase respectively in the gaseous phase.

The equations (C.1)-(C.5) form a system of five equations in seven unknowns (r_b, Q_s, $\Phi_{g,s}$, $\Phi_{g,s}$, T_f, T_s, and p). After eliminating four unknowns from the five equations, one obtains a single equation in three unknowns

$$\Phi_{c,s} = \Phi_{c,s}(r_b, p) \ . \tag{C.6}$$

If the gas phase and the surface reactions are considered quasi-steady, while the condensed phase is treated as a transient process, then this equation can be extended to transient burning to obtain

$$\Phi_{c,s}(t) = \Phi_{g,s}\left(r_b(t), p(t)\right) \ . \tag{C.7}$$

From experimental data the following relationships are known

$$\bar{r}_b = \bar{r}_b(T_a, \bar{p}) \tag{C.8}$$

$$\bar{T}_{s,0} = \bar{T}_s(p, \bar{r}_b) \ . \tag{C.9}$$

The steady-state solid-phase energy balance is written as

$$K_c \Phi_{c,s} = \bar{r}_b \rho_c \int_{T_a}^{\bar{T}_s} c_c(T) dT \ . \tag{C.10}$$

Using equations (C.6)-(C.10) it is possible to construct the *Zeldovich map*. If the propellant initial temperature, chamber pressure, and instantaneous burning rate are known, $\Phi_{c,s}$ can be determined . This quantity is needed to specify the boundary condition at the solid-gas interface for the transient solid phase energy equation. Since the burning rate appears also as a coefficient in the energy equation, the solution is iterative. Radiation absorption can be modelled by use of the *equivalence principle* [30]. This principle states that there is an equivalence between radiant flux and an increased propellant temperature,

$$r_b(p, T_a, I_0) = r_b(p, T_a + I_0/(\rho r_b c_c), 0) \ , \tag{C.11}$$

where I_0 the external energy flux.

The ZN-method is reliable only when accurate steady state burning data is available. If this is not the case, than the flame description is more accurate.

Appendix D

Thermophysical properties of AP-composites.

In this section an overview is given of measurements of thermodynamic properties and burning characteristics of AP-composites. As reference a nonaluminized composite propellant containing 86% AP and 14% HTPB is chosen ("AP1" from reference [57]). First the properties of pure AP are discussed, and hereafter the propellant properties are reviewed.

D.1 Thermophysical properties of AP.

Ammonium perchlorate is an inorganic salt commonly used as an oxidizer in composite propellants. As monopropellant is has been studied over a large temperature and pressure range. A recent review of AP monopropellant combustion is reported in reference [57].

AP features two crystalline phases in the temperature range of ballistic interest, orthorombic in the range of 83 – 513 K, and cubic above 513 K (although 516 K has also been reported, see e.g. reference [8]). As reported by Guirao and Williams [28] this transition is endothermic requiring 21.3 cal/g (89.1 J/g).

The melting temperature of AP is 723 K. As this temperature lies below typical surface temperatures for composite propellants, it becomes clear that this phase transition is also important for describing the condensed phase accurately. As the crystallographic transition, this transition is also endothermic, with a latent heat of 59.6 cal/g (249 J/g) [28].

During phase transitions the densities change from 1.957 g/cm^3 in the orthorombic state, to 1.756 g/cm^3 in the cubic state, and 1.710 g/cm^3 in the liquid phase.

The specific heat, thermal diffusivity and thermal conductivity of AP-crystals are strongly temperature dependent. These properties are not discussed for pure AP, but only for the complete propellant (see next section). For details consult references [28], [46], and [57].

D.2 Thermophysical properties of HTPB.

Hydroxyl terminated polybutadiene (HTPB) is the traditional binder used in composite rocket propellants. This rubbery organic material serves as a fuel and is oxidized by the oxygen released during the decomposition of AP.

HTPB is an amorphous polymer. In contrast with the crystalline polymers, the amorphous polymers do not exhibit discontinuities in their thermophysical properties. The discontinuities in the thermal properties of AP-HTPB propellants come from the AP, and not from the HTPB. Typical for amorphous polymers is the linearly dependency of the specific heat on the temperature. This is confirmed by the measurements for HTPB. See reference [57] for a summary of these measurements.

D.3 Thermophysical properties of an AP/HTPB propellant.

Define T_{tra} as the temperature at which crystallographic transition occurs (513 K), and T_m as the melting temperature of AP (723 K).

As said before, the density of AP is dependent on its phase. Due to these differences, the density of the propellant (containing AP) also changes during phase transitions. For the current propellant this can be summarized as

$$\rho_c(T) = \begin{cases} 1.630 \text{ g/cm}^3 & \text{for } T < T_{tra} \\ 1.506 \text{ g/cm}^3 & \text{for } T > T_{tra}\,. \end{cases} \tag{D.1}$$

The thermal diffusity is controlled mainly by the presence of AP. When AP is orthorombic, the average thermal diffusivity is slightly below that of pure AP. When AP is cubic or liquid, the thermal diffusivity is much lower and reproduces that of cubic AP. The thermal diffusivity can be written as

$$\alpha_c(T) = \begin{cases} 1.84 - 10^{-3} \text{ cm}^2/\text{s} & \text{for } T < T_{tra} \\ 0.53 - 10^{-3} \text{ cm}^2/\text{s} & \text{for } T > T_{tra}\,. \end{cases} \tag{D.2}$$

The specific heat of the condensed phase is given by (in cal/gK)

$$c_c(T) = \begin{cases} 0.289 + 0.469 - 10^{-3}(T - 300) & \text{for } T < T_m \\ 0.381 & \text{for } T > T_m\,. \end{cases} \tag{D.3}$$

This equation is summarized in figure D.1.

The thermal conductivity can be computed from the above properties and is given by (in cal/cm s K)

$$k_c(T) = \begin{cases} 8.67 \text{-}10^{-4} + 1.41 - 10^{-6}(T - 300) & \text{for } T < T_{tra} \\ 2.31 \text{-}10^{-4} + 3.74 - 10^{-7}(T - 300) & \text{for } T_{tra} < T < T_m \\ 3.04 \text{-}10^{-4} & \text{for } T_m < T\,, \end{cases} \tag{D.4}$$

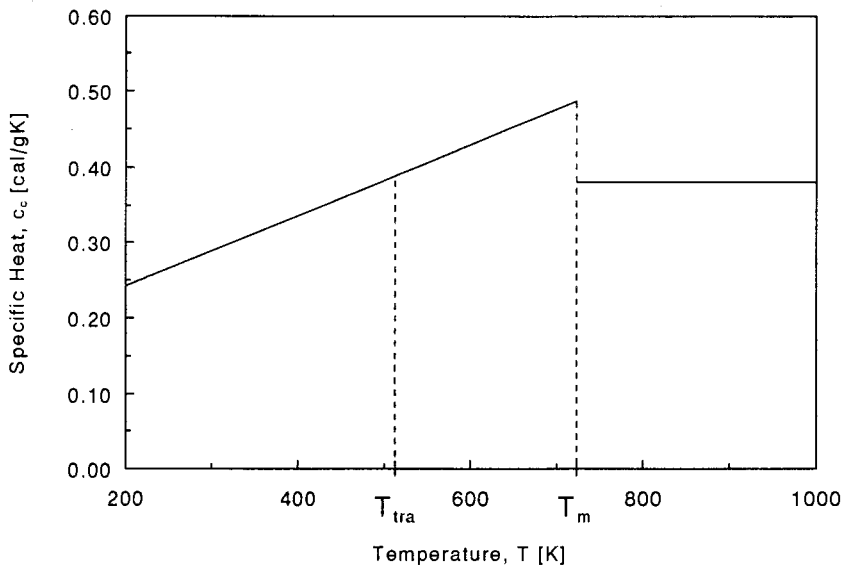

Figure D.1: Specific heat of an AP/HTPB:86/14 propellant as function of the temperature.

see figure D.2. Note the large dependence of k_c on temperature, causing a factor 3 difference between maximum and minimum thermal conductivity.

Table D.1 shows the propellants properties as used in the calculations, unless noted otherwise. The adiabatic flame temperature, T_f, is calculated with the NASA SP-273 code [26], assuming a temperature efficiency of 95%.

	Symbol	Value	Unit	Reference
AP weight fraction		86	%	
AP crystalline transition temperature	T_{tra}	513	K	[57]
AP crystal transition heat	Q_{tra}	-21.3	cal/g	[28]
AP melting temperature	T_m	723	K	[57]
AP melting heat	Q_m	-59.6	cal/g	[28]
AP decomposition heat	Q_{dec}	800	cal/g	[16]
AP vaporization heat	$Q_{vap,AP}$	-493	cal/g	[28]
HTPB weight fraction		14	%	
HTPB vaporization heat	$Q_{vap,HTPB}$	-430	cal/g	[38]
Condensed density	ρ_c	1.630	g/cm^3	[57]
Condensed specific heat	$c_c(T)$	eq. (D.3)	cal/g K	[57]
Condensed thermal conductivity	$k_c(T)$	eq. (D.4)	cal/cm s K	[57]
Condensed thermal diffusivity	$\alpha_c(T)$	eq. (D.2)	cm^2/s	[57]
Gas specific heat	$c_g(T)$	0.33	cal/g K	[18]
Gas thermal conductivity	$k_g(T)$	$2.0 \cdot 10^{-4}$	cal/cm s K	[18]
$\alpha\beta\gamma$-flame model parameters	$\alpha(p)$	$0 \ldots 1$	-	
	$\beta(p)$	$0 \ldots 1$	-	
	$\gamma(p)$	$0, 1, 2, 3, \ldots$	-	
Surface pyrolysis pressure exponent	n_s	0	-	
Surface pyrolysis activation energy	$\tilde{E}_s$	21000	cal/mole	[57]
Initial sample temperature	T_a	300	K	
Steady-state burning rate	$\bar{r}_b$	$1.074 \cdot (p/p_{ref})^{0.53}$	cm/s	[57]
Steady-state surface temperature	$\bar{T}_s$	$945.2 \cdot (p/p_{ref})^{0.045}$	K	[57]
Adiabatic flame temperature	$\bar{T}_f$	$2763 \cdot (p/p_{ref})^{0.019}$	K	SP-273
Steady-state surface heat release	$\bar{Q}_s$	$96.5 \cdot (p/p_{ref})^{0.049}$	cal/g	[25]
Condensed phase	$\bar{Q}_c$	0	cal/g	
Reference Properties				
Pressure	p_{ref}	68	atm	
Temperature	T_{ref}	300	K	
Length	x_{ref}	$17.14 \cdot 10^{-4}$	cm	
Time	t_{ref}	$15.96 \cdot 10^{-4}$	s	
Heat	Q_{ref}	186.5	cal/g	
External radiation	I_{ref}	326.4	cal/cm^{2}s	

Table D.1: Properties of the AP:HTPB 86:14 propellant used as reference propellant. All heat releases positive if exothermic.

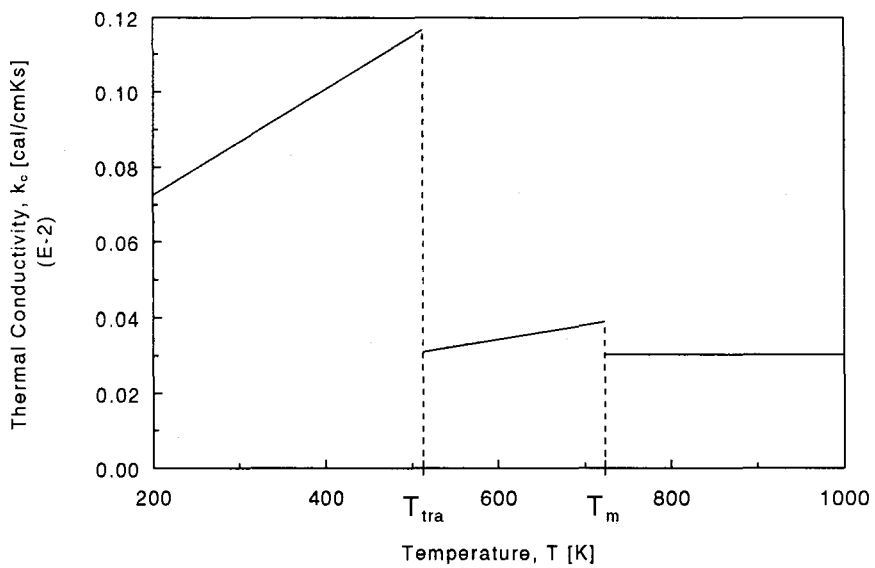

Figure D.2: Thermal conductivity of an AP/HTPB:86/14 propellant as function of the temperature.

Appendix E

HNF-GAP propellants.

E.1 Properties of HNF-GAP propellants.

E.1.1 Properties of HNF.

Hydrazinium NitroFormate (HNF) is a potential high performance chlorine free oxidizer for future solid propellants. Until the renewed interest for this oxidizer only a few studies existed. Thermophysical properties are hardly found in the open literature.

Von Elbe et al. found a thermal diffusivity of $\alpha_c \sim 0.001$ cm^2/s, by a fitting procedure on the thermal profiles as obtained by micro-thermocouple measurements in the condensed phase [23]. The density is not accurately known, measurements at PML-TNO gave a density of 1.91 g/cm^3, which is within the literature data [49]. The condensed specific heat is estimated as $c_c = 0.3$ cal/g, and the thermal conductivity is set at $k_c = 1 \cdot 10^{-4}$ cal/cm s K (in agreement with the thermal diffusivity).

The melting point of HNF is related to its purity. A representative value for the melting point of HNF is 396 K (123°C). At this temperature HNF decomposes.

E.1.2 Properties of GAP.

Glycidyl Azide Polymer (GAP) is an energetic material which produces heat by decomposition, because of the azide groups (N_3) in its structure. It is expected that GAP in combination with HNF, produces a reduced smoke, high performance propellant. Recently is has been tested with existing oxidizers such as ammonium nitrate and ammonium perchlorate as substitute for the less energetic HTPB [48].

Because of the high heat release during scission of the $-N_3$ bond, GAP shows a self sustained combustion at pressures above 0.3 MPa [34]. This makes it an excellent candidate fuel for gas generators in ducted rockets. It is also possible to (partly) replace the common HTPB in hybrid rockets with GAP, to overcome the problem of low regression rates [38]. Owing to the great number of applications of GAP, a lot of effort is put in the research of its characteristics. Thermophysical properties are given by Kubota and Sonobe [34].

Measurements of the combustion zone of GAP show a condensed reaction zone, starting at a temperature of 600 K, and extending to the surface temperature of approximately 700 K. It was found that the condensed phase heat release in this reaction zone is Q_c = 149 cal/g [34].

E.1.3 Properties of HNF-GAP propellants.

Only little burn rate data is available for HNF-GAP propellants. The TNO/PML HGU-4-1 combination has been tested in a chimney burner. This propellant contains 47.5% HNF and 52.5% GAP by weight. The burning law was determined to be

$$r_b = 15.3 \cdot p^{0.751} \text{ mm/s} , \tag{E.1}$$

where p in MPa. It is seen that the burning exponent n and overall burning rate are large.

As mentioned before HNF starts to decompose at its melting point (396 K). Because of the low melting point, it is expected that the surface temperature of HNF-based propellants is much lower than that of AP composites. Assume that the surface temperature of the HGU-4-1 propellant is 550 K at reference properties. The high reactivity of HNF-based propellants will result in a high sensitivity of the burning rate on the surface temperature. This sensitivity is expressed by the surface activation energy $\tilde{E}_s$. For composite propellants this activation energy varies between 15 and 25 kcal/mole (63 and 105 KJ/mole). Based on these values, the surface activation energy is assumed to be $\tilde{E}_s$ = 30 kcal/mole.

By fitting the steady state temperature as function of the pressure is found from the steady state burning law[1]. Figure E.1 shows the surface temperature as function of the pressure. The relation between flame temperature and pressure is found from calculations with the NASA SP-273 code.

At reference conditions the energy necessary to heat up the propellant up to it's steady state temperature is calculated as

$$Q = c_c(T_{s,ref} - T_a) = 95 \text{ cal/g} . \tag{E.2}$$

Assume that 50% of this energy is released by condensed phase reactions and surface reactions, and the other 50% is conducted from the flame into the propellant. It is further assumed that all condensed phase reactions are collapsed to the surface, i.e. $Q_c = 0$.

Table E.1 summarizes the properties of HNF and GAP individually, and the HGU-4-1 propellant. The quantities marked with an asterix (*) are estimated because of the lack of experimental data.

[1]The nondimensional form of the steady state burning law is $R = (p/p_{ref})^n$. The nondimensional Arrhenius pyrolysis law is written as $R = \exp\left\{-\tilde{E}_s/\Re T_s(p)\right\} / \exp\left\{-\tilde{E}_s/\Re T_{s,ref})\right\}$. Equalization of these equations yields

$$T_s(p) = \frac{1}{\dfrac{1}{T_{s,ref}} - \dfrac{n\Re}{\tilde{E}_s}\ln(p/p_{ref})} .$$

This equation is then fitted to the common power relation $T_s(p) = T_{s,ref}(p/p_{ref})^{n_{T_s}}$.

	Symbol	Value	Unit	Reference
HNF weight fraction		47.5	%	
Condensed density of HNF	$\rho_{c,HNF}$	1.91	g/cm^3	[49]
Condensed specific heat of HNF	$c_{c,HNF}$	0.30	cal/gK	*
Condensed thermal conductivity of HNF	$k_{c,HNF}$	$1.0 \cdot 10^{-3}$	cal/cm s K	*
Condensed thermal diffusivity of HNF	$\alpha_{c,HNF}$	$\sim 1 \cdot 10^{-4}$	cm^2/s	[23]
Melting temperature of HNF	$T_{m,HNF}$	395	K	[49]
GAP weight fraction		52.5	%	
Condensed density of GAP	$\rho_{c,GAP}$	1.28	g/cm^3	[38]
GAP decomposition heat	$Q_{dec,GAP}$	150	cal/g	[38]
Condensed specific heat of GAP	$c_{c,GAP}$	0.45	cal/gK	
Condensed thermal conductivity of GAP	$k_{c,GAP}$	$3.5 \cdot 10^{-4}$	cal/cm s K	[38]
Condensed thermal diffusivity of GAP	$\alpha_{c,GAP}$	$6.1 \cdot 10^{-4}$	cm^2/s	[38]
Decomposition temperature of GAP	$T_{dec,GAP}$	$600 \sim 700$	K	[34]
Condensed density	ρ_c	1.52	g/cm^3	[49]
Condensed specific heat	c_c	0.38	cal/g	*
Condensed thermal conductivity	k_c	$8.1 \cdot 10^{-4}$	cal/cm s K	*
Condensed thermal diffusivity	α_c	$1.4 \cdot 10^{-3}$	cm^2/s	*
Gas specific heat	c_g	0.46	cal/gK	SP-273
Gas thermal conductivity	k_g	$2.0 \cdot 10^{-4}$	cal/cm s K	*
$\alpha\beta\gamma$-flame model parameters	$\alpha(p)$	0	-	
	$\beta(p)$	1	-	
	$\gamma(p)$	0/1	-	
Surface pyrolysis pressure exponent	n_s	0	-	
Surface pyrolysis activation energy	$\tilde{E}_s$	30000	cal/mole	*
Initial sample temperature	T_a	300	K	
Steady-state burning rate	$\bar{r}_b$	$6.381 \cdot (p/p_{ref})^{0.751}$	cm/s	TNO/PML
Steady-state surface temperature	$\bar{T}_s$	$550 \cdot (p/p_{ref})^{0.026}$	K	*
Adiabatic flame temperature	$\bar{T}_f$	$2037 \cdot (p/p_{ref})^{0.00082}$	K	SP-273
Steady-state surface heat release	$\bar{Q}_s$	47.5	cal/g	*
Condensed phase	$\bar{Q}_c$	0		*
Reference Properties				
Pressure	p_{ref}	68	atm	
Temperature	T_{ref}	300	K	
Length	x_{ref}	$2.2 \cdot 10^{-4}$	cm	
Time	t_{ref}	$3.4 \cdot 10^{-5}$	s	
Heat	Q_{ref}	76	cal/g	
External radiation	I_{ref}	737	cal/cm^{2}s	

Table E.1: Properties of the HGU-4-1 (HNF:GAP 47.5:52.5) propellant.

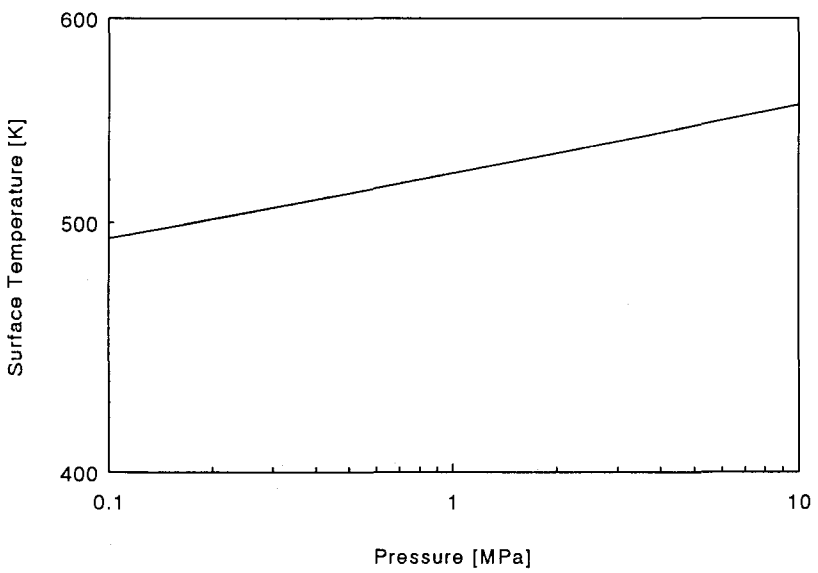

Figure E.1: Estimated surface temperature as function of the pressure for a HNF-GAP propellant.

E.2 Burning of HNF-GAP propellants.

E.2.1 Steady state burning.

The high regression rates and the expected low surface temperatures of HNF-based propellants result in temperature profiles which are very different from the profiles in AP-composites. Figure E.2 compares a typical profile of an AP-propellant (curve 1) with that of a HNF-GAP propellant (curve 2). The steep profile is a direct result from the high burn rates of the HNF propellant because of the factor $\bar{r}_b x/\alpha_c$ in the exponent of the analytical solution (see equation (A.14)).

E.2.2 Response functions.

With the data from table E.1 a response function calculation for the HGU-4-1 propellant was performed at pressure of 1.0 Mpa. Figure E.3 shows the results of these calculations, together with the response function of the AP reference propellant for comparison. It is seen that the propellant has its maximum response at a frequency of approximately 3000 Hz. This high resonance frequency can be attributed to the small thermal layer of HNF-propellants, which resonates at a high frequency of the disturbance signal. For low frequencies the thermal layer is burned away completely within less then one cycle. For example, at a frequency of 100 Hz, the propellant burns 150 μm in one cycle, which is much larger then the thermal layer thickness (see figure E.2).

From the linearized calculations of chapter 4 it is known that $R_p \sim n$ (see equa-

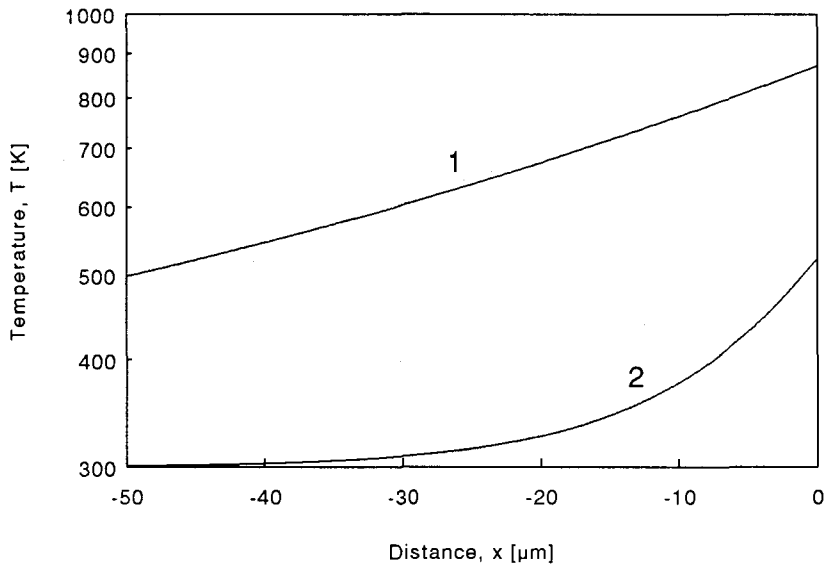

Figure E.2: Comparison of the temperature profile in the condensed phase of a typical AP-propellant (1) and a HNF-GAP propellant (2). Both calculations with constant thermal properities.

tion (4.15)), so the large instability of HNF based propellants (compared to the AP propellant) is not originated by the large value of n, because this would lead to a value which is only 50% higher. However, as also discussed for AP propellants the response function is very sensitive to the value of Q_s (and Q_c). Figure E.4 summarizes several response functions for different values of Q_s.

Due to the decomposition of GAP in the solid phase, the subsurface heat release of pure GAP is 149 cal/g (section E.1.2). If it is assumed that this process does not change because of the presence of HNF in the solid phase, the subsurface heat release due to HNF solely, is 78 cal/g. When this value is used in the calculations, it is evident from figure E.4 that a large intrinsic instability will be found. However, this high instability is far from practical. It can be concluded that the HNF/GAP propellant is insufficiently studied, and that the values of the different quantities are not known accurate enough. It is also important to know more about the chemical reaction zone, to be able to tell whether simplified analysis of an inert condensed phase and simple flame model are valid.

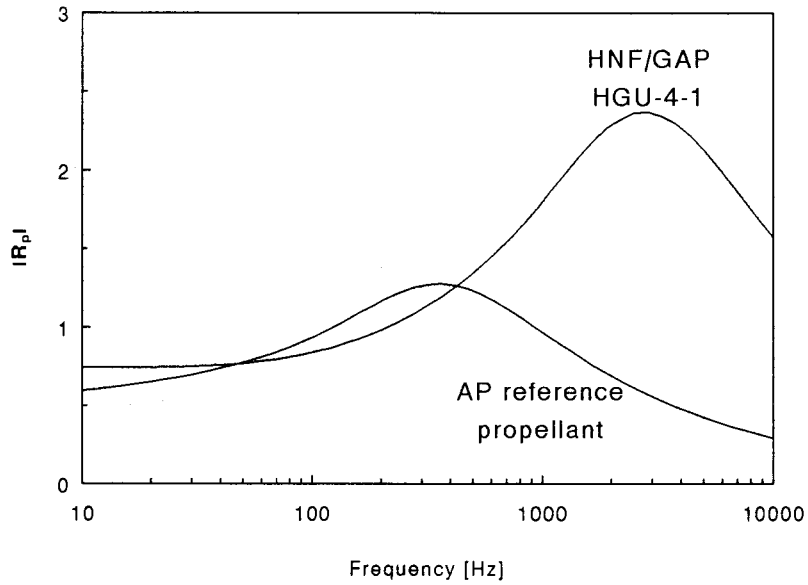

Figure E.3: Comparison of the pressure coupled response function of a HNF/GAP-propellant with that of the AP reference propellant.

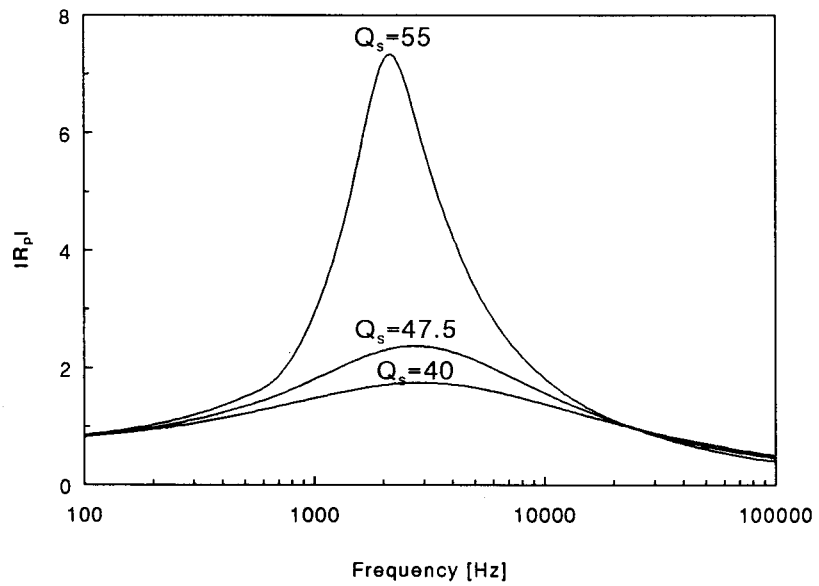

Figure E.4: Pressure coupled response function of a HNF/GAP-propellant for several values of the surface heat release.

Appendix F

TW95 Workshop.

Some parts of the work of this thesis were presented at the International Workshop TW95, "Chemical gasdynamics and combustion of energetic materials", held in Tomsk, Russia, June 26-29, 1995. The next pages show the poster (reduced size) and accompanying handout presented there.

Effect of solid phase reactions on the nonlinear transient burning of composite propellants

Jeroen Louwers, Guy M.H.J.L. Gadiot
TNO Prins Maurits Laboratory, P.O. Box 45, 2280 AA Rijswijk, The Netherlands
E-mail: gadiot@pml.tno.nl

Introduction

An extended model for the transient burning of AP-composites was developed. The model accounts for:

- temperature dependent thermal properties
- solid phase reactions
- the melting of AP and the crystalline transformation of orthorhombic to cubic AP.

The model is based on the flame description approach, with the following most important assumptions:

- quasi-steady gas phase, the heat feedback from the gaseous phase to the condensed phase ($q_{g,s}$) is calculated using the $\alpha\beta\gamma$-model with α=0, β=1, and γ=0,1,2,..
- homogeneous one-dimensional condensed phase.

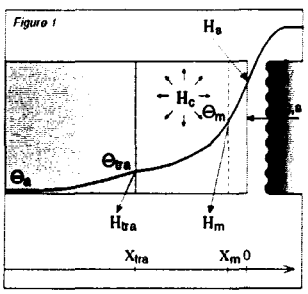

Figure 1 shows the model considered. Deep in the propellant solid phase, the propellant has its initial temperature Θ_s. Due to the conductive heating by the gas phase, and chemical reactions in the solid, the temperature in the solid increases. This process can be described by the following nondimensional parabolic partial differential equation: (1)

$$C_c(\Theta)\left[\frac{\partial\Theta}{\partial\tau}+R\frac{\partial\Theta}{\partial X}\right]=\frac{\partial}{\partial X}\left[K_c(\Theta)\frac{\partial\Theta}{\partial X}\right]+H_c e_c(\Theta),\ \text{for } -\infty<X<0$$

The equations are solved numerically by the use of an implicit finite difference method.

Object of this study is to analyze the effects of the processes in the condensed phase on the transient burning.

Results

Figure 2 shows the effect of several processes on the steady-state temperature profile in the condensed phase:

1. constant thermal properties (analytical solution of equation (1))
2. temperature dependent thermal properties
3. as 2, with latent heats of phase transitions.

From transient calculations the response function of the propellant can be calculated. The pressure driven response function is computed by perturbing the steady state with a sinusoidal fluctuating pressure, with an amplitude of 10% of it mean value. After a few cycles a situation of dynamic equilibrium develops. The relative change in burning rate, r_b, during this balance divided by the relative change in pressure defines the pressure coupled response function, according to: (2)

$$R_p=\frac{r_b'/r_b}{p'/p}$$

Figure 3 is an example of the calculation of the response on a 500 Hz sinusoidal disturbance, for three different distributions of the chemical reactions:

1. Reactions occurring at the surface
2. Reactions in the condensed phase, high activation energy, i.e. close to the surface
3. Reactions in the condensed phase, low activation energy, i.e. broad reaction zone.

Figure 4 shows the pressure coupled response function obtained for the complete frequency domain.

Figure 5 shows the transient results for first two situations of figure 2.

Figure 6 shows the effect of the crystallographic transition, and melting of AP.

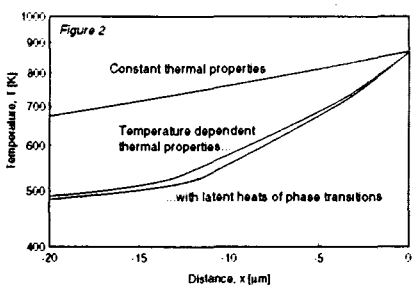

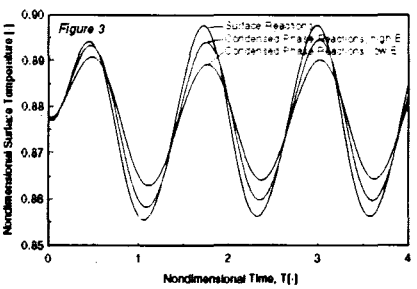

Conclusions

- Solid phase reactions have a similar effect on the transient burning as the surface heat release, however for condensed phase reactions the maximum of the response decreases, and shifts to lower frequencies, because the thermal layer thickness is enlarged (figure 4).

- The approximation of constant thermal properties is too crude to predict the response of a propellant accurately (figure 5).

- Phase changes in the condensed phase yields a more stable propellant, lowering the maximum of the response function and shifting it to higher frequencies (figure 6).

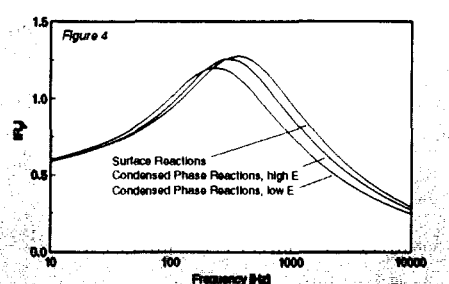

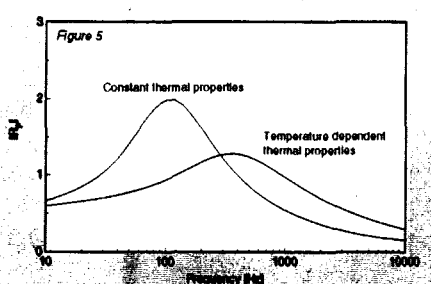

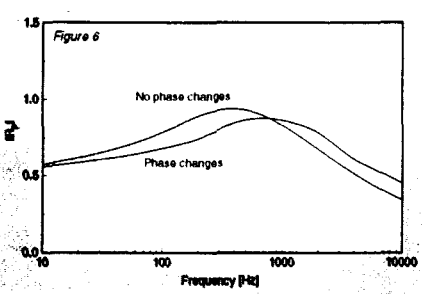

Effect of Solid Phase Reactions on the Nonlinear Transient Burning of Composite Propellants[1]

Jeroen Louwers, Guy M.H.J.L. Gadiot[2]
TNO Prins Maurits Laboratory, P.O. Box 45, 2280 AA Rijswijk, The Netherlands

The phenomenon of transient burning of solid propellants is a topic which still contains a large number of questions. In this paper the transient burning of AP composite propellants is calculated within the QSHOD approach (Quasi Steady gas phase, Homogeneous One-Dimensional condensed phase). This paper focuses on the effect of the condensed phase on the transient burning of solid propellants by showing the effect of temperature dependent thermal properties, phase transitions and chemical reactions in the solid phase. Nonlinear effects are conserved, as governing equations are solved numerically.

♦ Introduction

In the past a lot of effort has been put into the development of models for transient burning of solid propellants. With the exception of a few models, most models share the same basic assumptions, of which the most important are: homogeneous propellant, quasi-steady gas phase and neglect of solid phase reactions. Several researchers reported that the existing models could be improved by accounting for the chemical reactions in the solid phase, hence, an extended model for the solid phase of Ammonium Perchlorate (AP) composites was developed, within the flame description approach. This model accounts for the solid phase reactions, the melting of AP and the crystalline transformation of orthorhombic to cubic AP, the latter causes an abrupt change of thermal properties at the transitions.

♦ The model

Figure 1 shows the model considered. Deep in the propellant solid phase, the propellant has its initial temperature Θ_a. Due to the conductive heating by the gas phase, and chemical reactions in the solid, the temperature in the solid increases. This process can be described by the following nondimensional parabolic partial differential equation [1]:

$$C_c(\Theta)\left[\frac{\partial\Theta}{\partial\tau}+R\frac{\partial\Theta}{\partial X}\right] = \frac{\partial}{\partial X}\left[K_c(\Theta)\frac{\partial\Theta}{\partial X}\right] + H_c\varepsilon_c(\Theta) \quad , \quad \text{for } -\infty<X<0 \; . \tag{1}$$

C_c is the (temperature dependent) heat capacity of the condensed phase, K_c the thermal conductivity of the propellant, Θ is the temperature, R is the burning rate, τ and X are the time and space coordinate respectively, and $H_c\varepsilon_c(X)$ is the heat release distribution due to chemical reactions in the solid phase, which is assumed to be exponentially dependent on the

---

[1] Presented at the International Workshop - TW95, *Chemical Gasdynamics and Combustion of Energetic Materials,* June 26-29, 1995, Tomsk, Russia

[2] Corresponding author, E-mail: gadiot@pml.tno.nl

local temperature. (all nondimensional quantities). The sources of nonlinearity are $R\partial\Theta/\partial X$, and $H_c\varepsilon_c(\Theta)$. At the surface, heat is released which is described by the term H_s. This surface heat release can be seen as the total heat released in the condensed phase which is collapsed at the surface. This allows for simple calculations, because this term does not appear in the energy equation but in its boundary conditions.

During heating two phase transitions take place in the solid, the crystallographic transition (at $X=X_{tra}$) and the melting of AP (at $X=X_m$). These transitions require energy and act as heat sinks in the solid phase (H_{tra} and H_m respectively). Also the temperature dependence of the thermal conductivity and heat capacity are accounted for. The thermal conductivity of AP, e.g., is reduced by a factor of three during the transition from orthorhombic to cubic AP as illustrated by figure 2 [2]. The gas phase is considered to be quasi-steady, which holds for low frequencies and low pressure. The heat feedback from the gaseous phase to the condensed phase ($q_{g,s}$) is calculated using the $\alpha\beta\gamma$-model with $\alpha=0$, $\beta=1$, and $\gamma=0,1,2,...$ [1]. It is assumed further that this conductive heat transport is only pressure dependent. From these assumptions it becomes clear that the gas phase is modelled very crude, however, it is the objective of this study to analyze the effects of the processes in the condensed phase on the transient burning.

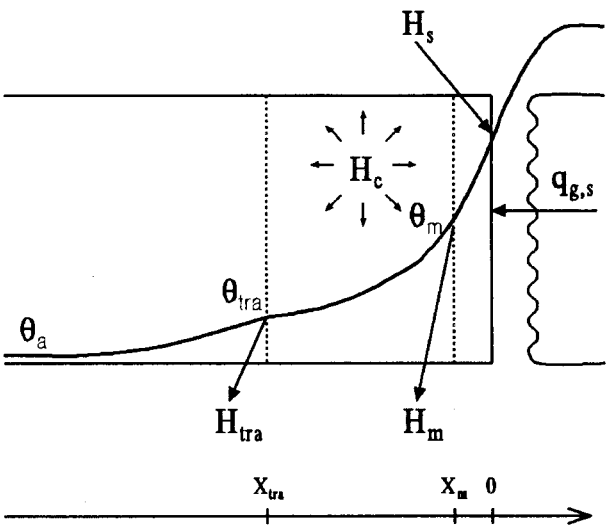

Figure 1 Schematic of the temperature distribution and physical processes in an AP propellant.

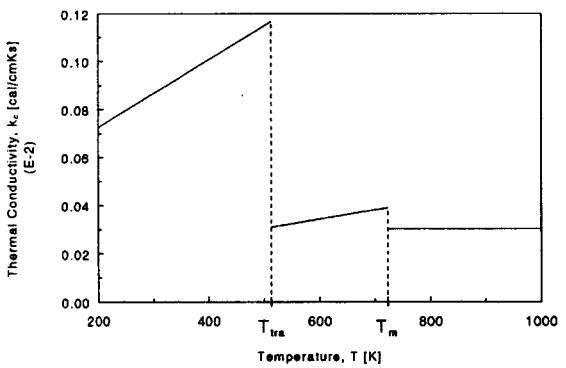

Figure 2 Thermal conductivity of a typical nonaluminized AP propellant.

The equations are solved numerically by the use of an implicit finite difference method. Unless noted otherwise, all calculations are performed at a pressure of 1.0 MPa. The temperature dependent thermal properties are obtained from Ref.[2].

♦ Steady State Burning

Because of the dependence of the thermophysical properties on the temperature, the temperature distribution in the condensed phase will be different from the analytical solution of Eq.(1) which holds for constant thermal properties (curves 1 and 2 of figure 3). When the latent heats are introduced the profile becomes steeper (curve 3), because of the condition

$$\left[K_c(\Theta)\frac{\partial\Theta}{\partial X}\right]_{X=X_{tra}^-} = \left[K_c(\Theta)\frac{\partial\Theta}{\partial X}\right]_{X=X_{tra}^+} + RH_{tra} \quad , \tag{2}$$

at the crystallographic transition point, and analogous at the melting point. Note that the melting heat of AP is not found in the open literature, and is approximated by that of potassium perchlorate [3].

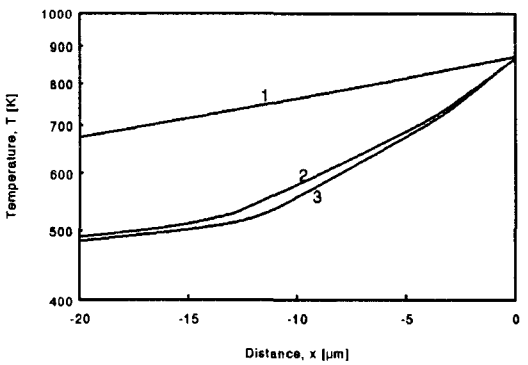

Figure 3 Analytical temperature distribution in the solid(1). Effect of temperature dependent thermophysical properties (2), and latent heats (3).

♦ Transient Burning

In order to be able to calculate the transient burning of a solid rocket propellant, it is necessary that the propellant parameters are known accurately. The value of the total heat released by chemical reactions (H_s+H_c) is a quantity which is difficult to measure. It was shown that the surface heat release H_s is a very sensitive quantity for steady state burning [4], as well as for transient burning for which this sensitivity can be shown easily by the linearized calculations of the response function [1]. Apart from the value of the total heat release in the condensed phase, the distribution of this release is another important aspect.

To verify the effect of the distribution of condensed phase reactions on the transient burning of solid propellants, the response of the propellant on a pressurization was calculated. The calculations started from a steady state at $t=0$, followed by an increase in pressure according to

$$p(\tau) = \bar{p} + \Delta p \cdot \left(1 - e^{-\tau}\right) \quad . \tag{3}$$

For these calculations $\bar{p}=\Delta p=1$ MPa. The total heat released by chemical reactions is assumed to be 150 cal/g. This value is somewhat larger than the realistic values (100..125 cal/g), but was choosen because it clearly demonstrates the effect of the different distributions.

Figure 4 contains several typical results. Curve 1 shows the fluctuating surface temperature for a propellant with all the chemical reactions collapsed to the surface ($H_s\neq 0$, $H_c=0$). Curve 2 is obtained from calculations with all chemical reactivity in the condensed phase ($H_s=0$, $H_c\neq 0$). For these calculations a high activation energy has been used (28.9 kcal/mole, according to ref.[5]), i.e. the heat is released in a thin layer close to the surface, and falls to exponentionally small values, even at short distances from the surface. As expected for this

high value of the activation energy the response is similar, showing a damped response. This shape can be attributed to the increase in burning rate during the increase in pressure. At higher burning rates the thermal zone in the condensed phase is smaller. Because the temperature distribution was in its steady state at $t=0$, the layer is too thick during the transition. Thus a preheated zone exists, which burns away fast (the maximum in the response). After this period almost no thermal layer exists, and it takes time to build a new thermal layer by heat conduction from the gasesous phase (minimum in the response). Note that the response of the propellant resembles a typical response of an underdamped second order mass-spring-dasphot system on a step response. This analogy can be shown by approximation of the partial differential equation (1) by an ordinary differential equation [1]. Curve 3 is the result of calculations with an activation energy of 10 kcal/mole. The energy is released in a wider layer, yielding a slower response. The three responses show that even for a narrow chemical zone, the approximation of this zone by a heat release at the surface is not correct (difference between curves 1 and 2). For real propellants the reaction zone is spatially distributed over a wider thermal layer, which exhibits a different response. These calculations illustrate that the transient burning of solid rocket propellants is greatly affected by a spatial distribution of the heat release due to chemical reactions.

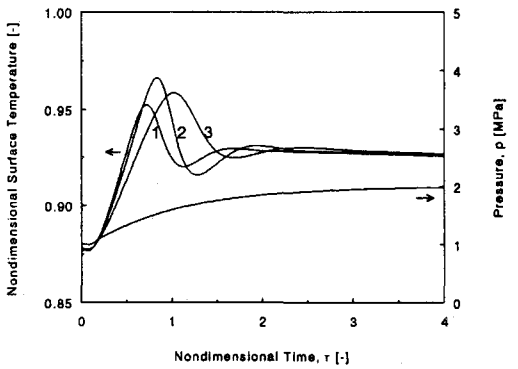

Figure 4 Combustion transient during a pressurization from 1 to 2 MPa.

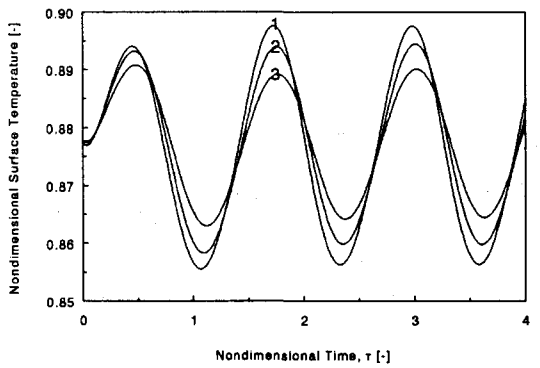

Figure 5 Fluctuating surface temperature during a sinusoidal pressure disturbance.

For the three same cases the surface temperature was monitored for a sinusoidal pressure disturbance of 500 Hz. Figure 5 shows the results of these calculations. When compared to the results of the pressurization experiment it is seen that now curve 1 gives the largest response.

♦ Response Functions

From the transient calculations the response function of the propellant can be calculated. The pressure driven response function is computed by perturbing the steady state with a sinusoidal fluctuating pressure, with an amplitude of 10% of it mean value. After a few cycles a situation of dynamic equilibrium develops. For high frequencies the number of transient cycles is larger because it takes more cycles to burn through the disturbed preheated zone. Figure 6 is an example of such a situation. The relative change in burning rate, r_b, during this equilibrium divided by the relative change in pressure defines the pressure coupled response function, according to:

$$R_p = \frac{r_b'/\overline{r_b}}{p'/\overline{p}} \,. \tag{4}$$

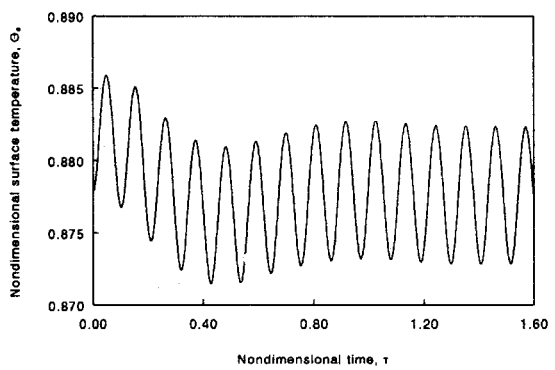

Figure 6 Fluctuating surface temperature due to a sinusoidal pressure disturbance with an amplitude of 10% of its mean value. After a few initial cycles the response of the reaches a dynamic equilibrium.

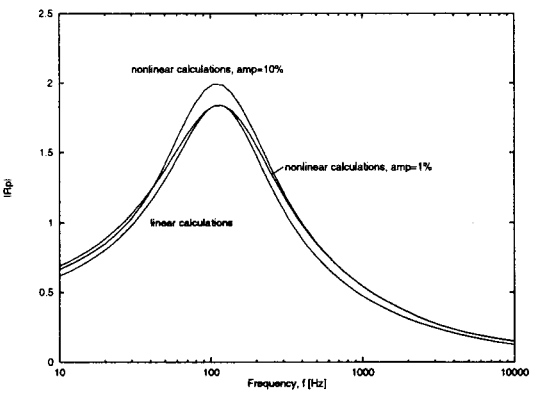

Figure 7 Nonlinear pressure driven response functions versus linear calculated response function.

To verify the numerical calculations under limit conditions, a comparison has been made with the familiar linearized analysis [1]. Figure 7 is an example of such a calculation. For these calculations the condensed phase is assumed to be inert, with no phase transitions, and constant thermal properties. It is seen that the response function for a disturbance amplitude of 10% predicts a much larger response than that for an amplitude of 1%. So even for the usual $\Delta p/\bar{p}$=0.1, nonlinearity plays an important role. This is an important restriction when pressure coupled experiments are compared with linearized analysis. From an experimental point of view, large disturbance amplitudes are desirable for acceptable signal to noise ratios.

The nonlinearity from figure 7 is confirmed by the Fast Fourier Transform (FFT) calculations of the propellant response on a sinusoidal pressure disturbance with a frequency of 500 Hz, (figure 8). This figure demonstrates that a second harmonic is introduced for an amplitude of 10% of the mean signal. For a larger amplitude even more harmonics appear.

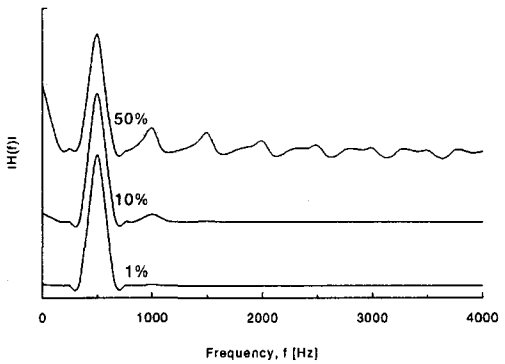

Figure 8 Effect of the disturbance amplitude on the fft-spectrum.

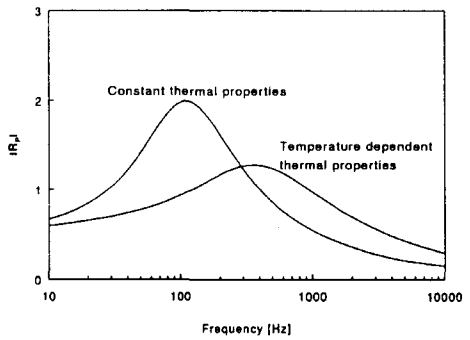

Figure 9 Effect of thermal properties on the pressure coupled response function.

The effect of the temperature dependent properties on the pressure driven response functions is shown in figure 9. As seen from figure 3, the thermal layer thickness of the analytical temperature profile is much larger than that of the other two profiles because of the reduced thermal conductivity of AP. This thermal layer stores information of foregoing disturbances. Because of the smaller affected zone of the condensed phase for a propellant with temperature dependent thermal properties, the response is smaller. This smaller zone has a higher resonance frequency, expressed by the shifting of the maximum of the response function to higher frequencies.

The effect of phase changes of AP are not only found in the thermal properties, but coupled with it are the latent heats of transition, H_{tra} and H_m. As seen from curve 3 of figure 3, this leads to a smaller thermal layer, with an accompanying higher resonance frequency. This is confirmed by the calculations of figure 10. The propellant for which phase transitions are accounted for has a smaller maximum of the response function, indicating that this propellant is more stable, as compared to the propellant for which the latent heats are assumed to be zero.

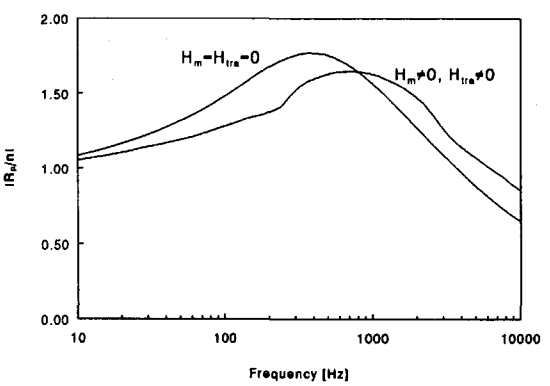

Figure 10 Effect of crystal transitions on the normalized pressure coupled response function.

Figure 11 shows the effect of the heat release distribution on the response function, for the same situations of the figures 4 and 5, however, now the more realistic heat release of 125 cal/g has been used. It is seen that the condensed phase reactions lower the maximum response. So, when subsurface reactions are approximated by surface reactions, the propellants appears to be less stable. The maxima of the response function shift to lower frequencies, because the thermal layer is larger for subsurface reactions.

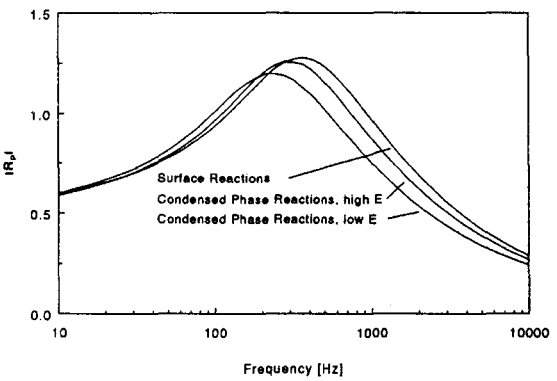

Figure 11 Pressure coupled response function for several chemical heat release distributions.

♦ Conclusions

- The approximation of constant thermal properties is too crude to predict the response of a propellant accurately.

- Phase changes in the condensed phase yields a more stable propellant, lowering the maximum of the response function and shifting it to higher frequencies.

- Solid phase reactions have a similar effect on the transient burning as the surface heat release. Subsurface reactions demonstrate an decrease in maximum and resonance frequency for an increase in chemical reaction zone width.

- For small disturbance amplitudes of 1%, the response of the propellant is linear, for 10% disturbances the nonlinearity cannot be neglected anymore, and differences can be found from small amplitude calculations.

♦ References

[1] L. DeLuca, *Theory of Nonsteady Burning and Combustion Stability by Flame models*, in: Nonsteady Burning and Combustion Stability of Solid Propellants, edited by L. Deluca, E.W. Price, and M. Summerfield, AIAA Progress in Astronautics and Aeronautics Vol. 143, Chapter 14, 1992.

[2] C. Zanotti, and A. Volpi, *Measuring Thermodynamic Properties of Burning Propellants*, in: Nonsteady Burning and Combustion Stability of Solid Propellants, edited by L. Deluca, E.W. Price, and M. Summerfield, AIAA Progress in Astronautics and Aeronautics Vol. 143, Chapter 5, 1992.

[3] C. Guirao, and F.A. Williams, *A Model for Ammonium Perchlorate Deflagration between 20 and 100 atm*, AIAA Journal **9**, 1345 (1971).

[4] C.E. Hermance, *A Model of Composite Propellant Combustion Including Surface Heterogeneity and Heat Generation*, AIAA Journal **4**, 1629 (1966).

[5] R.N. Kumar, and F.E.C. Culick, *Role of Condensed Phase Details in the Oscillatory Combustion of Composite Propellants*, AIAA Paper No. 73-218 (1973).